Pneumatic Particulate Collection System Analysis and Design

Michael W. Bromley II

Thesis submitted to the Faculty of the
Virginia Polytechnic Institute and State University
in partial fulfillment of the requirements for the degree of

Master of Science
in
Mechanical Engineering

Kevin B. Kochersberger, Co-Chair
Francine Battaglia, Co-Chair
Alan A. Kornhauser

June 4, 2012
Blacksburg, Virginia

Keywords: Particulate Sampling, Particle Entrainment, Pneumatic transport, FLUENT
Multiphase Flow, CFD

Pneumatic Particulate Collection System Analysis and Design

Michael W. Bromley II

ABSTRACT

A pneumatic particulate collection system harnesses the energy associated with the release of a compressed gas to transport particulate to a collection chamber. In an effort to improve the efficiency of a previously designed collection system, high speed imaging in conjunction with computational fluid dynamics (CFD) was utilized to highlight design deficiencies. Areas of recirculation within the collection device as well as impingement of the sampling surface were observed through the testing and CFD analysis. The basis of the improved collection system was conceived through research of pneumatic transport and the deficiencies found through testing and simulation. An improved rectangular-duct-styled system was designed in three main stages. A variety of filters used to contain the desired particulate were characterized through testing for use in simulations as well as fluids calculations. The improved system was then analyzed utilizing compressible and incompressible flow calculations and design iterations were conducted with CFD to determine the final parameters. The final design was simulated with a multiphase flow model to examine the particulate entrainment performance. The improved collection system efficiently expanded and developed the gas flow prior to the collection area to employ the particulate entrainment process. The final design was constructed with an additive manufacturing process and experimentally tested to validate the simulations and flow calculations. The testing proved that the final design operated purely on particulate entrainment and collected only the top layer of particles as simulated. The improved collection system eliminated all areas of flow recirculation and impingement of the particle bed to provide a more efficient sampling device.

Contents

List of Figures

List of Tables

Nomenclature

Variables

A	Area
Ar	Archimedes number
C_D	Drag coefficient
c_p	Constant pressure specific heat
c	Speed of sound
d_p	Particle diameter
D	Duct or pipe diameter
e_{ss}	Coefficient of restitution
E	Total energy
f	Friction factor
g	Gravity
$g_{0,ss}$	Radial distribution function
h	Enthalpy
J	Mass flux
k	Turbulent kinetic energy, specific heat ratio
K_{gs}	Interphase momentum exchange coefficient
K_L	Loss coefficient
K_{ss}	Interphase momentum exchange coefficient

L, l	Length
Ma	Mach number
p, P	Pressure
R	Gas constant
Re_p	Particle Reynolds number
Re_p^*	Modified particle Reynolds number
Re	Reynolds number
T	Temperature
t	Time
u	Velocity component
U_{gpu}	Gas pickup velocity
u'	Fluctuating velocity component
U, V	Average velocity
$\vec{v}$	Velocity vector
x	Position vector

Greek

α	Phasic volume fraction
ϵ	Turbulence dissipation rate
γ	Specific weight
λ	Bulk viscosity
μ	Dynamic viscosity
μ_{sh}	Shear viscosity
μ_t	Turbulent viscosity
ω	Angular velocity
$\overline{\overline{\tau}}$	Stress-strain tensor

ϕ	Angle of internal friction
ρ	Density
σ_ϵ	Turbulent dissipation rate Prandtl number
σ_k	Turbulent kinetic energy Prandtl number
Θ	Granular Temperature

Subscripts

g	Gas
p	Particle
q	Phase
s	Solid

Superscripts

*	Choked flow location

Chapter 1.

Introduction

1.1 Background

The operation of particulate collection has been performed for years by a wide variety of devices and for many applications such as gold mining to lunar sampling. The Unmanned Systems Laboratory (USL) at Virginia Tech was tasked with designing a collection system to be deployed on an unmanned aerial vehicle (UAV) to collect a sample of material from a remote site for further analysis. The material of interest is the top layer of small to fine particulate on the order of 500 μm (the size of table salt). Mike Couch [8] from the USL tested the feasibility of using a vacuum sample collection system; however he found the power draw and shear size to be too great to be implemented on a UAV. Therefore, he proposed the concept of a pneumatic particulate collection system (PCS) in which compressed air provides the energy for transporting and collecting the desired material. It is the purpose of this thesis to present the testing and analysis of the previous design and present a new and improved design based on the findings.

The previously designed PCS was to be deployed on a ground robot tethered to a helicopter UAV. The system utilized the kinetic energy associated with the release of the

compressed air to transport particles to a collection area. The PCS consisted of an on board pressurized air supply, an array of solenoid valves and the sampling device as shown in Figure 1.1. The air supply was an aluminum compressed air tank. The tank contained 0.002 m^3 of air pressurized to 827 kPa and was 0.254 m in length and 0.109 m in diameter. This design allowed for 2.8 seconds of flow time through the five nozzles. The sampling device is divided into two main areas, the sampling chamber and the collection chamber as pictured in Figure 1.2. The sampling chamber is an array of five flow channels, shown in Figure 1.3, to eliminate effects between each nozzle's flow patterns. Pressurized air is released through the five nozzles into the sampling chamber where the particulate collection process begins. The nozzles are positioned parallel to the sampling surface in an attempt to employ the process of particle entrainment. The high speed air ideally entrains the particles into the air flow stream and carries them up the ramp and into the collection chamber. The air exits the system via four exhaust ports covered with a paper filter retaining all particles larger than

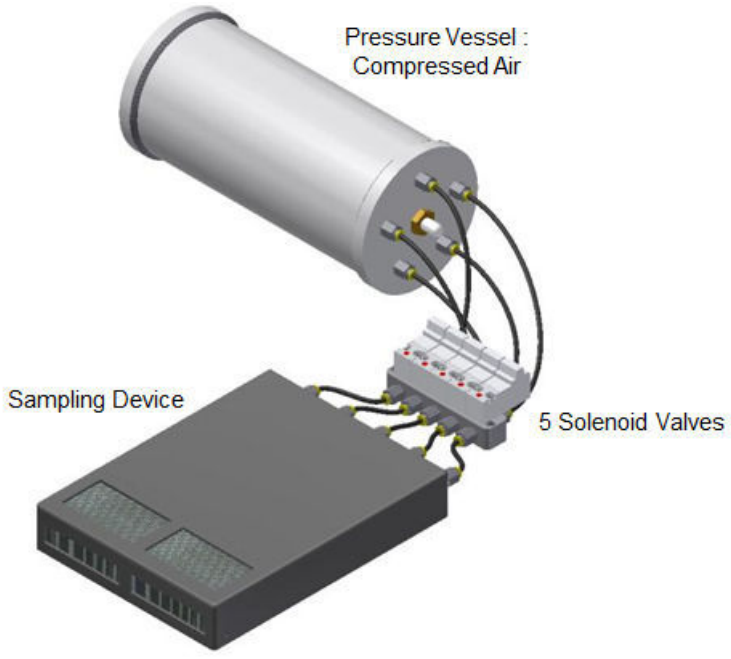

Figure 1.1: The original USL particulate collection system consisting of a pressure vessel, an array of solenoid valves, and the sampling device.

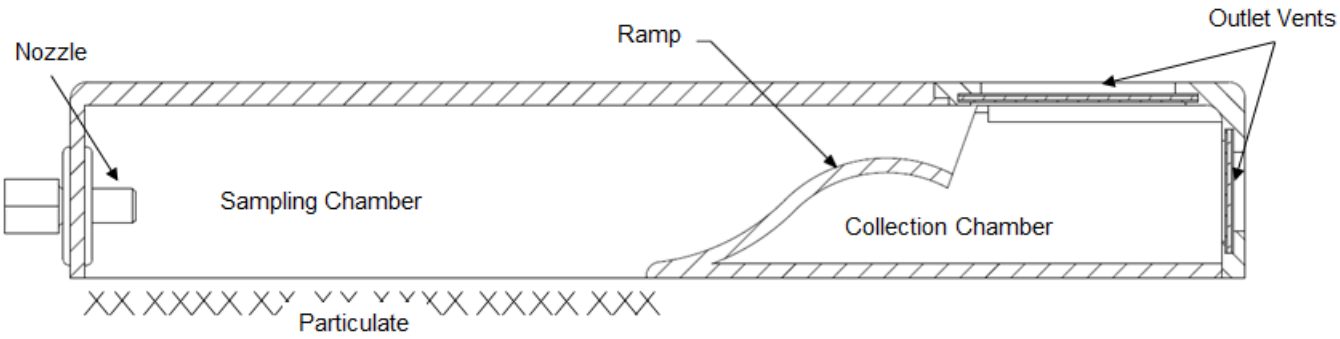

Figure 1.2: Sampling device divided into two key areas: sampling chamber and the collection chamber.

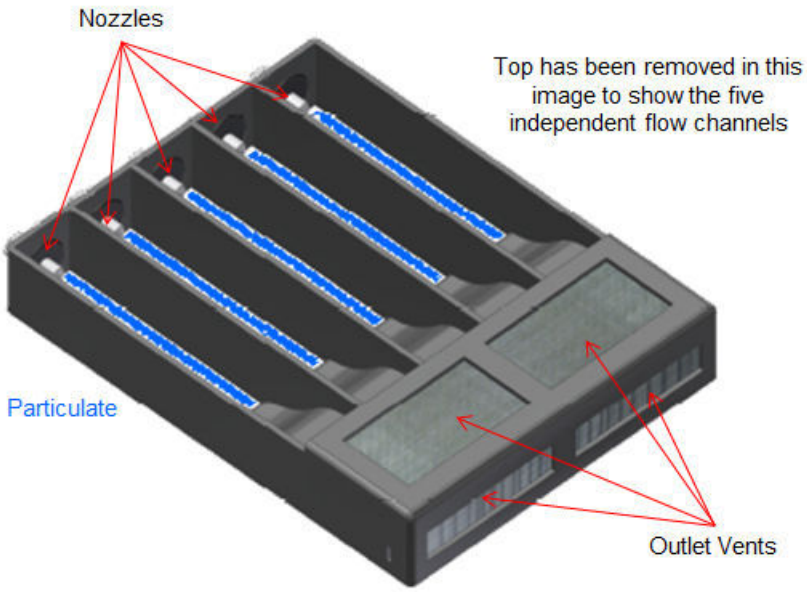

Figure 1.3: The sampling device with the top removed to show the five separate flow channels in the sampling chamber.

5 µm. The system shown in Figure 1.1 provided the basis of a new design for an improved collection system.

1.2 Objectives

An adjustable collection system modeled after the original PCS was created purely for testing purposes to investigate the effects of design changes as well as to collect data for computational fluid dynamics (CFD) analyses. The experimental testing and analyses of the original PCS divulged design flaws and areas for improvement. The high speed imaging as well as the CFD simulations showed areas of recirculation, wasting valuable energy for particle transport. It was also noticed that despite the nozzles being positioned parallel to the particle bed, the jet was impinging the particle surface instead of operating purely by entrainment, as was desired. These results in conjunction with research in the area of particle entrainment and transport influenced the creation of the new design.

Unlike the previous collection system, the new design was no longer constrained by being mounted on a ground robot. However, it was still desired to be carried on board a UAV and operated as a standalone system. Therefore a few constraints were imposed on the system. First and foremost, weight is always of concern when designing for aerial vehicles. The carrying capacity is limited depending on the size of the aircraft and the minimum amount of additional weight possible is always desired. The second constraint is the size of the system which is limited by the capabilities of the rapid prototyping machine, Stratasys Dimensions SST 768, to a volume of 0.254 m x 0.254 m x 0.305 m. These dimensions also insured that the system would fit within the payload bay of the UAVs operated by the USL. It was chosen to build the collection system with an additive manufacturing process to provide a system that is easily manufactured and quickly reproducible. The additive manufacturing

process also provides the ability to create complex shapes that typical machining processes can not achieve.

An improved rectangular duct design was proposed as the basis of the new collection device. The aim was to produce a device that would operate purely on particulate entrainment and eliminate areas of recirculation. The collector design was analyzed through fluids calculations and CFD to create a system that achieved a fully developed velocity profile at the collection area of the proper magnitude to entrain the particulate. The final design was manufactured and bench tested to validate the fluids calculations and CFD results as well as to test the final performance.

1.3 Outline of Thesis

Chapter 2 begins with a literature review of particle transport theory and important relationships to characterize transport. Included is a discussion of numerical modeling of multiphase flow and compressible flow. The previously designed PCS is tested and analyzed in Chapter 3 through high speed imaging and CFD. The simulations begin in a 2D environment to investigate the effects of model and parameter changes and then are transferred to a 3D environment. In Chapter 4, an improved collection system is analyzed with fluids calculations and design iterations are conducted utilzing CFD to determine the final design parameters. The final collector design is simulated with a multiphase model to test the particulate entrainment performance. Lastly, the final design is manufactured and bench tested for comparison with the fluids calculations and CFD models. Chapter 5 includes conclusions drawn and recommendations for future improvements of the particulate collection system.

Chapter 2.

Literature Review

A pneumatic system for the purpose of particulate collection is a unique subject in both CFD simulations as well as experimental measurements. As a result, little published work exists on the subject. However, the process of particulate entrainment and transport has been studied in areas such as river bed and sand erosion as well as pneumatic transport. The theories and concepts developed in the aforementioned fields will greatly influence the basic design features of the collection system. The simulation of a gas-solid flow in CFD has been studied extensively for fluidized beds in the chemical, metallurgical, environmental, and energy industries for purposes such as fossil fuel combustion, coal, and biomass gassification. CFD has also been applied to other topics such as sediment transport and drifting particles in nature. The applications of CFD in multiphase flows was researched as a basis for model selection in the analyses to be performed on the PCS.

2.1 Particulate Transport

Pneumatic particle transport has been employed for over a century and considerable work has been conducted in this field. A key parameter to the pneumatic transport of particles

is the minimum conveying velocity, defined as the minimum gas velocity for horizontal conveyance of solid particles [7, 12]. Operating a pneumatic conveying system with too high of a velocity results in an unnecessary increase in the pressure drop and as a result energy costs. Alternatively, too low of a conveying velocity could result in a blockage or deposition of the particles on the bottom of the pipe. It is desired to predict the minimum conveying velocity based upon key parameters such as the particle diameter, particle density, the gas density, and the size of the system. Many researchers have studied in this field and several terms have been used in place of the minimum conveying velocity including: pickup velocity, suspension velocity, critical velocity, rolling or sliding velocity, etc. Despite the variety of terms used, the main goal of all of the studies is to be able to predict the minimum conveying velocity required for pneumatic transport.

2.1.1 Particle Pickup Velocity

Cabrejos and Klinzing [7] studied the pickup and saltation mechanisms of solid particles experienced in horizontal pneumatic transport. The pick up velocity is defined as the gas velocity required to resuspend a particle initially at rest on the bottom of a pipe. On the contrary, saltation velocity is defined as the gas velocity at which the particles start to drop out of suspension and settle on the bottom of the pipe. Different experimental setups were used in the study of the pick up and saltation velocities. To determine the pick up velocity, a one meter long layer of particles with approximately half of the cross-sectional area of the pipe left free was created. The pipe used was transparent to allow for observation of the particle movement. The gas flow rate through the pipe was set constant and the layer would erode away therefore increasing the free area. The increase of the free area resulted in a decrease of velocity across the particles and naturally it would reach an equilibrium state. The volumetric flow rate and the area above the particulate at the equilibrium state

was recorded. The tests were performed for a wide range of particle sizes and a dimensional analysis was performed. A simple correlation is presented as,

$$\frac{U_{gpu}}{\sqrt{gd_p}} = 0.0428 Re_p^{0.175} \left(\frac{D}{d_p}\right)^{0.25} \left(\frac{\rho_p}{\rho_g}\right)^{0.75} \tag{2.1}$$

where U_{gpu} is the minimum pick up velocity, d_p is the particle diameter, D is the pipe diameter, ρ_p is the particle density, ρ_g is the gas density, and Re_p is the particle Reynolds number. Cabrejos and Klinzing define the particle Reynolds number as,

$$Re_p = \frac{d_p U_g \rho_g}{\mu_g} \tag{2.2}$$

where U_g is the gas velocity and μ_g is the gas dynamic viscosity. The correlations were able to accurately predict the pickup velocity of particles ranging from 100 μm to 1000 μm. However, the experiments were based purely on visual observation to determine the state of the particles.

Kalman et al. [13] furthered the studies of Cabrejos and Klinsing [7] and created a method for measuring the pickup velocity of particles other than by visual observation. Experiments were conducted in a rectangular wind tunnel in which a section downstream incorporated a rectangular bath at the bottom surface that was filled with particles. The top layer of the particles matched the bottom surface of the wind tunnel. The pickup velocity was then determined quantitatively by measuring the reduction of weight of the particles and plotting it against the air velocity. A curve was fitted to the data and the minimum pickup velocity was determined as the intersection of the fit curve and the point at which zero weight loss occurred. The experiment was repeated and the minimum pick up velocities for a variety of particle sizes were found. Kalman et al. [13] desired to find a set of non-dimensional numbers to describe the pick up velocities as well. Cabrejos and Klinzing [7]

had found that the Reynolds number and the Froude number accurately described the pick up velocity; Kalman et al. [13] proposed that the Reynolds and Archimedes number as a better indication where:

$$\text{Re} = \frac{\text{inertial force}}{\text{viscous force}}$$

$$\text{Ar} = \frac{\text{inertial force} \cdot \text{bouyancy force}}{(\text{viscous force})^2}$$

A simple function can then be used to describe the pickup velocity of particles larger than 100 μm where,

$$Re_p = 2.66 Ar^{0.474} \tag{2.3}$$

and Re_p is as defined in Equation 2.2 and the Archimedes number is defined as:

$$Ar = \frac{g\rho_g \left(\rho_p - \rho_g\right) d_p^3}{\mu_g^2} \tag{2.4}$$

Unlike the equations presented by Cabrejos and Klinzing [7], the proposed equations do not account for the pipe diameter or duct size.

2.1.2 Pipe Diameter Correction

Many experimentalists have conducted tests on the entrainment and transport of particles. As a result, there is a large amount of data available, however the tests were conducted in a variety of experimental test setups.

In order to compare the data from each experiment a relationship was needed to convert the pick up velocity measured in the test diameter to a common diameter. Kalman et al.

[13] proposed a non-dimensionalized conversion defined as,

$$Re_p^* = \frac{\rho_g U_{gpu} d_p}{\mu_g \left(1.4 - 0.8 \cdot e^{-\frac{D/D_{50}}{1.5}}\right)} \tag{2.5}$$

where D is the pipe diameter or equivalent hydraulic diameter, and lastly D_{50} is the diameter of a 50 mm pipe. The modified Reynolds number, Re_p^*, is used to compile the data from a wide range of experiments into a comparable set of pick up velocities.

2.1.3 Three Zone Model

Kalman et al. [13] proposed a method to describe the experimental data from Cabrejos and Klinzing [7], Hayden et al. [12], and Kalman et al. [13] using a simple three zone model. The three zone model describes the pick up velocities required for a wide range of particle diameters. The first zone consists of large particle sizes in which the weight of the particle is the main constraint on particle pick up. In this zone the modified Reynolds number is as:

$$Re_p^* = 5Ar^{3/7} \text{ for } Ar > 16.5 \tag{2.6}$$

The second zone consists of smaller particles in which the cohesive forces begin to contribute the resistance to entrainment. The modified Reynolds number remains constant for the second zone where:

$$Re_p^* = 16.7 \text{ for } 0.45 < Ar < 16.5 \tag{2.7}$$

Finally, zone three represents even smaller particles where the cohesive forces dominate.

In this zone the modified Reynolds number is defined as:

$$Re_p^* = 21.8Ar^{1/3} \text{ for } Ar < 0.45 \tag{2.8}$$

A compilation of the experimental data is plotted against the three zone model in Figure 2.1. As can be seen from Figure 2.1 the three zone model accurately describes the minimum or critical pickup velocity of a wide range of particle sizes. The solid line in Figure 2.1 represents the critical or minimum pick up velocity; therefore any point that lies above the line will result in transport of the particle.

The three zone model was also applied to studies conducted by Ramadan et al. [19] who tested the pickup velocity of sand in water. Although the pick up velocity was determined visually, the three zone model was in agreement with the velocities observed. This confirms that the zone equations can accurately include the effects of the fluid density on the pick up velocity. The three zone model in conjunction with Equation 2.5 to account for the

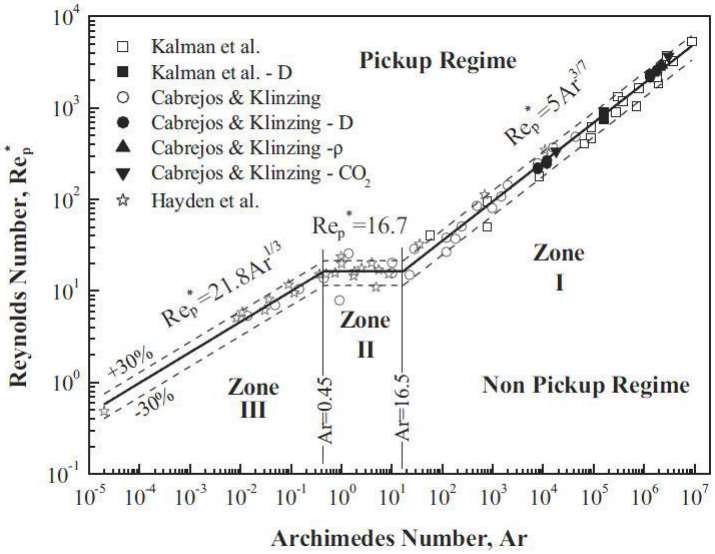

Figure 2.1: The three zone model plotted with experimental data from multiple researchers. [13]

pipe diameter size will be utilized in determining the desired minimum velocity for particle transport in the collector design of the work herein.

2.2 Multiphase Flow Modeling and Applications

Computational fluid dynamics (CFD) has been used in a wide range of fields to predict and analyze multiphase flows. The use of CFD allows for designs to be tested without any manufacturing, therefore the available software packages are becoming increasingly more accurate in flow predictions to save time and money. The commercial code used in this thesis for all simulations is ANSYS FLUENT v13.0. In an effort to select the appropriate models, research was done on previous applications of multiphase flow and the modeling techniques used.

Gas-solid flows have been studied in wide variety of fields and validated against experimental results for accuracy. There are two prominent methods for modeling a multiphase flow: Eulerian-Lagrangian and Eulerian-Eulerian. The former of the two methods is computationally intensive as it treats the fluid phase as a continuum by solving the Navier-Stokes equations and the dispersed phase is solved by tracking a large number of particles throughout the flow field. The application of the Eulerian-Lagrangian method assumes that the dispersed secondary phase occupies a low volume fraction of the flow. The Eulerian-Eulerian method treats each phase as an interpenetrating continua, thus two phases cannot occupy the same volume of space at any point in time. Phasic volume fractions are introduced and the sum of the volume fractions at any point in space and time must be equal to one.

It was found that the Eulerian-Eulerian approach is generally accepted for gas-solid flow. A study of gas-solid jets in a circulating fluidized bed riser flow was performed by Li and Guenther [15]. This work was significant in that the penetrating jet flow was modeled as two-

phase and with a high gas velocity of up to 37.18 m/s which further increased the complexity of the simulation. However, employing an Eulerian-Eulerian approach, Li and Guenther showed that the hydrodynamics of the overall flow and the characteristics of the gas-solid jet were predicted reasonably well when compared to experimental data. Another study of fluidized beds was conducted by Battaglia et al. [3] in an effort to accurately predict the hydrodynamic behavior measured experimentally. Once again an Eulerian-Eulerian model was implemented and found to accurately predict the pressure drop as well as the fluidization velocity with adjustments only to the initial solid bed height. The study was performed initially with sand as the bed medium, but was also conducted using ground walnut shell and ground corncob. All of the simulations correctly predicted the pressure drop curves measured experimentally.

A study of drifting windblown particles was performed by Alhajraf [1] utilizing both two- and three-dimensional Eulerian-Eulerian simulations. It was the goal of the study to accurately predict a natural phenomenon known as the Aeolian process. This process is divided into three stages: erosion, transportation, and deposition, which occurs when wind or an aerodynamic force entrains particles from rest and carries them some distance. First the model was used to simulate drifting snow and then was applied to sand drifting around a double row porous fence. The simulations showed good qualitative as well as quantitative agreement with field and wind tunnel observations for both cases. A similar study was performed by Pattanapol et al. [17] to determine suitable foredune morphologies to prevent erosion damage. Light detection and ranging (LIDAR) data was used to recreate the topography of the area and historical wind data was used for the boundary conditions. The Volume of Fluid Eulerian-Eulerian method provided by FLUENT was utilized. The CFD modeling proved to be an effective tool and was able to accurately predict the sand erosion.

The applications discussed are only a small portion of the studies available where a Eulerian-Eulerian approach is implemented in a gas-solid flow. Due to the size of the particles desired to be collected, the volume fractions expected and the relative accuracy of a Eulerian-Eulerian model, it was chosen to be employed for the simulations to follow.

2.3 FLUENT Theory

Computational fluid dynamic simulations were used extensively in this work to analyze experimental testing as well as to predict performance of proposed designs. The CFD code utilized for all simulations was ANSYS FLUENT v13.0 [2]. A finite volume approach is used by FLUENT in simulating a variety of flow situations. Two main categories of simulations completed in this work are: multiphase flow with turbulence and compressible flow with turbulence. The governing equations for each scenario will be presented in the following sections.

2.3.1 Multiphase Turbulent Flow: Governing Equations

The Eulerian-Eulerian model provided by FLUENT was selected for all multiphase flows as discussed in 2.2. This model selection solves momentum and continuity equations for each phase. It also requires that a single pressure is shared by all phases and that the volume fraction at any discrete volume and point in time must sum to one. In every multiphase case simulated in this thesis the number of phases is equal to two; the primary phase represents the gas and the secondary phase is a granular phase representing the particles. The continuity equation for each phase, q, is defined as,

$$\frac{\partial}{\partial t}\left(\alpha_q \rho_q\right) + \nabla \cdot \left(\alpha_q \rho_q \vec{v_q}\right) = 0 \tag{2.9}$$

where $\vec{v}$ is the velocity and α is the phasic volume fraction. The conservation of momentum for the gas phase yields,

$$\frac{\partial}{\partial t}\left(\alpha_g \rho_g \vec{v}_g\right) + \nabla \cdot \left(\alpha_g \rho_g \vec{v}_g \vec{v}_g\right) = -\alpha_g \nabla p + \nabla \cdot \bar{\bar{\tau}}_g + \alpha_g \rho_g \vec{g} + \sum_{p=1}^{2} \vec{R}_{gs} \tag{2.10}$$

where $\bar{\bar{\tau}}_g$ is the phase stress-strain tensor defined as,

$$\bar{\bar{\tau}} = \alpha_q \mu_{sh,q} \left(\nabla \vec{v}_q + \nabla \vec{v}_q^T\right) + \alpha_q \left(\lambda_q - \frac{2}{3}\mu_{sh,q}\right) \nabla \cdot \vec{v}_q \bar{\bar{I}} \tag{2.11}$$

where the phase q is replaced by g for the gas phase. In Equations 2.10 and 2.11, $\mu_{sh,q}$ is the shear viscosity, λ_q is the bulk viscosity, and $\vec{R}_{gs}$ is an interaction force between the phases. The interaction force between the phases is defined as,

$$\sum_{p=1}^{2} \vec{R}_{gs} = \sum_{p=1}^{2} K_{gs} \left(\vec{v}_g - \vec{v}_s\right) \tag{2.12}$$

where K_{gs} is the interphase momentum exchange coefficient.

The conservation of momentum for the s^{th} solid phase is,

$$\frac{\partial}{\partial t}\left(\alpha_s \rho_s \vec{v}_s\right) + \nabla \cdot \left(\alpha_s \rho_s \vec{v}_s \vec{v}_s\right) = \alpha_s \nabla p - \nabla p_s + \bar{\bar{\tau}}_s + \alpha_s \rho_s \vec{g} + \sum_{l=1}^{N} K_{gs} \tag{2.13}$$

where $\bar{\bar{\tau}}_s$ is the stress-strain tensor for the solid phase defined by Equation 2.11, p_s is the solids pressure, and K_{gs} is the momentum exchange coefficient between gas phase g and solid phase s. The gas-solid momentum exchange coefficient is defined as,

$$K_{gs} = \frac{3}{4} C_D \frac{\alpha_s \alpha_g \rho_g \mid \vec{v}_s - \vec{v}_g \mid}{d_s} \alpha_g^{-2.65} \tag{2.14}$$

when $\alpha_g > 0.8$ and as,

$$K_{gs} = 150\frac{\alpha_s\left(1-\alpha_g\right)\mu_g}{\alpha_g d_s^2} + 1.75\frac{\rho_g \alpha_s \mid \vec{v}_s - \vec{v}_g \mid}{d_s} \tag{2.15}$$

when $\alpha_g \leq 0.8$. The drag coefficient that appears in Equation 2.14 is calculated as,

$$C_D = \frac{24}{\alpha_g Re_s}\left[1 + 0.15\left(\alpha_g Re_s\right)^{0.687}\right] \tag{2.16}$$

when utilizing the Gidaspow model. The particle Reynolds number appearing in Equation 2.16 is defined as shown in Equation 2.17.

$$Re_s = \frac{\rho_g d_s \mid \vec{v}_s - \vec{v}_g \mid}{\mu_g} \tag{2.17}$$

When the granular (secondary) phase volume fraction is less than the maximum allowed value, termed the packing limit, a solids pressure is calculated independently and used in Equation 2.13 as ∇p_s. The solids pressure is comprised of two terms; a kinetic term and a term due to particle collisions,

$$p_s = \alpha_s \rho_s \Theta_s + 2\rho_s\left(1+e_{ss}\right)\alpha_s^2 g_{0,ss}\Theta_s \tag{2.18}$$

where Θ_s is a granular temperature, e_{ss} is a coefficient of restitution, and $g_{0,ss}$ is a radial distribution function. The radial distribution function describes the spacing between the solid particles when the volume fraction is less than the maximum. Therefore it is a correction factor that modifies the probability of collisions within the granular phase. The granular temperature is a parameter associated with the random fluctuation of the solid particles. The velocity fluctuations of the solid particles dissipate into heat as a result of the inter-particle collisions and is termed the granular temperature.

The solids stress tensor includes shear and bulk viscosities which arise from particle momentum exchange during collisions and movement. The shear viscosity is comprised of three components that describe collisions, kinetic energy, and friction. The overall shear viscosity is defined as,

$$\mu_{sh} = \mu_{sh,col} + \mu_{sh,kin} + \mu_{sh,fr} \tag{2.19}$$

The collisional part of the shear viscosity is,

$$\mu_{sh,col} = \frac{4}{5}\alpha_s \rho_s d_s g_{0,ss} \left(1 + e_{ss}\right) \left(\frac{\Theta_s}{\pi}\right)^{1/2} \alpha_s \tag{2.20}$$

The kinetic part is defined by the expression,

$$\mu_{sh,kin} = \frac{10\rho_s \sqrt{\Theta_s \pi}}{96\alpha_s \left(1 + e_{ss}\right) g_{0,ss}} \left[1 + \frac{4}{5} g_{0,ss} \alpha_s \left(1 + e_{ss}\right)\right]^2 \alpha_s \tag{2.21}$$

as provided by Gidaspow et al. [9] Initially, the particle bed is very close the the packing limit and the generation of stress is mainly due to the friction between the particles. As a result, the frictional viscosity model is enabled which calculates,

$$\mu_{sh,fr} = \frac{p_s \sin\phi}{2\sqrt{I_{2D}}} \tag{2.22}$$

where p_s is the solids pressure, ϕ is the angle of internal friction, and I_{2D} is the invariant of the deviatoric stress tensor. The bulk viscosity term appearing in the stress-strain tensor Equation 2.11 for the solid phase accounts for the resistance of granular particles to compression and expansion. The Lun et al. [6] model is chosen and defines the bulk viscosity as,

$$\lambda_s = \frac{4}{3}\alpha_s \rho_s d_s g_{0,ss} \left(1 + e_{ss}\right) \left(\frac{\Theta_s}{\pi}\right)^{1/2} \tag{2.23}$$

The $k-\varepsilon$ dispersed turbulence model was chosen as it is appropriate when the dominant process in the random motion of the secondary phase is due to the influence of the primary phase turbulence. In the cases studied, the turbulence of the high velocity jet is the primary reason for turbulence in the particle bed. The dispersed turbulence model predicts the turbulence of the primary continuous phase using a supplemented standard $k-\varepsilon$ model as,

$$\frac{\partial}{\partial t}\left(\alpha_q \rho_q k_q\right) + \nabla \cdot \left(\alpha_q \rho_q \vec{U}_q k_q\right) = \nabla \cdot \left(\alpha_q \frac{\mu_{t,q}}{\sigma_k} \nabla k_q\right) + \alpha_q G_{k,q} - \alpha_q \rho_q \Pi_{k_q} \tag{2.24}$$

$$\frac{\partial}{\partial t}\left(\alpha_q \rho_q \varepsilon_q\right) + \nabla \cdot \left(\alpha_q \rho_q \vec{U}_q \varepsilon_q\right) = \nabla \cdot \left(\alpha_q \frac{\mu_{t,q}}{\sigma_\varepsilon} \nabla \varepsilon_q\right) + \alpha_q \frac{\varepsilon_q}{k_q}\left(C_{1\varepsilon} G_{k,q} - C_{2\varepsilon} \rho_q \varepsilon_q\right) + \alpha_q \rho_q \Pi_{\varepsilon_q} \tag{2.25}$$

where Π_{k_q} and Π_{ε_q} represent the influence of the dispersed phase on the continuous phase, $G_{k,q}$ is the production of turbulent kinetic energy, μ_t is the turbulent viscosity, and $C_{1\varepsilon}$, $C_{2\varepsilon}$ are constants set as 1.44 and 1.92 respectively. The prediction of the turbulence quantities for the secondary phase are obtained through Tchen-theory correlations [2].

2.3.2 Compressible Flow with Turbulence: Governing Equations

FLUENT was used to analyze a single phase compressible flow through a duct. In all cases simulated, the fluid flow was fully turbulent and the realizable $k-\epsilon$ model was employed. In a turbulent flow a Reynolds averaging approach is used to modify the standard instantaneous continuity and momentum equations. The ensemble-averaged continuity and momentum equations are,

$$\frac{\partial p}{\partial t} + \frac{\partial}{\partial x_i}(\rho u_i) = 0 \tag{2.26}$$

$$\frac{\partial}{\partial t}(\rho u_i) + \frac{\partial}{\partial x_j}(\rho u_i u_j) = -\frac{\partial p}{\partial x_i} + \frac{\partial}{\partial x_j}\left[\mu\left(\frac{\partial u_i}{\partial x_j} + \frac{\partial u_j}{\partial x_i} - \frac{2}{3}\delta_{ij}\frac{\partial u_l}{\partial x_l}\right)\right] + \frac{\partial}{\partial x_j}(-\rho\overline{u_i' u_j'}) \tag{2.27}$$

which are referred to as the Reynolds-averaged Navier-Stokes (RANS) equations. The variables are defined as: p is the pressure, u is the velocity components, ρ is the fluid density, x represents the position vector, u' is the fluctuating quantities of velocity, and t is time. Equations 2.26 and 2.27 are applicable to incompressible as well as compressible flow. However, when modeling compressible flow, the conservation of energy equation,

$$\frac{\partial}{\partial t}(\rho E) + \nabla \cdot (\vec{v}\,(\rho E + p)) = -\nabla \cdot \left(\sum_j h_j J_j \right) \tag{2.28}$$

must also be included where E is the total energy, $\vec{v}$ is the velocity vector, h is the enthalpy, and J is the mass flux. The realizable $k-\epsilon$ model was chosen due to increased performance over the standard $k-\epsilon$ model which is especially true in the prediction of the spreading rate for axisymmetric jets. It has been shown that the standard $k-\epsilon$ model predicts the spreading rate of planar jets reasonably well, but shows poor performance for axisymmetric jets [2]. The kinetic energy and dissipation rate equations for the realizable $k-\epsilon$ model are,

$$\frac{\partial}{\partial t}(\rho k) + \frac{\partial}{\partial x_j}(\rho k u_j) = \frac{\partial}{\partial x_j}\left[\left(\mu + \frac{\mu_t}{\sigma_k} \right) \frac{\partial k}{\partial x_j} \right] + G_k + G_b - \rho\varepsilon - Y_M + S_k \tag{2.29}$$

and

$$\frac{\partial}{\partial t}(\rho\varepsilon) + \frac{\partial}{\partial x_j}(\rho\varepsilon u_j) = \frac{\partial}{\partial x_j}\left[\left(\mu + \frac{\mu_t}{\sigma_\varepsilon} \right) \frac{\partial \varepsilon}{\partial x_j} \right] + \rho C_1 S\varepsilon - \rho C_2 \frac{\varepsilon^2}{k + \sqrt{v\varepsilon}} + C_{1\varepsilon}\frac{\varepsilon}{k} C_{3\varepsilon} G_b + S_\varepsilon \tag{2.30}$$

where

$$C_1 = max\left[0.43, \frac{\eta}{\eta + 5} \right], \ \eta = S\frac{k}{\varepsilon}, \ S = \sqrt{2 S_{ij} S_{ij}} \tag{2.31}$$

In Equations 2.29 and 2.30, G_k represents the generation of turbulence kinetic energy due to the mean velocity gradients, G_b represents the generation of turbulence kinetic energy due to buoyancy effects, Y_M is the contribution of compressibility effects to the overall dissipation

rate, C_2 is a constant, σ_k *and* σ_ε are the turbulent Prandtl numbers for k and ε, and S_k and S_ε are user-defined source terms. The turbulent viscosity is calculated the same across all $k-\varepsilon$ models as,

$$\mu_t = \rho C_\mu \frac{k^2}{\varepsilon} \tag{2.32}$$

where C_μ represents a constant. However, in the realizable $k-\varepsilon$ model it is not a constant and is computed from,

$$C_\mu = \frac{1}{A_0 + A_s \frac{kU^*}{\varepsilon}} \tag{2.33}$$

where

$$U^* = \sqrt{S_{ij}S_{ij} + \tilde{\Omega}_{ij}\tilde{\Omega}_{ij}} \tag{2.34}$$

and

$$\tilde{\Omega}_{ij} = \overline{\Omega_{ij}} - \varepsilon_{ijk}\omega_k \tag{2.35}$$

where $\overline{\Omega_{ij}}$ is the mean rate of rotation tensor in a moving reference frame with angular velocity ω_k. The constants seen in Equation 2.33 are defined as,

$$A_0 = 4.04,\ A_s = \sqrt{6}\cos\beta$$

where

$$\beta = \frac{1}{3}\cos^{-1}\left(\sqrt{6}W\right),\ W = \frac{S_{ij}S_{jk}S_{ki}}{\tilde{S}^3},\ \tilde{S} = \sqrt{S_{ij}S_{ij}},\ S_{ij} = \frac{1}{2}\left(\frac{\partial u_j}{\partial x_i} + \frac{\partial u_i}{\partial x_j}\right)$$

The other model constants presented in Equation 2.30 are,

$$C_{1\varepsilon} = 1.44,\ C_2 = 1.9,\ \sigma_k = 1.0,\ \sigma_\varepsilon = 1.2$$

which have been determined experimentally and are valid for a wide range of cases.

Chapter 3.

Previous Design Review

The previous PCS designed by the USL was based on theory and iterated through experimental testing. In an effort to further improve the efficiency of the design, the concept was tested with high speed imaging and analyzed with ANSYS FLUENT. The results from the experimental testing and simulations influenced the new design for improved efficiency.

3.1 Experimental Testing

The experimental testing was conducted to analyze the performance of the previous PCS design as well as gather data to validate ANSYS FLUENT simulations. An adjustable system consisting of a single nozzle was constructed for testing and is pictured in Figure 3.1. The rear wall that contains the nozzle may be adjusted to reduce or increase the distance to the ramp. The height of the system was adjusted by removing one side of the collection system and moving the top plate into a separate set of notches as seen in Figure 3.1. The adjustability allowed for many different designs to be tested with a single system. The setting shown in Figure 3.1 represents the dimensions of the original PCS designed by Mike Couch. The main differences being that the experimental setup consisted of only a single nozzle,

Table 3.1: Levels of Test Parameters

Parameter Level	Height (mm)	Distance to Ramp (mm)	Pressure (kPa)
1	52.58	67.06	827
2	49.53	75.18	758
3	46.74	83.06	689
4	43.94	91.19	621
5	41.15	99.06	552

the ramp is flat for ease of manufacturing as well as modeling, and one larger filter area is present on the top wall. The front wall of the collection system was manufactured from polycarbonate to allow for full viewing in the high speed imaging.

The collection system height, distance to the ramp, and nozzle inlet pressure were varied throughout the bench top testing. The aim of the experiments was to collect data through high speed imaging as well as the amount of mass collected in each arrangement. A Taguchi array [5] was used in the design of experiments to most efficiently test each of the variable parameters. Each parameter had five levels to test as shown in Table 3.1. A Taguchi design array insures that each level of each parameter appears the same number of times throughout the experiment and that repetition of each parameter-level combination is minimized as much as possible. An orthogonal Taguchi array was chosen to investigate

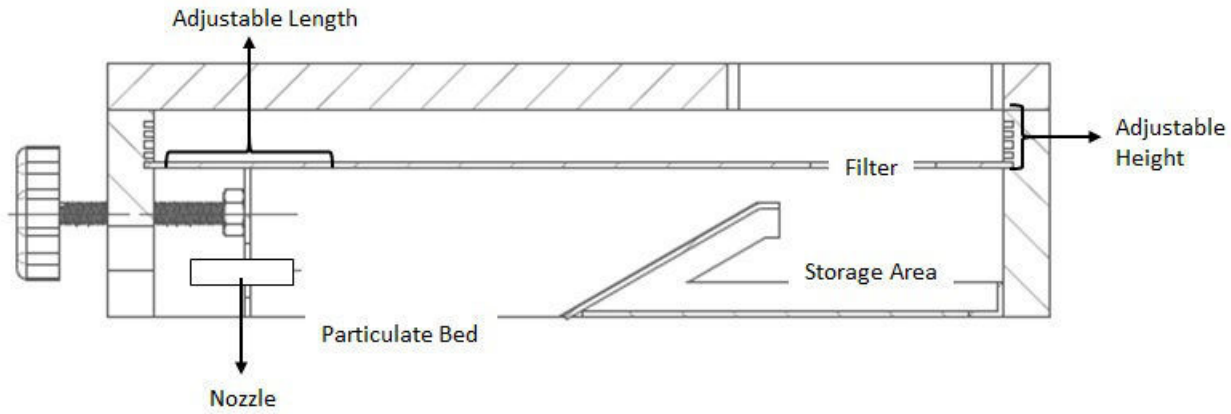

Figure 3.1: Adjustable particulate collection system for high speed testing.

the effects of each of the parameters on the amount of particulate collected. An orthogonal array states that for each level of a particular parameter, all levels of each of the other parameters are tested at least once. This resulted in a total of 25 different combinations of the parameters as is shown in Table 3.2. In order to achieve greater accuracy in the experiments three trials were run at each combination resulting in a total of 75 experiments. The adjustable collector system was placed on a leveled bed of sand at the start of each experiment. The bed of sand exhibited an average particle size of 500 μm and a bulk density of 2000 kg/m^3. A 20 gallon compressor charged to the desired inlet pressure was used as the supply. A solenoid valve was then activated to release the air for 1.5 seconds; the large tank size allowed the system to operate at a semi-steady state for the set length of collection time. The total mass collected was recorded for each of the experiments and averaged across all three trials for each run.

Table 3.2: Orthogonal Taguchi Array

Run #	Height	Distance to Ramp	Pressure	Run #	Height	Distance to Ramp	Pressure
1	1	1	1	16	4	1	4
2	1	2	2	17	4	2	5
3	1	3	3	18	4	3	1
4	1	4	4	19	4	4	2
5	1	5	5	20	4	5	3
6	2	1	2	21	5	1	5
7	2	2	3	22	5	2	1
8	2	3	4	23	5	3	2
9	2	4	5	24	5	4	3
10	2	5	1	25	5	5	4
11	3	1	3				
12	3	2	4				
13	3	3	5				
14	3	4	1				
15	3	5	2				

The analysis of the results was then performed by the techniques proposed by Taguchi in order to determine the effects of the system height, distance to the ramp, and inlet pressure on the amount of particulate collected. Level averages were calculated, which are defined as the average value of the mass collected at each level of a specific parameter. For example, the amount of mass collected each time the height was at the lowest level is averaged as a single value. This process is repeated for each level of each parameter. The results of the level averages for each parameter are shown in Figures 3.2, 3.3, and 3.4. The error bars in each plot represent one standard deviation of the averaged samples. It should also be noted that the average standard deviation of the three trials at each configuration was 1 g with a maximum of 2.5 g.

The levels of each parameter are in reference to those stated in Table 3.1. The data exhibits good correlation between the amount of mass collected and the height of the collection system as well as the distance to the ramp as shown in Figure 3.2 and Figure 3.3,

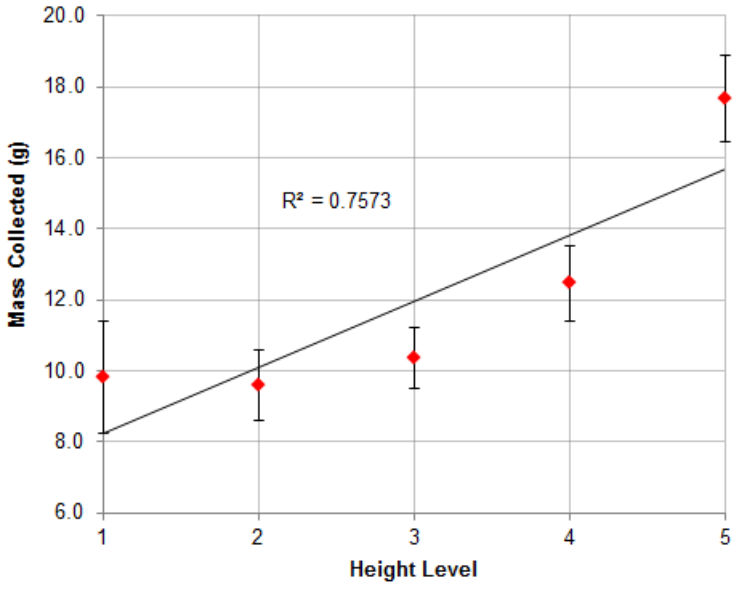

Figure 3.2: Experimental results show strong correlation between the amount of mass collected and the height of the system.

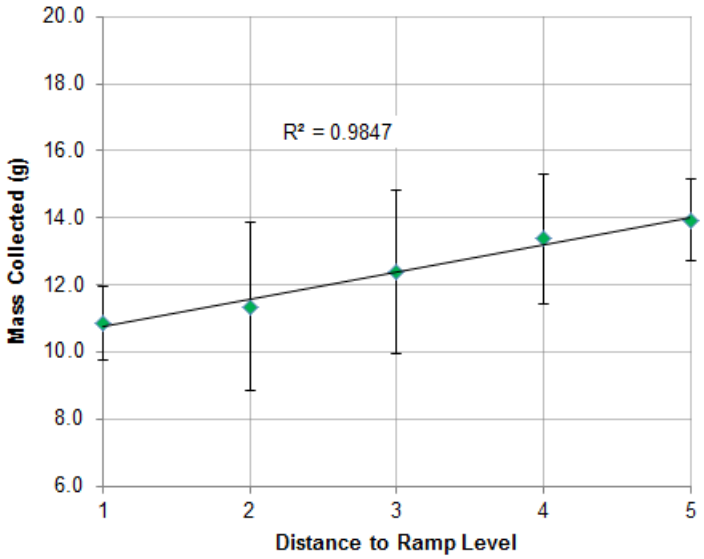

Figure 3.3: Experimental results show strong correlation between the amount of mass collected and the distance to the ramp.

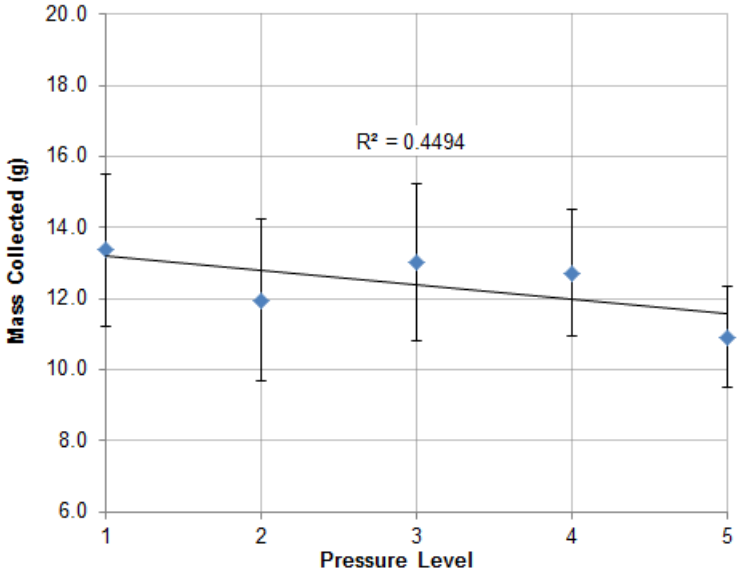

Figure 3.4: Experimental results show little correlation between the inlet pressure and the amount of mass collected.

respectively. On the contrary, little correlation between the nozzle inlet pressure and the amount of mass collected is observed from Figure 3.4. This is most likely due to the fact that an increase in the nozzle inlet pressure has very little effect on the system as the flow is choked through the nozzle. The air velocity through the nozzle cannot increase any further with an increase in the pressure level; only the mass flow rate through the nozzle will increase.

From the experimental results it can be concluded that decreasing the height, effectively changing the area between the top of the ramp and the top of the collector, will increase the amount of mass collected within the range tested. Also, increasing the length, the distance between the nozzle and the start of the ramp, will also increase the amount of mass collected within the range tested. As previously stated, no correlation can be stated between the nozzle inlet pressure and the amount of mass collected. These trends as well as the flow characteristics visualized with the high speed video were attempted to be replicated utilizing CFD.

3.2 FLUENT Analysis

The process of simulating the particulate collection system can be broken down into two stages; the 2D environment and the 3D environment. The first stage of simulations were executed in the 2D environment where a strategic approach of model changes was employed. The first stage is shown as the cases on the left side of Figure 3.5. A clear progression can be seen through the cases and will be described in more detail in section 3.2.1. The second stage took place in a 3D environment. The knowledge gained through the 2D studies was applied to 3D simulations to begin. Then the model was modified one parameter at a time in an attempt to accurately represent the bench top testing previously conducted.

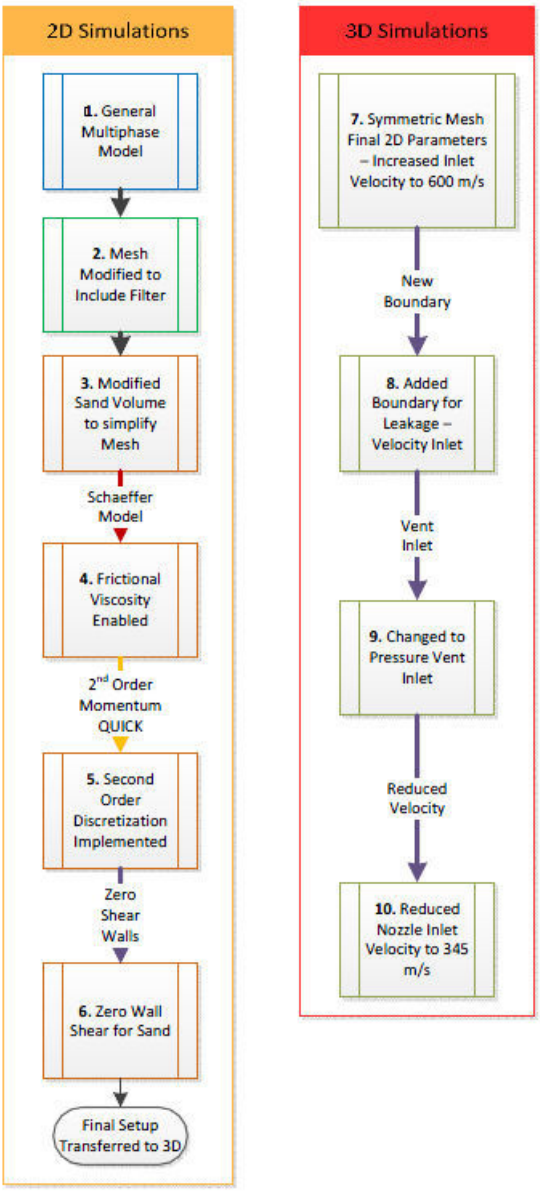

Figure 3.5: Flowchart of FLUENT simulations during the study of the particulate collection system.

3.2.1 Stage One - 2D Simulations

The first stage of simulations was performed in a 2D environment. The goal was to experiment with different models to find a set that would most accurately portray the dynamics seen through the high speed image testing. The mesh as well as the model selections were changed in a strategic manner to analyze the effects of each change. The final set of models found through the first stage were then transferred into a 3D environment for further simulation.

3.2.1.1 General Multiphase Model

Initially the parameters found during a fluidized bed study as were implemented. This was the starting point for the 2D case as well as a generic mesh to represent one setting of the adjustable collection system as shown in Figure 3.6. The lower rectangle represents the sand or particulate region while the upper rectangle encompasses the internals of the collection

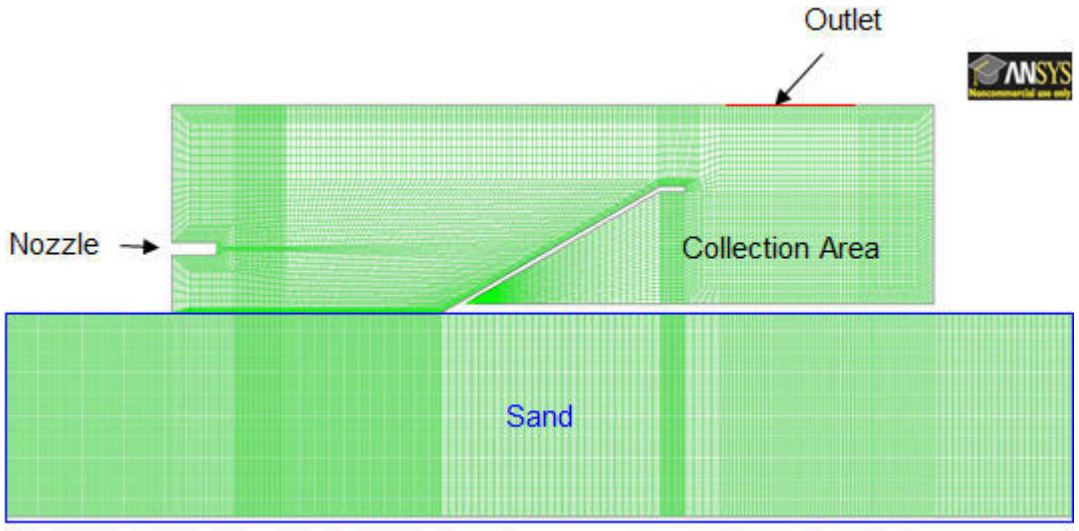

Figure 3.6: 2D mesh created to represent a side view of the collector sitting on a bed of particulate or sand.

system. The nozzle can be seen on the left upper side of the mesh. The boundary conditions consist of a 345 m/s velocity inlet at the tip of the nozzle and a zero gauge pressure outlet at the top right side of the collection area. The inlet velocity was chosen due to the flow being choked through the nozzle and therefore at Mach 1. The Eulerian two-phase model was used with a k-epsilon turbulence model as detailed in section 2.3.1. For more details on the case parameters reference the "Model Parameters Summary" spreadsheet in Appendix A. This case showed promising results in that the particulate was entrained into the flow and transported up the ramp. However, the particulate was exiting the collection area through the outlet as it remained in the air stream as seen in Figure 3.7 (the blue color represents the sand).

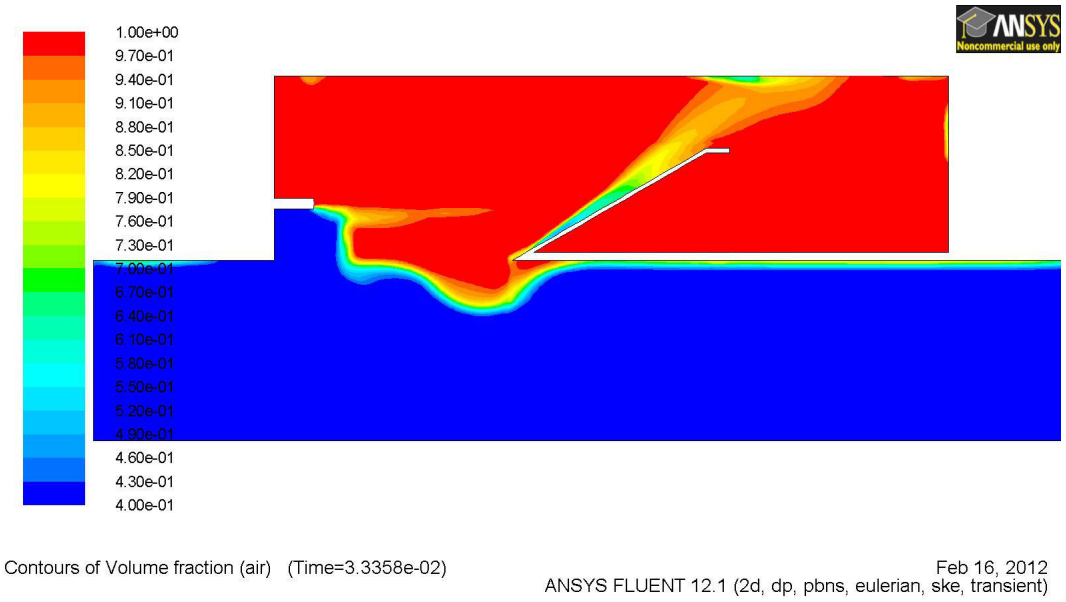

Figure 3.7: Case 1: Original 2D simulation utilizing parameters found through a fluidized bed study.

3.2.1.2 Geometry Modified to Include Filter

The first case showed entrainment and transportation of the particulate. However, the particulate was carried in the air flow through the outlet boundary. This contradicts the experimental system in which the particulate would contact a filter and drop out of the air stream into the collection area. A porous zone was utilized to model a filter to prevent the particles from escaping. The geometry was modified to include a new zone above the outlet as shown in Figure 3.8. The grid resolution was maintained with the only change being the addition of the new zone and all model parameters were held constant from the first case. The boundary conditions for the filter zone was selected to be porous with a fluid porosity of 0.8. Then the viscous resistance and inertial resistance were set independently for each phase; sand and air. Values for the resistances of the filter were found through flow bench testing of the real system. Once the filter was implemented, the particulate was prevented from exiting the collection area and the particulate accumulated on the face of the filter as would be expected. This result can be seen in the image of contours of volume fraction in

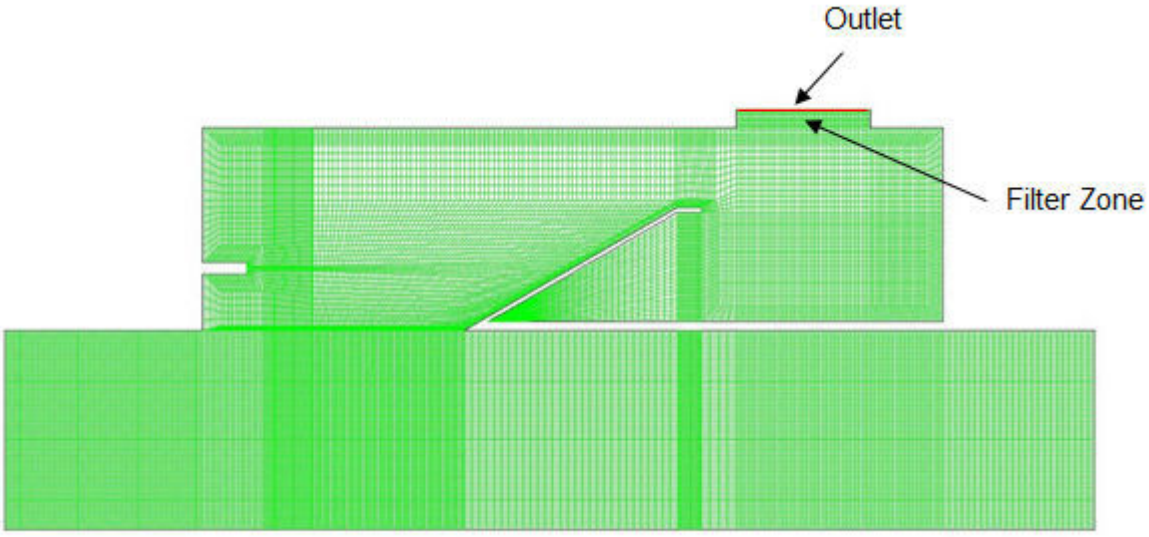

Figure 3.8: Modified 2D mesh for geometry including a filter zone.

Figure 3.9 after 35 ms of flow time.

3.2.1.3 Modified Sand Volume to Simplify Geometry

In an effort to decrease the simulation time the geometry was simplified and unnecessary areas were removed. As can be seen in the image of contours of volume fractions in case two, Figure 3.9, the lower half of the particulate area remains unaffected. Also, to further simplify the geometry, the protruding nozzle section was removed and the nozzle opening was specified as flush with the left wall of the collector. The resulting mesh is shown in Figure 3.10. A similar grid resolution was used in creation of the mesh. The case parameters remain unchanged and the simulation was run again. The results shown in Figure 3.11 are very similar to those as seen in the second case. The geometry changes did change some of the flow patterns, but the particulate was still entrained and transported. As a result, the simplified geometry was used for further studies on model changes and comparisons. The

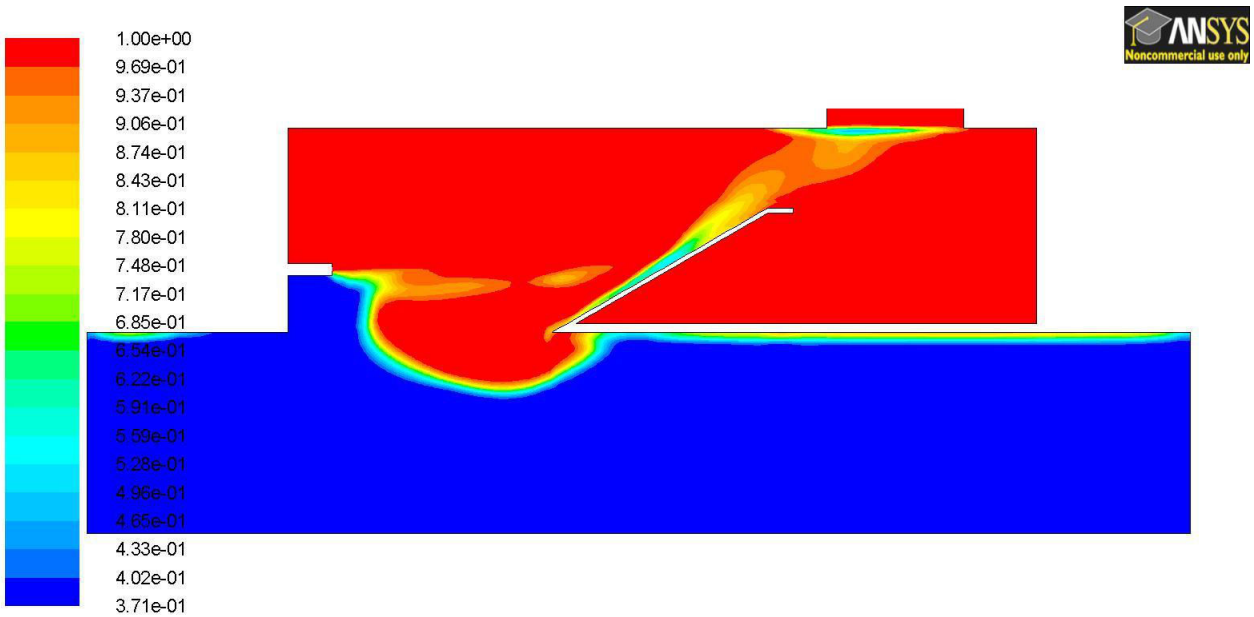

Figure 3.9: Case 2: Contours of volume fraction of air with the addition of a filter.

resulting volume fraction contour plot is shown in Figure 3.11 after 40 ms of flow time.

3.2.1.4 Frictional Viscosity Enabled

A fourth case was used to investigate the effects of including a Schaeffer frictional viscosity model. Including this model greatly affected the entrainment and transportation of the particulate. The particulate appeared to be pushed up the ramp as opposed to primarily being entrained into the air stream and blown onto the ramp as is illustrated in Figure

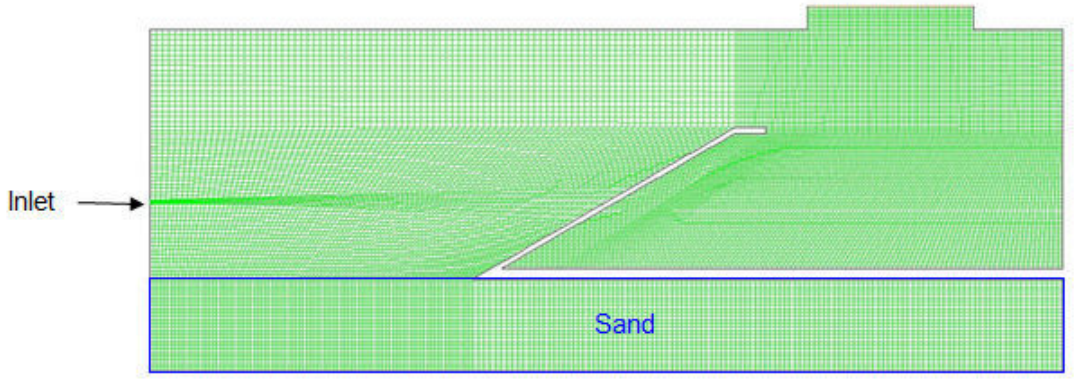

Figure 3.10: 2D mesh for simplified geometry to eliminate unnecessary areas and improve simulation times.

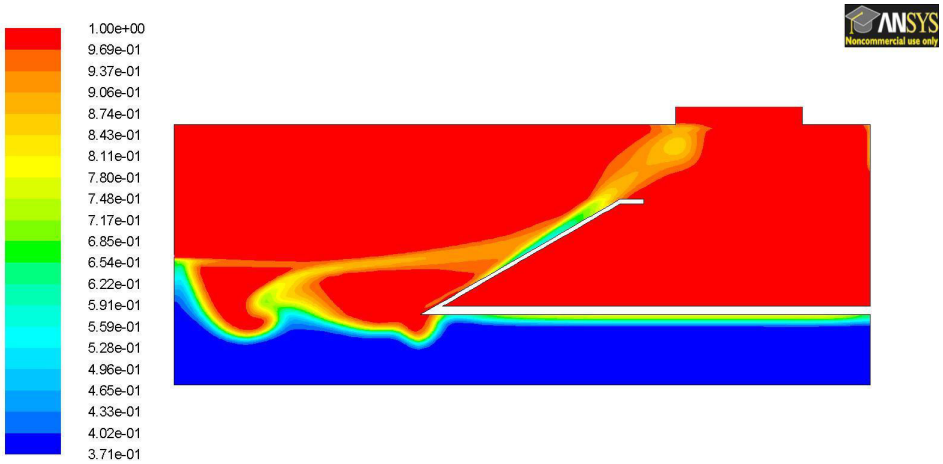

Figure 3.11: Case 3: Contours of volume fraction of air after simplifying the geometry.

3.11. A comparison between the original parameters and the addition of frictional viscosity is illustrated in Figure 3.12. The change is very evident and more closely represents what was seen during the bench top testing high speed videos.

3.2.1.5 Second Order Discretization Implemented

The parameters remained the same from Case 4 however a second-order discretization was implemented for momentum as well as the quadratic upwind interpolation for convective kinematics (QUICK) scheme for volume fraction. The aforementioned changes for Case 5 produced noticeable results in the development of the flow. The entrainment and transport of the particulate exhibited a more random nature. Sections or groupings of particulate

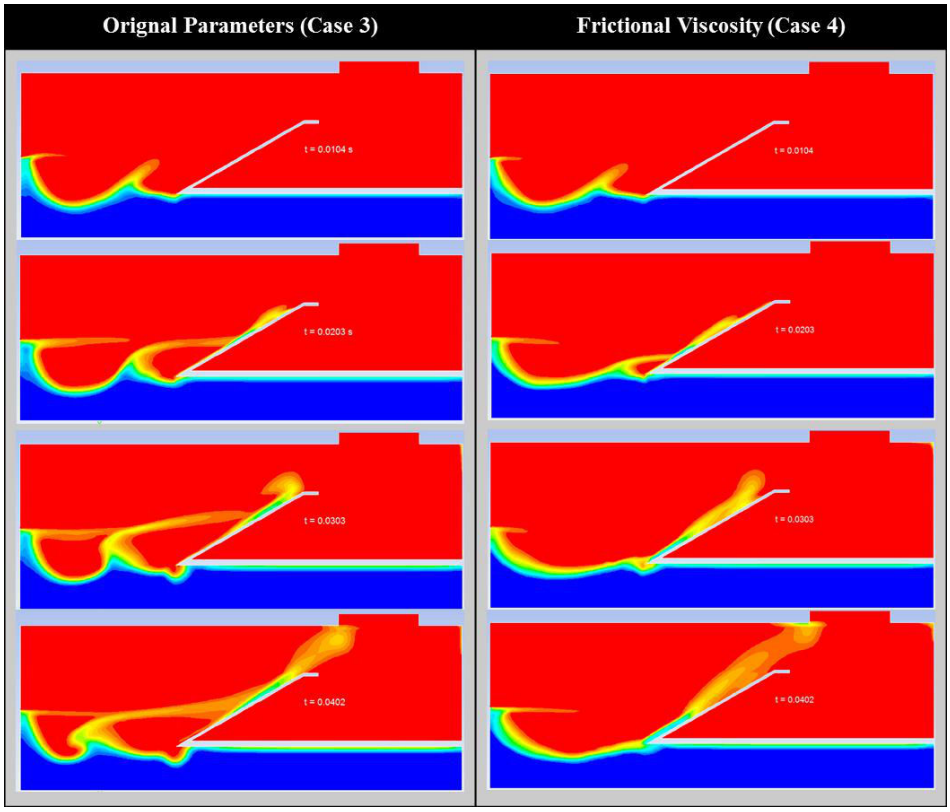

Figure 3.12: A comparison of the results between the original parameters (Case 3) and the addition of a frictional viscosity model (Case 4).

deviated from the main stream flow as it was transported up the ramp. Once again the results appear to be closer to what was observed in the high speed videos of the bench top testing. A comparison with case 4 is shown in Figure 3.13.

3.2.1.6 Zero Wall Shear for Sand

In the previous cases a no-slip boundary condition had been used for both the sand and the air. This is a commonly used assumption for air, but not very realistic for the particulate. The wall boundary conditions for the sand were then changed to allow a specified shear of zero in both the x- and the y- direction. The change in the solid particle boundary condition prevented the amount of build-up of particulate on the ramp as well as the back wall of the

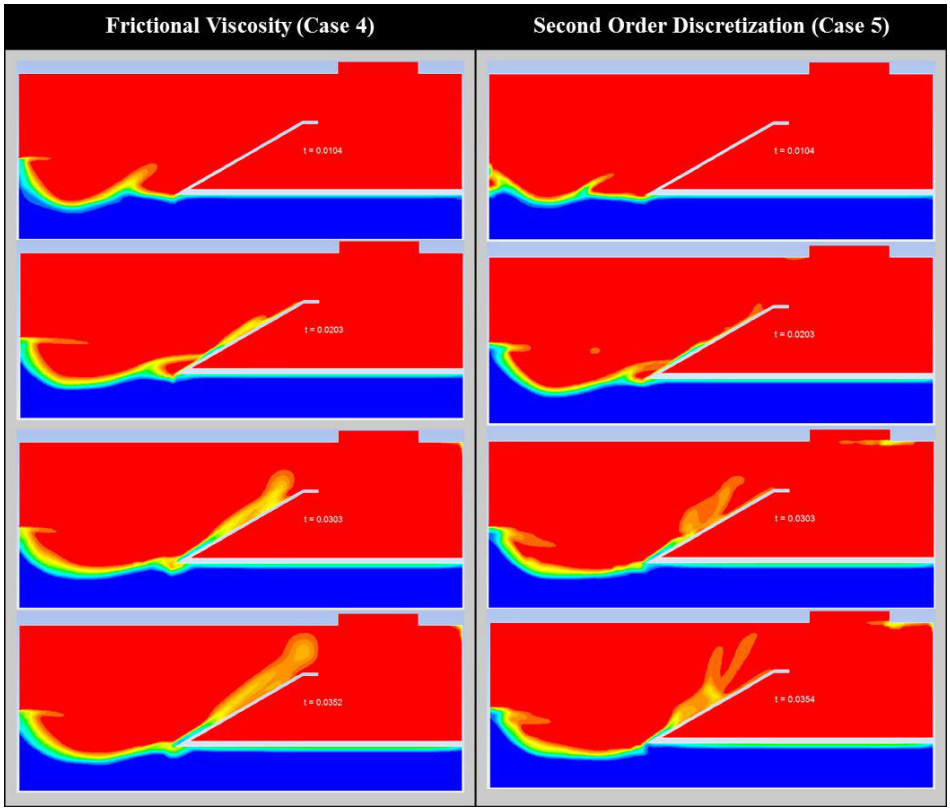

Figure 3.13: A comparison of the results between the addition of frictional viscosity (Case 4) and utilizing a second-order discretization for momentum (Case 5).

collection area. The results as compared to Case 5 are shown in Figure 3.14. It is clearly seen that the particulate moves up the ramp much faster and does not collect on the face of the filter. In the last frame it is also apparent that the particulate drops down into the collection area as was seen in the experiments.

Case 6 concluded the studies in the 2D environment. The entrainment and transportation of the particulate accurately represents the behaviors seen in the bench top testing. As a result, the models and parameters were transferred to a 3D environment to further validate the simulations.

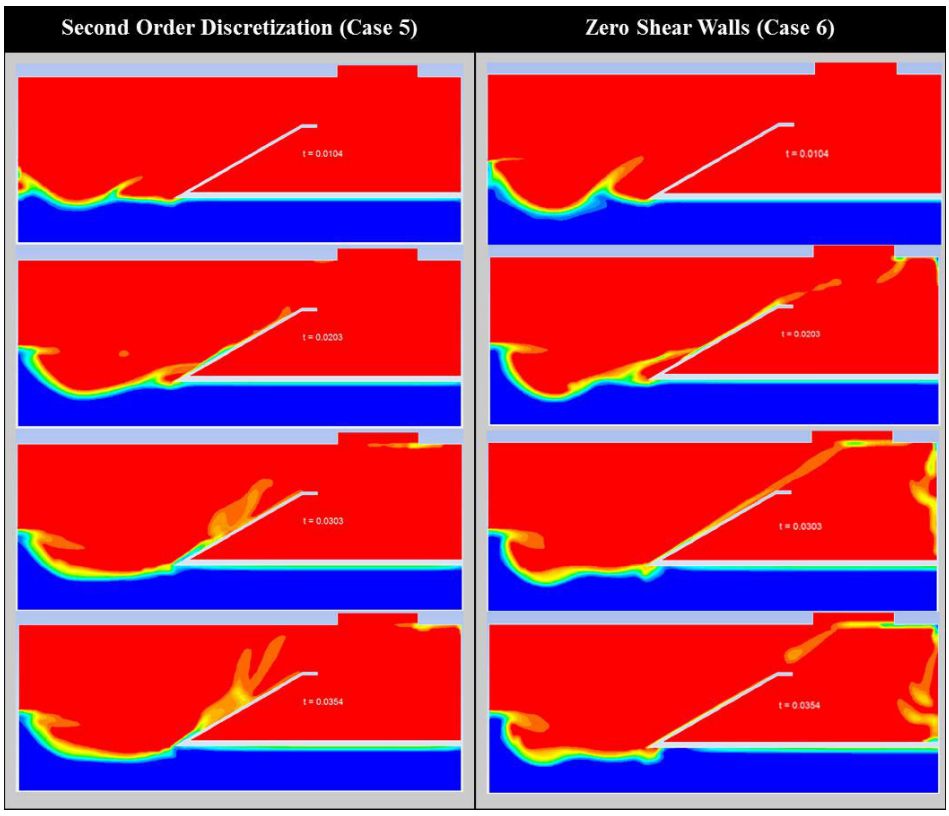

Figure 3.14: A comparison of the results between Case 5 and the addition of a zero shear wall boundary condition, Case 6.

3.2.2 Stage Two - 3D Simulations

The second stage of simulations was performed to more accurately represent the experimental testing performed by taking into account the three-dimensionality. Initially, problems were encountered with the simulations and a strategic approach was employed to modify the models and the mesh. Ideally, the amount of mass collected would be recorded through simulations and compared to the experiments. (However, due to the complexity of the simulations this was not able to be achieved.) The final case provided promising results in that the dynamics of the system could be captured.

3.2.2.1 Symmetric Mesh with Final 2D Parameters

A mesh with consistent grid resolution as the 2D cases was created in 3D, and is displayed in Figure3.15. The area outlined in green represents the collector, the area outlined in orange represents the particulate or sand, and the yellow plane outlined in red marks the symmetry plane. The lighter red area on the top of the collector is the outlet of the filter. This case was initially run with all of the same parameters as the final 2D case (Case 6). No particulate entrainment, and as a result no transport, was seen after the initial simulation. As a result, the inlet velocity was increased to 600 m/s in an attempt to remedy the issue. However, after simulating for 40 ms of flow time, the air velocity field had appeared to be fully developed without any entrainment of the particulate. Contours of the air velocity plotted on the symmetry plane is shown in Figure 3.16(a). Contours of the volume fraction of air were then examined as seen in Figure 3.16(b) plotted on the symmetry plane. Finally, contours of the y-velocity of the sand as plotted on the symmetry plane are shown in Figure 3.16(c). The velocities transferred to the sand by the air stream were not enough to begin any movement of the sand. After closer examination of the test bench case it was proposed that potentially

the leakage around the base of the collector allowed air flow near the surface of the sand to form and begin the entrainment process. In contrast, the system is completely sealed in the model and a new case included leakage.

3.2.2.2 Boundary for Leakage – Velocity Inlet

The geometry from Case 7 was modified to create a new boundary condition. A row of cells along the backside of the collector was defined as an inlet, shown by the blue outline in Figure 3.17. Once again all of the model parameters remained the same with an inlet velocity of 600 m/s at the nozzle. The first test case was run with a leakage inlet velocity of 1% of the nozzle velocity or 6 m/s. The simulation was run for 36 ms and the results were examined. The nozzle air velocity profile remained the same as was seen in Case 7, however the addition of the leakage inlet did begin the particle entrainment process. A contour plot

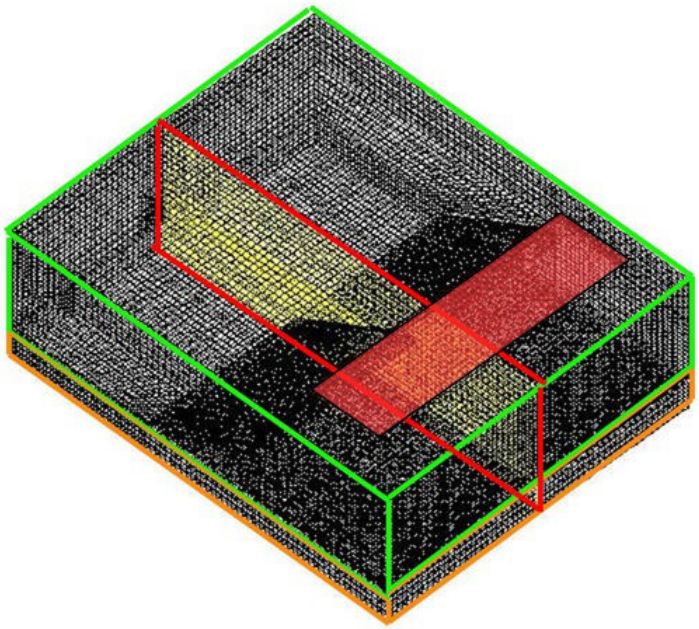

Figure 3.15: Modified 3D mesh to eliminate unnecessary volume in the sand region.

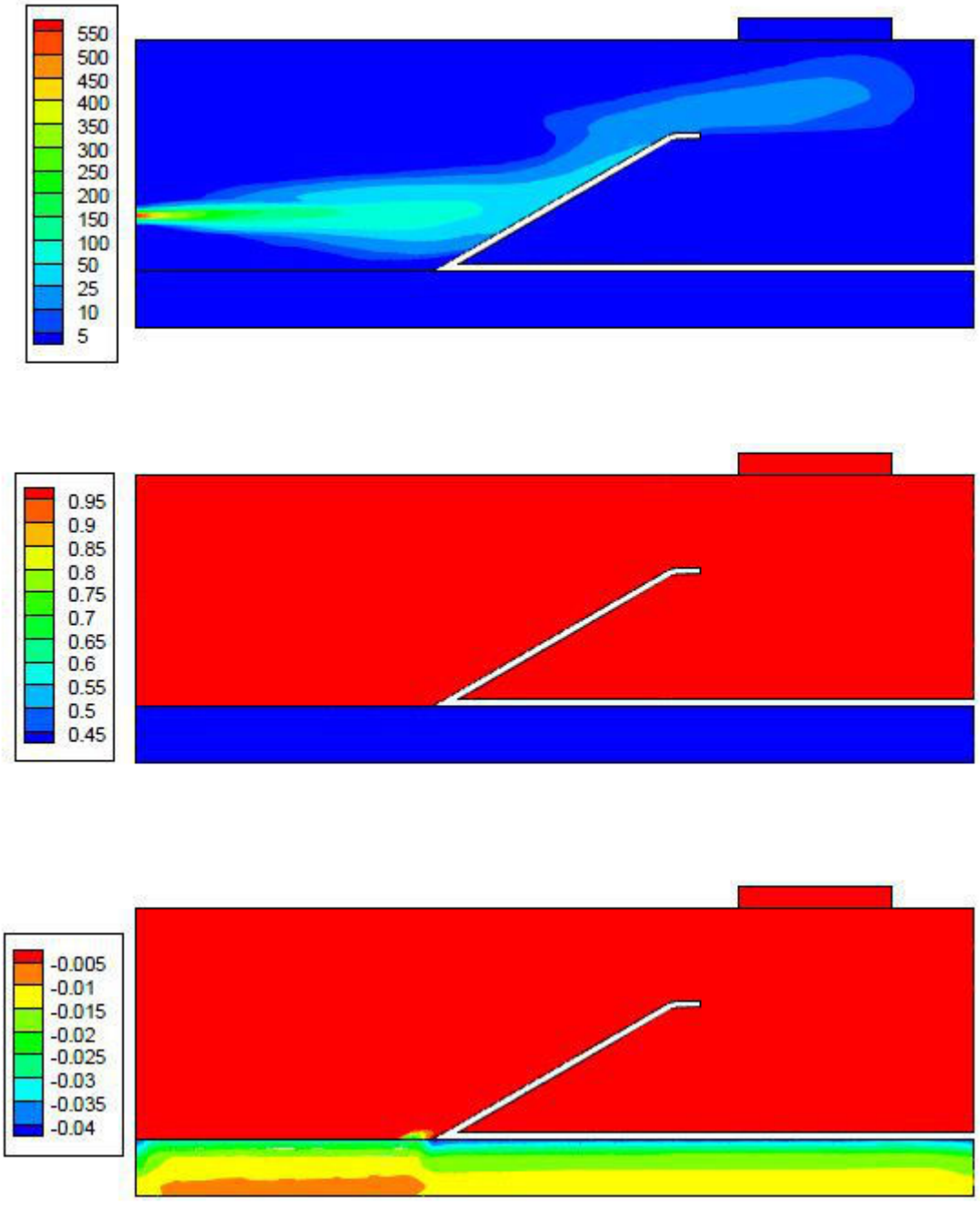

Figure 3.16: All plots represent the simulated flow after 41 ms of time. The top plot (a) shows contours of air velocity plotted on the symmetry plane. The middle plot (b) illustrates the air volume fraction contours. The lower plot (c) shows contours of the sand velocity in the y-direction.

of the volume fraction of air as plotted on the symmetry plane is shown in Figure 3.18. The particulate began to travel up the ramp and a small amount was entrained in the flow. To further improve on this idea of a leakage inlet and more closely represent the bench top system, the velocity inlet boundary condition was changed to a vent inlet condition. Instead of inducing a fictional velocity the system would act as though it would experimentally and pull air through the leak as the flow develops.

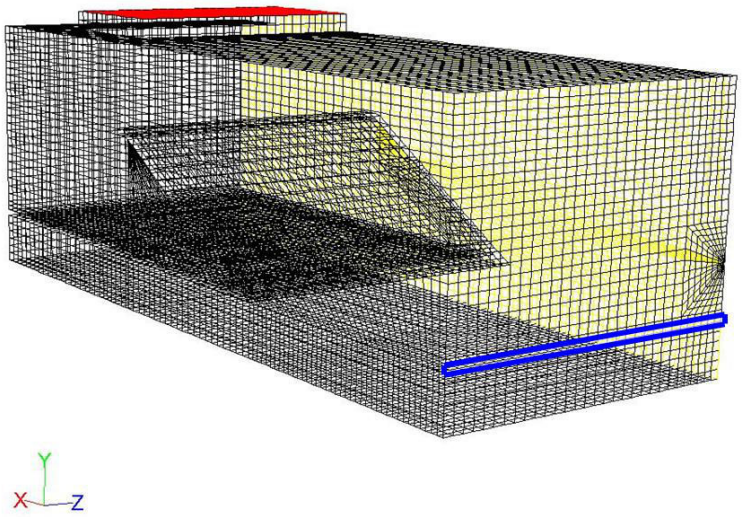

Figure 3.17: 3D mesh modified to include a new zone for a leakage inlet.

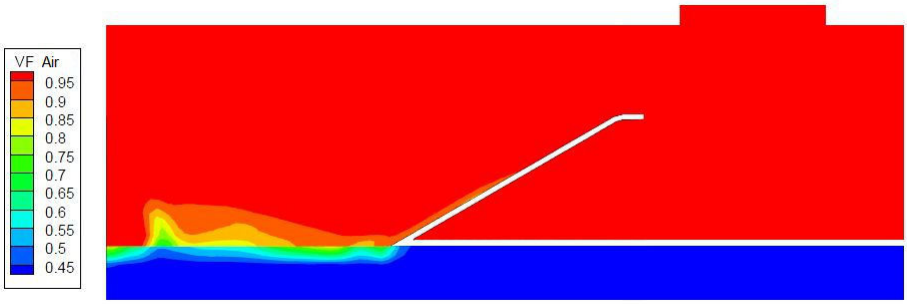

Figure 3.18: Case 8: The addition of a velocity inlet at the boundary of the air and sand volume in the 3D case results in particle movement.

3.2.2.3 Boundary for Leakage - Pressure Vent Inlet

The leakage inlet on the back wall of the collector was changed from a velocity inlet to a pressure vent inlet set at zero gauge. The case was simulated for 24 ms of flow time and the results examined. The particulate began the entrainment process as seen previously with Case 8. Contours of the volume fraction of air on the symmetry plane can be seen in Figure 3.19 for the pressure inlet boundary condition. It should be noted that the nozzle inlet velocity still remained at 600 m/s at this point. Therefore to accurately represent the experiment the nozzle velocity was reduced to 345 m/s.

3.2.2.4 Reduced Nozzle Inlet Velocity

The nozzle inlet velocity was reduced to 345 m/s as was used in the 2D simulations. All other parameters remained unchanged and the case was simulated for 25 ms. The results remained the same and the particulate began the entrainment process as previously seen. Contours of the volume fraction of air as plotted on the symmetry plane are shown in Figure 3.20. This case exhibits very promising results as it appears the particulate will begin being transported up the ramp. However, due to the complexity of the case each time step requires approximately 20 seconds to converge. The time step size is set to 0.01 μs seconds

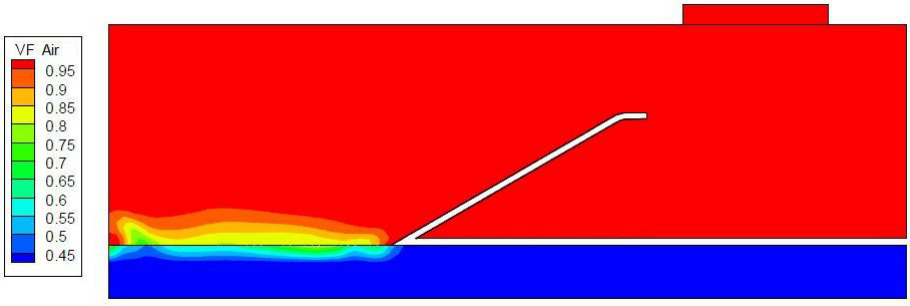

Figure 3.19: Case 9: The change from a velocity inlet to a vent pressure inlet produced similar results.

for consistent convergence. As a result, to achieve 100 ms of flow time it will require 2000 days at the current rate. It is hard to make any conclusions at this stage due to not having enough simulation data to compare to the bench top experiments.

3.2.3 CFD Simulation Results

The 2D simulations exhibited positive results, the particulate was entrained and transported to the collection area. The 2D cases also provided the opportunity to quickly study the effects of model and parameter changes on the movement of the particulate. Although, to accurately compare to the bench top experiments, a 3D simulation was needed. After some initial troubles with the 3D simulations, the particulate began moving and entrained within the flow. However, due to the high velocity of the air stream, the complexity of the mesh, and utilizing multiphase models in conjunction with turbulence models, the case is computationally intensive. It is also difficult to confirm that the simulation accurately represents the testing completed experimentally due to the minimal amount of flow time completed. As a result, a method of decreasing the computation time either through model and parameter changes or through processing power needs to be found to continue the 3D simulations.

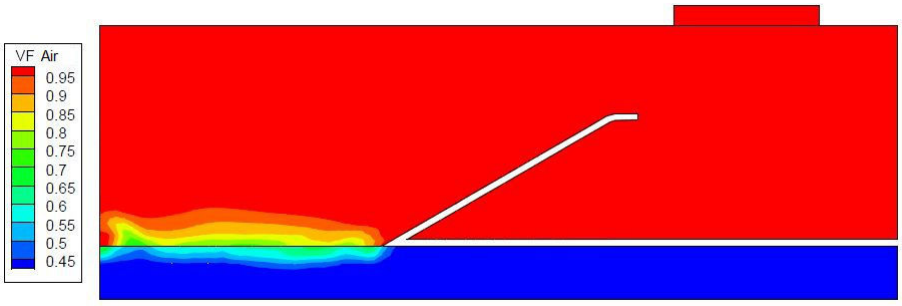

Figure 3.20: The reduced nozzle inlet velocity had very little effect on the movement of the particulate.

Comparison with high speed video shows similar characteristics in the simulated air and particulate flow patterns. Figure 3.21 shows a side by side comparison between frame captures of the high speed video and the final 2D simulation. In frame one the jet impingement on the particulate bed can clearly be seen in both the simulation as well as the high speed frame capture. The flow from the jet impacts the particulate bed transporting particles upwards into the collection chamber. The next frame illustrates the particles being entrained into the flow and carried up the ramp. Frame three shows that the originally impacted portion of the particulate bed is becoming uniform again and the primary movement of the particles is following the profile of the ramp. Recirculation of the particles in the col-

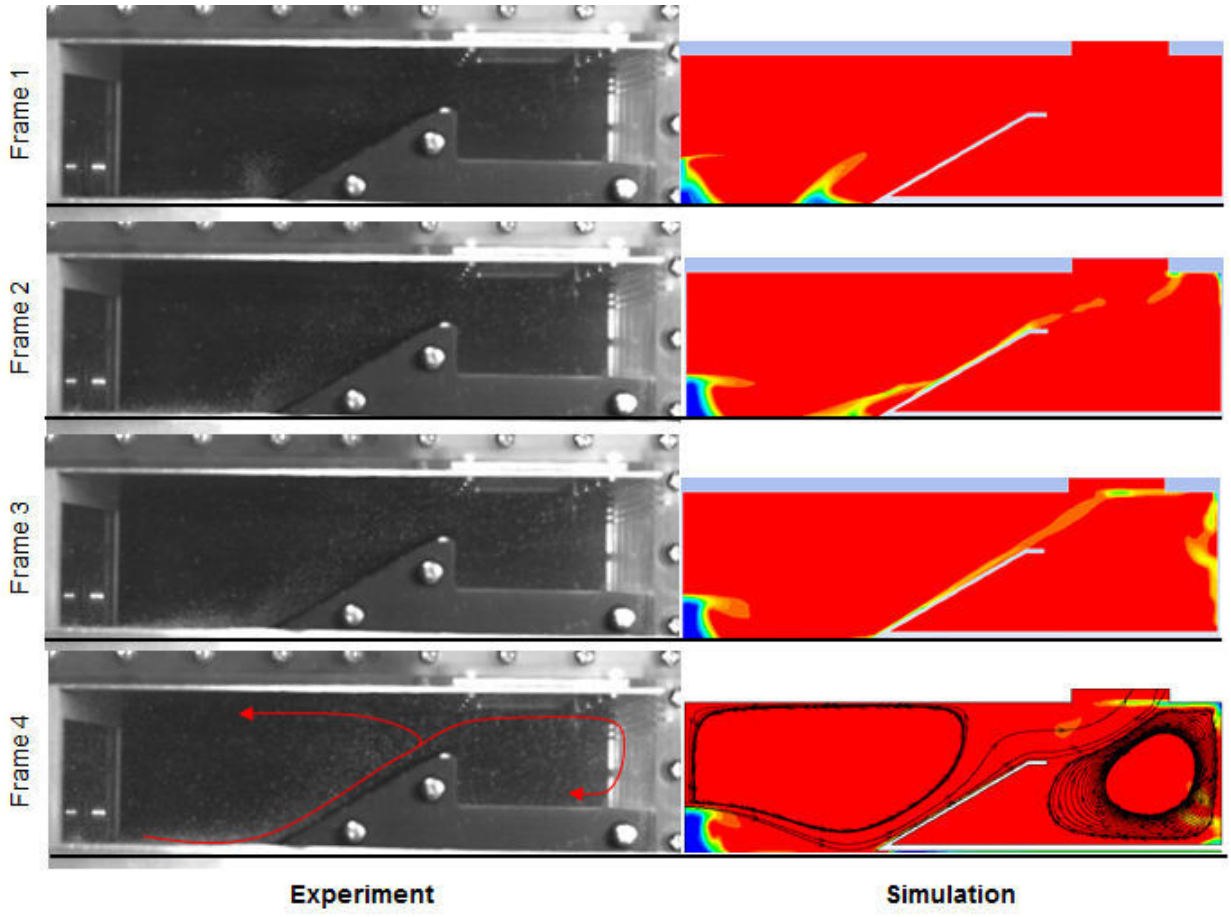

Figure 3.21: Comparison of high speed videos with final 2D FLUENT simulation.

lection chamber as well as the sampling chamber has begun. Finally, in frame four the flow has developed further and the particles are recirculating in both chambers as shown by the red arrows in the high speed frame capture. Particulate is carried back towards the nozzle wall and the high density of particles in the collection chamber is due to the recirculation. The black lines in frame four of the simulation represent velocity path lines of the air and confirm the patterns seen in the high speed video.

The analysis of the high speed video and the simulation provided sufficient information in that undesirable flow characteristics were a result of the design of the PCS. The nozzle was positioned parallel to the particulate bed in an attempt to utilize the mechanism of particle entrainment as the method of transport. However, it was found that the jet impinged the particle bed due to the spread of the jet flow. Critical energy is wasted during this process as the particles are not being transported in the desired direction. Also, large recirculation regions in the collector were found through the simulations and the high speed video. The recirculation of the flow carried particles up the ramp and back towards the nozzle wall and as a result wasting valuable energy. If the recirculation is eliminated or reduced, the amount of compressed air used could be reduced to produce the same collection results. CFD proved to be a valuable tool in predicting the flow characteristics of the PCS and will be utilized to improve the design.

Chapter 4.

Particulate Collection System Design and Testing

The particulate collection system is comprised of two main components: the energy storage device and the collection device. Each component serves a critical role in particulate collection and were examined for areas of improvement.

4.1 Pressure System

The compressed air tank of the previous PCS design provided 2.8 seconds of flow time while remaining above the critical pressure, resulting in choked flow. Although the velocity through the nozzle remained at Mach 1 while above the critical pressure, the density of the air was constantly changing while the tank was depleted of air. Examining Equations 2.5 and 2.4 shows that the gas density is a critical parameter when determining the pickup velocity of the particulate. Initially, when the pressure is high the pickup velocity required is lower due to the increased gas density; as the pressure drops the density decreases and the pick up velocity becomes higher. This inconsistency creates a system that is difficult to design and

operate at optimum performance at all times.

The improved design will utilize carbon dioxide as the supply. Carbon dioxide can be stored at very high pressures and stored in a saturated liquid form. Therefore, as the gas is released the saturated liquid evaporates and maintains the pressure within the vessel. Unlike the compressed air tank, the carbon dioxide vessel supplies a constant pressure while it is depleted. The constant pressure allows the system to be designed for a quasi-steady state operation while the vessel contains saturated liquid. Another distinct reason for utilizing carbon dioxide is the increase in density. At atmospheric conditions carbon dioxide is 33% more dense than air which allows the system to operate at a lower velocity while maintaining the ability of particulate entrainment. While holding all variables constant other than the gas used for transport, carbon dioxide requires a minimum pick up velocity 23% lower than air. A lower collection velocity translates into a lower inlet pressure and ultimately a longer collection time.

4.2 Collector Design Features

The particulate collection system design was heavily influenced by the studies presented in the literature review as well as the conclusions drawn from the testing and analysis of the previous design presented in Chapter 3. The design was meant to closer replicate the particle entrainment and transport that has been studied (e.g., [7, 12, 13]). All of the studies performed were done in a fully developed turbulent flow that is parallel to the particle bed. In order to achieve these flow characteristics, a rectangular duct configuration with a diffuser was proposed as the basis of the design. To meet the size constraints set forth by the rapid prototyping machine, a bend was added to the rectangular duct to keep the system compact while allowing the flow to further develop. A basic schematic of the proposed system is

shown in Figure 4.1. The carbon dioxide enters the system through a 1.6 mm inner diameter hose at the inlet of the diffuser. It then expands through the pyramidal diffuser and develops throughout the rest of the rectangular duct. The collection area is at the lower side of the duct where a section of the bottom is removed. The particle storage area is directly after the collection area at the end of the duct. Finally, the very end of the duct is covered by a filter to release the carbon dioxide and retain the desired particles. The collector device would be comprised of multiple rectangular ducts allowing for a larger sample or multiple samples. However, only a single duct needs to be analyzed simplifying the design procedure. Several parameters of this design were studied in an attempt to achieve a fully developed velocity profile of the desired magnitude at the collection area. The parameters include: duct cross sectional sizing, bend radius, and diffuser angle. However, compromises were made in designing the system to meet the overall size constraints. The design of the system consisted of three stages:

1. Filter Testing - Three felt filters were selected with micron ratings of 25, 50 and 100. Each was tested in a basic pipe flow experiment to derive a pressure drop versus velocity

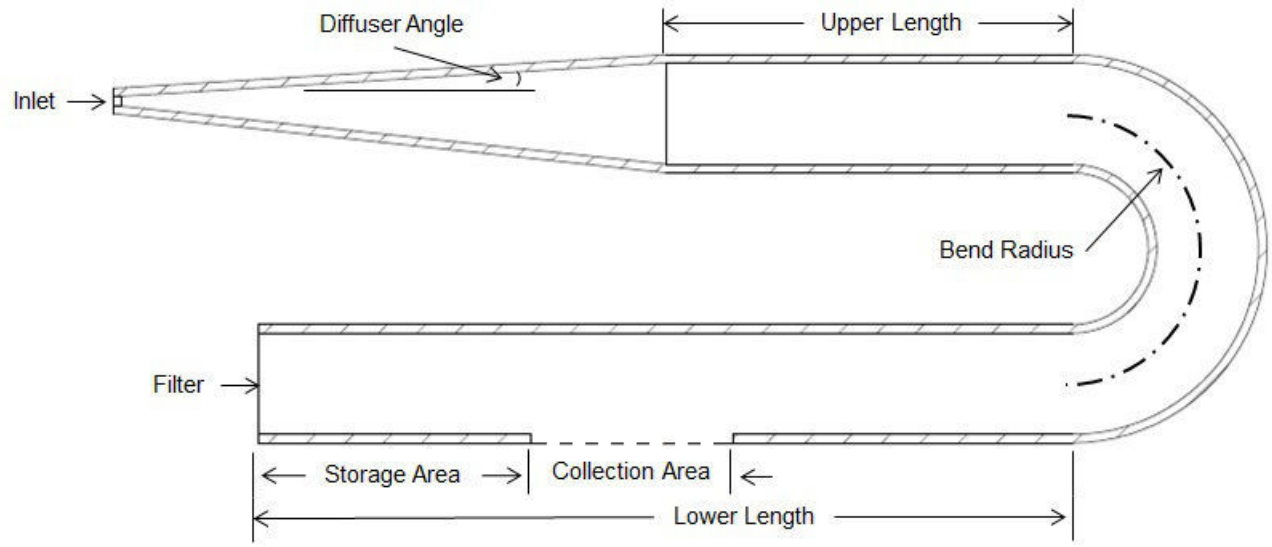

Figure 4.1: The basis of the collector design with variable parameters labeled.

curve. This curve allowed the filter to be characterized for analysis in both FLUENT simulations and fluids calculations.

2. Fluids Calculations - A combination of compressible flow and incompressible flow calculations were completed to determine the velocities, pressures, and temperatures at key points throughout the duct. The results allowed for validation of the FLUENT simulations in stage three as well as determining the inlet pressure required for the desired collection velocity dependent on the collector parameters.

3. FLUENT Analysis - An appropriate turbulence model was selected by conducting a study of turbulence models and comparing them with velocity profile data collected experimentally. The rectangular duct design was simulated with compressible turbulent flow models to study the effects of key parameter changes; specifically the diffuser angle and the bend radius. The boundary conditions were determined from the filter testing and the fluids calculations.

The final design parameters were selected as the design that most closely replicated a fully developed turbulent velocity profile at the collection area while meeting the size constraints. The design was experimentally tested and compared to the FLUENT simulations as well as the fluids calculations.

4.3 Filter Testing

The filter is an important piece of the collection system as it retains the desired particles while allowing the carbon dioxide to escape. As a result, the selected filters were characterized for the fluids calculations as well as the FLUENT simulations. An experiment was constructed to measure a range of velocities through the filter and the resulting pressure drop. The

experiment consisted of a six foot long, 3" SCH 40 PVC pipe fitted with a cap at one end to mount an array of nozzles and a flange at the opposing end. A second two foot long section of 3" SCH 40 PVC pipe was fitted with a flange. The filter was placed between the flanges and the flanges were bolted and sealed together. An air compressor connected to a pressure regulator and three nozzles was used to create the flow through the pipe. Dwyer 1/8" pitot-static tubes, part number 167-6-CF, were mounted 6" upstream and downstream of the filter to measure the velocity through the filter as well as the static pressure drop. A Setra differential pressure sensor, Model 264, was used to measure the velocity upstream the filter by connecting to the total pressure port and the static pressure port of the pitot-static tube. An Omega differential pressure sensor, PX278-01D5V, was connected to the two static ports of the pitot-static tubes to measure the pressure drop across the filter. The data was collected with a National Instruments myDAQ in conjunction with a Labview interface. A schematic of the test set up is shown in Figure 4.2 and a photo of the actual setup in Figure 4.3.

Before any filter testing was performed, the velocity profiles were measured across the pipe diameter, to correlate the center line velocity to the average velocity through the pipe

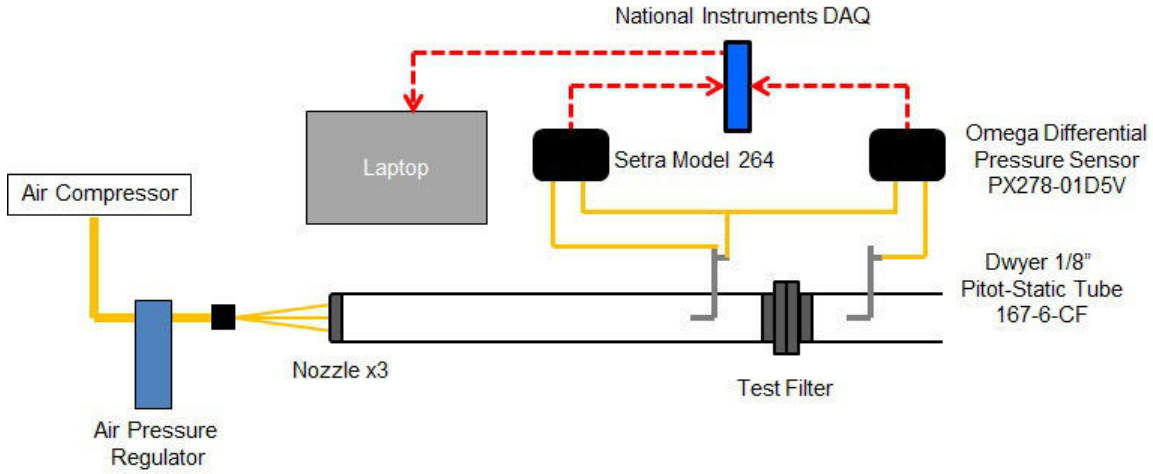

Figure 4.2: Filter experimental test setup schematic.

at each test setting. The full velocity profile was measured at a single setting to confirm symmetry through the pipe and then the rest of the measurements were taken for only one-half of the pipe diameter. The resulting velocity profiles are shown in Figure 4.4 for different inlet pressures. The error bars plotted represent one standard deviation. The data

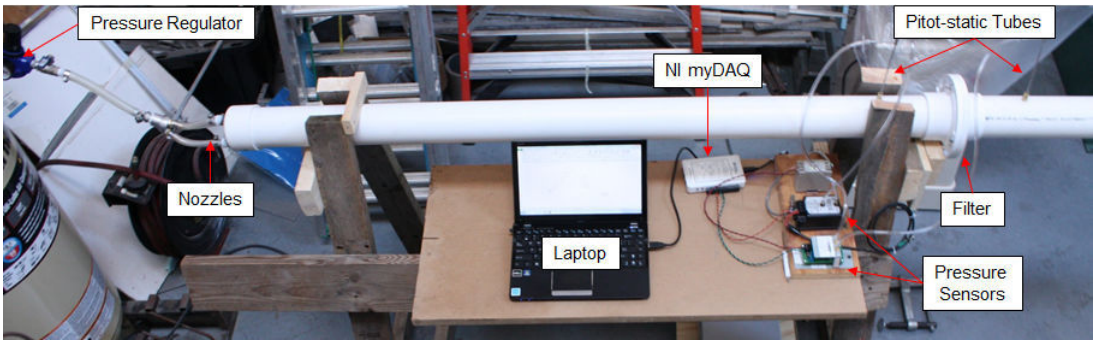

Figure 4.3: Filter experiment test bench.

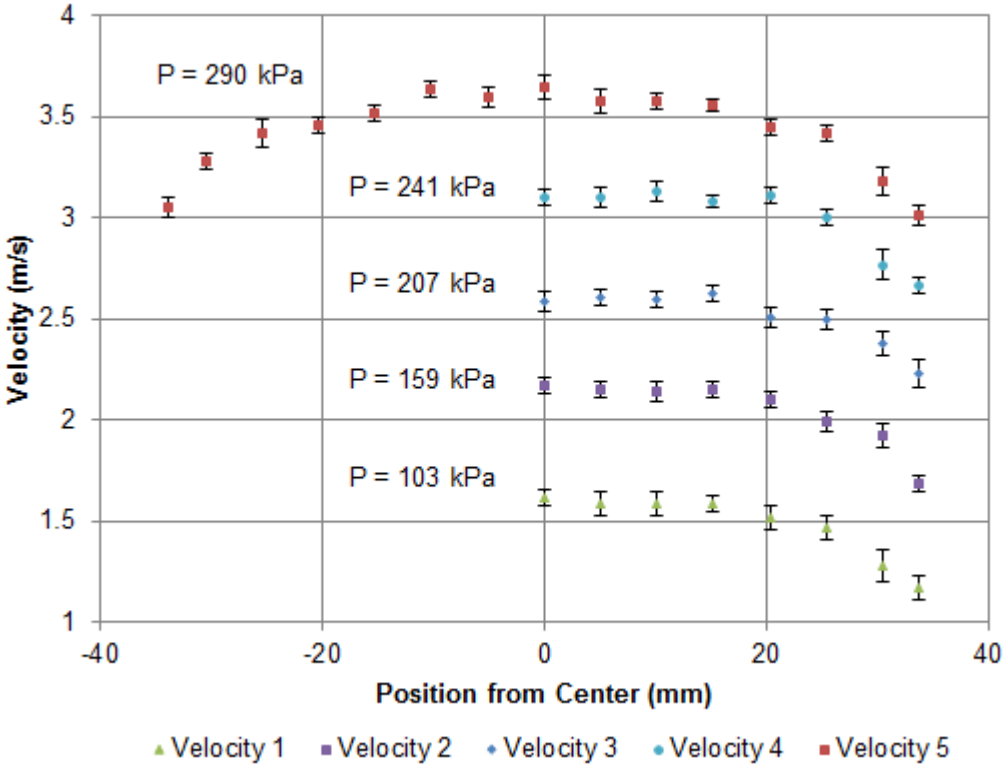

Figure 4.4: Velocity profiles measured at varying inlet pressures.

was collected at 1 kHz for 5 seconds and then filtered with a low pass filter with a cut off frequency of 50 Hz to prevent any electrical noise. The data was then averaged and the standard deviation was calculated. The inlet pressure of 290 kPa (Velocity profile 5) confirmed that the flow is symmetric through the pipe.

Knowing the velocity profiles allowed the velocity to only be measured at the pipe center line during the filter testing and related to the average velocity. It was intended to run the same five velocities for each filter and record the pressure drop across it. However, due to the increase in pressure because of the filter and the maximum pressure limit of the air compressor, the same velocities were not achieved. This was especially true for the case with the finest filter (25 μm rating). Even with these constraints, five velocities were tested for each filter and the pressure drop was recorded. The pressure drop for each of the filters plotted against the calculated average velocity is shown in Figure 4.5. The black curves

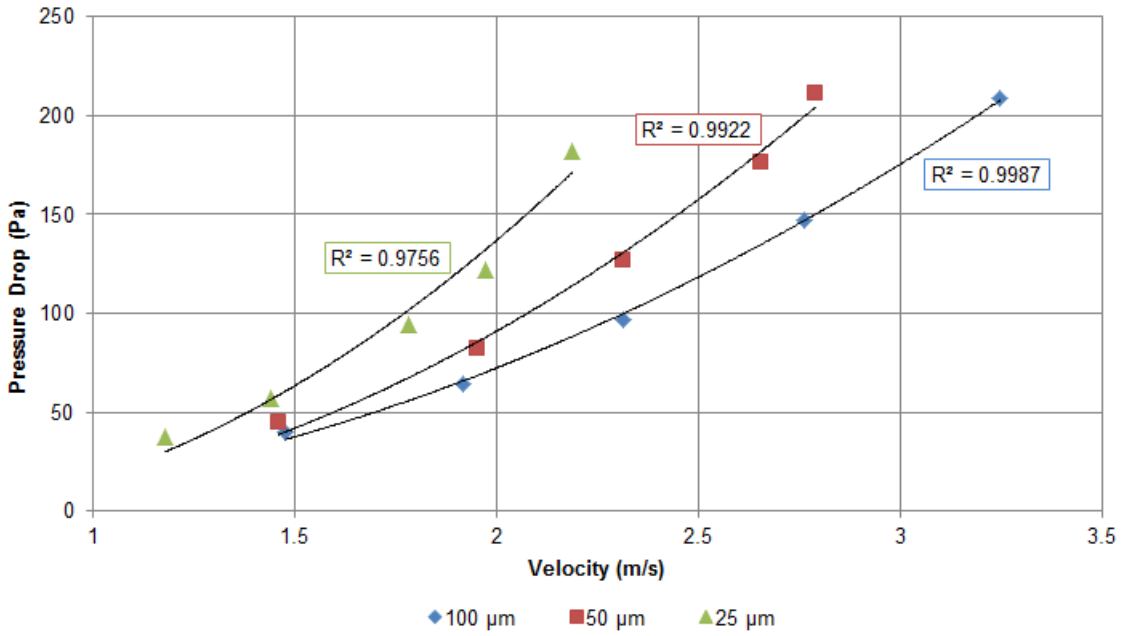

Figure 4.5: Measured filter pressure drops plotted against the average velocity.

represent a fitted trendline based on a second order polynomial regression of the form,

$$\Delta P = A \cdot V^2 + B \cdot V \tag{4.1}$$

where ΔP is the static pressure drop, V is the velocity, and A and B are constants. The R-squared values for each fitted line confirmed that the second order regression was a good fit. Equation 4.1 was used in the fluid flow calculations and the constants are used to derive the inertial and viscous loss parameters to input into FLUENT.

4.4 Fluids Calculations

The fluids calculations are divided into two main areas: compressible flow and incompressible flow. Initially the carbon dioxide is highly compressed and is regulated to a desired pressure. It then travels through a 1.6 mm diameter flexible hose to the inlet of the collector device pictured in Figure 4.1 and as point 2 in Figure 4.6. The carbon dioxide rapidly expands through the diffuser and flows through the rectangular duct. Compressible calculations are conducted from the exit of the pressure regulator, point 1, to the exit of the diffuser, point 3. The results are then input into incompressible flow calculations to determine the velocity at the collection area. The calculations are done in an iterative process to satisfy all of the equations.

4.4.1 Compressible Flow

The flow is highly compressed at the beginning of the process, therefore compressible calculations must be utilized to fully capture the characteristics of the flow. A schematic of the first section analyzed is shown in Figure 4.6. The pressure at point 1 is known as the

regulation pressure while the temperature is calculated as an isentropic expansion from the pressure vessel with Equation 4.2.

$$\frac{T_1}{T_2} = \left(\frac{P_1}{P_2}\right)^{\frac{k-1}{k}} \tag{4.2}$$

Carbon dioxide ($k = 1.288$) is typically stored at 6205 kPa and 300 K. The pressure at point 3 is assumed slightly higher than atmospheric. This assumption is to account for the pressure drop that occurs through the rest of the duct and across the filter. The actual pressure drop will be calculated with the incompressible flow calculations. As a result, this process must be iterated so that the pressure at point 3 matches the calculated pressure at point 3 with incompressible equations. Due to the large pressure differential it is assumed that the flow will be choked at location 2; this assumption will be later confirmed. The section from location 1 to location 2 is analyzed with the Fanno flow calculations. Under Fanno flow, it is assumed that the potential energy effects are negligible and that the flow is adiabatic. The Mach number at the inlet can then be calculated as a function of the distance to the critical state, location 2,

$$\frac{f(l^* - l)}{D} = \frac{1}{k}\frac{(1 - Ma^2)}{Ma^2} + \frac{k+1}{2k} ln\left\{\frac{[(k+1)/2]\,Ma^2}{1 + [(k-1)/2]\,Ma^2}\right\} \tag{4.3}$$

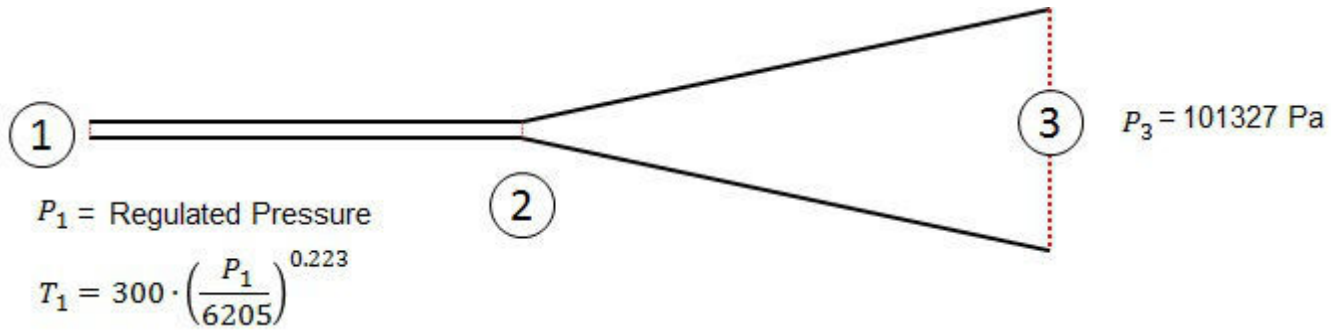

Figure 4.6: Schematic of the section of flow analyzed with compressible flow calculations.

The friction factor, f, is initially assumed as 0.02 and then iterated after determining the average velocity. The length differential, $l^* - l$, is 0.0762 m and the diameter of the tubing is D=1.6 mm;, therefore the Mach number at location 1 is calculated to be 0.574. The local speed of sound is calculated as,

$$c = \sqrt{kRT} \tag{4.4}$$

where R is the gas constant and T is the local temperature. Using the local speed of sound and the Mach number, the velocity at point 1 is found to be 155 m/s. The choked temperature T^*, pressure P^*, and velocity V^* can all be calculated knowing the inlet conditions,

$$\frac{T_1}{T^*} = \frac{(k+1)/2}{1 + [(k-1)/2]\, Ma_1^2} \tag{4.5}$$

$$\frac{P_1}{P^*} = \frac{1}{Ma_1} \left\{ \frac{(k+1)/2}{1 + [(k-1)/2]\, Ma_1^2} \right\}^{1/2} \tag{4.6}$$

$$\frac{V_1}{V^*} = \left\{ \frac{[(k+1)/2]\, Ma_1^2}{1 + [(k-1)/2]\, Ma_1^2} \right\}^{1/2} \tag{4.7}$$

where the lowest regulated pressure of 239.2 kPa will be used as the pressure at location 1. The results of Equations 4.5, 4.7, and 4.7 as well as the choked density as calculated using the ideal gas law are presented in Table 4.1. The average velocity is calculated between points 1 and 2 and the friction factor is checked; the friction factor is then iterated as needed. It should also be noted that the critical pressure is still much greater than the outlet pressure at location 3, and as a result the choked flow assumption at location 2 is confirmed.

Table 4.1: Choked flow conditions for P_1=239.2 kPa

T^*	116 K
P^*	120.5 kPa
V^*	168.3 m/s
ρ^*	5.48 kg/m^3

The flow is assumed isentropic from location 2 to location 3. To satisfy the first law for an ideal gas with constant specific heat the temperature at location 3 is defined as,

$$T_3 = T_0 - \frac{V_3^2}{2 \cdot c_p} \tag{4.8}$$

where T_0 is the stagnation temperature. Assuming that the flow is also steady and one dimensional the stagnation temperature is calculated using,

$$\frac{T}{T_0} = \frac{1}{1 + [(k-1)/2] Ma^2} \tag{4.9}$$

where the temperature T can be substituted with T^* when the Mach number is equal to one. Equation 4.9 then reduces to,

$$\frac{T^*}{T_0} = \frac{2}{k+1} \tag{4.10}$$

The velocity V_3 and temperature T_3 in Equation 4.8 are unknown and as a result an initial guess for the temperature is taken as slightly below the stagnation temperature. The velocity will be very low at location 3 due to the large area increase of the diffuser. The conservation of mass in conjunction with the idea gas law between points 2 and 3 is used to find the velocity at point 3 as,

$$V_3 = \frac{(\rho A V)_2}{\left(\frac{P_3}{RT_3}\right) A_3} \tag{4.11}$$

where the pressure P_3 and temperature T_3 are both initial guesses to be iterated. Once the velocity is known, Equation 4.8 is used to check the initial guessed temperature. The pressure at point 3 is found with the incompressible calculations.

4.4.2 Incompressible Flow Calculations

The remainder of the flow through the rectangular duct after the diffuser is calculated assuming that it is incompressible. This is a valid assumption as the velocities are very low and the gas has expanded to almost atmospheric conditions through the diffuser. A schematic for the incompressible calculations is presented in Figure 4.7. The pressure at point 3 was assumed from the compressible flow calculations to determine the velocity at point 3. Conservation of mass states that if the flow is steady and incompressible, the velocity at point 3 equals the velocity at point 4 because the duct has a constant area. Therefore, the energy equation reduces to,

$$\frac{p_3}{\gamma} = \frac{p_4}{\gamma} + h_{L\,3-4} \tag{4.12}$$

where γ is the specific weight and $h_{L\,3-4}$ represents the major and minor losses due to viscous effects. The major loss is calculated as,

$$h_{L\,major} = f\frac{L}{D}\frac{V^2}{2g} \tag{4.13}$$

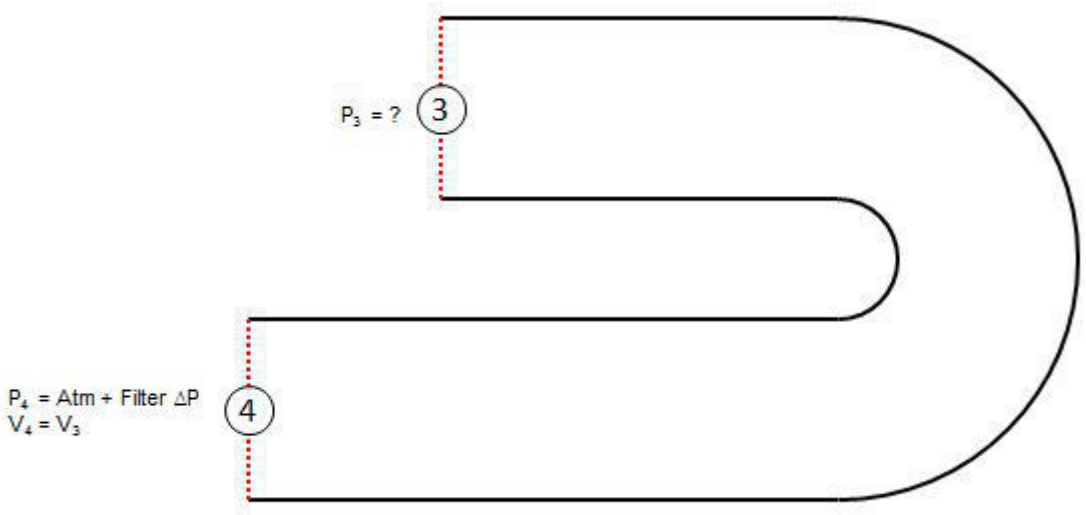

Figure 4.7: Schematic of the duct section analyzed with incompressible flow calculations.

where L is the length of the duct at the centerline and D is the hydraulic diameter of the duct. The friction factor is found using Colebrooks formula with an equivalent roughness of 0.0015 for drawn tubing and the Reynolds number. A minor loss also exists due to the 180^o bend and is defined as,

$$h_{L\,minor} = K_L \frac{V^2}{2g} \tag{4.14}$$

where K_L is a loss coefficient. The loss coefficient is found using a chart from Munson, Figure 8.30 [16], for bends knowing the radius, hydraulic diameter, and equivalent roughness. Finally, Equation 4.12 is used to calculated the pressure at location 3 where the pressure at 4 is found from Equation 4.1 knowing the velocity at point 4. The calculated pressure is then compared to the assumed pressure in the compressible flow calculations and is iterated as necessary.

The compressible and incompressible flow calculations were implemented in an excel spreadsheet, presented in Appendix A, to allow for quick iteration. The spreadsheet was used to examine the effects of the collector dimensions on the collection velocity. In particular the collector cross-sectional dimensions were analyzed as the diffuser angle and bend radius would be studied through CFD. The properties of the working fluid, carbon dioxide, and the particle bed, sand, as well as the duct sizing dictated the zone of operation from Figure 2.1. It was found that the system primarily operated in Zone I proposed by Kalman et al [13]. It was desired to operate the collector at a velocity approximately 20% above the calculated minimum pick up velocity to insure entrainment and transport of the sand. As the cross sectional area of the duct increased, the flow rate decreased and as a result a larger inlet pressure was required to achieve the desired collection velocity. Also, maintaining the collection velocity in a larger duct resulted in larger flow rates through the system and ultimately depleting the source at a faster rate. The required inlet pressure and the amount of flow time, if utilizing a 16 g carbon dioxide cartridge, were both examined while varying

the cross-section dimensions. It was found that the cross sectional sizing was the dominant factor in determining the collection velocity as the viscous resistance and bend losses had minimal effects in comparison. The size was chosen to allow for the desired collection velocity to be achieved at an inlet pressure of approximately 1135 kPa and allow for a flow time of at least 2 seconds. An inlet pressure of 1135 kPa was within the pressure range of most pressure regulators commercially available. Utilizing the spreadsheet, the duct height and width were set as 19.1 mm and 25.4 mm respectively to allow for a large collection opening while not sacrificing the flow time of the system or the amount of inlet pressure required.

4.5 FLUENT Analysis

Simulations of the rectangular duct collector were performed with FLUENT to study the effects of two main parameters: diffuser angle and the bend radius. Whenever geometry changes occur a new mesh needs to be created which can occupy a lot of time. To efficiently study the effects of multiple parameters, a Matlab script file was written to generate key geometry points and ICEM script files were recorded to generate the mesh. The mesh generation procedure is documented in Appendix B.

The mesh generated with ANSYS ICEM was imported into FLUENT where compressible turbulence models were implemented to simulate the flow through the rectangular duct. The inlet pressure was set to 791 kPa as discussed in section 4.4.2 and the filter was represented by a porous media. The inertial and viscous coefficients of the porous media were calculated from the coefficients of the pressure drop versus velocity curve found in section 4.3. The outlet of the filter was set as a vent outlet of zero gauge pressure. These boundary conditions remained constant throughout all of the FLUENT simulations to strictly compare the effects of the geometry changes. The diffuser was first analyzed in an effort to eliminate

separation and recirculation while considering the size constraints. Once a diffuser angle had been decided the effects of the bend radius on the velocity profile at the collection area were analyzed. The bend was modified and iterated in an effort to achieve a fully developed turbulent velocity profile at the collection area.

4.5.1 Diffuser Angle

The diffuser angle was studied first as it dictated the allowable dimensions of the other parameters of the collector. It was desired to find a diffuser angle that would decelerate and expand the flow efficiently. An array of simulations was completed with varying diffuser angles while holding all other dimensions constant. The boundary conditions, initial conditions, and the grid resolution remained constant for all simulations. The diffuser angle was varied from 4 degrees up to 10 degrees and the velocity profiles were examined in each case. A large diffuser angle caused separation of the flow and as a result recirculation. On the contrary, a small diffuser angle created a very long diffuser which induced more viscous resistance and limited the variability of the other collector parameters. Contours of the x-velocity magnitude for varying diffuser angles are shown in Figure 4.8 where the white space represents negative velocities. The area of recirculation and/or separation represented by the white space in Figure 4.8 clearly increases as the diffuser angle increases. To better visualize this, contour plots of the velocity magnitude on planes perpendicular to the flow are shown in Figure 4.9 for the same diffuser angles. Examining the contour plots of the diffuser angles larger than 5 degrees shows that the flow completely separates from the walls of the diffuser. Separation occuring at a diffuser angle of 6 degrees is contrary to the commonly known performance of conical diffusers. However, due to the pyramidal shaped diffuser, separation occurs in the corners first and begins flow separation at a lower diffuser angle. As a result, large recirculation zones developed, which are a waste of valuable energy. The differences

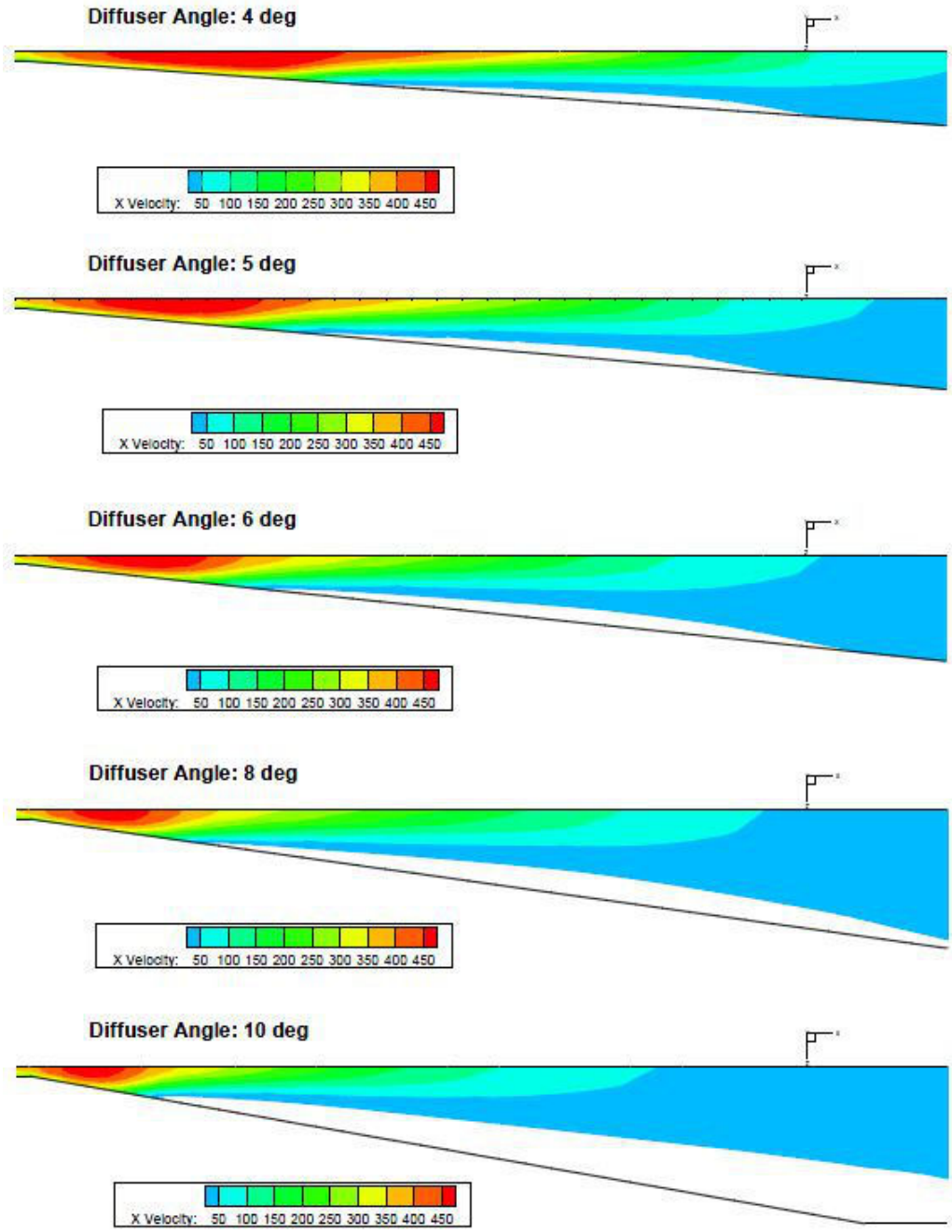

Figure 4.8: Diffuser angle comparisons showing contours of velocity; white area represents areas of recirculation.

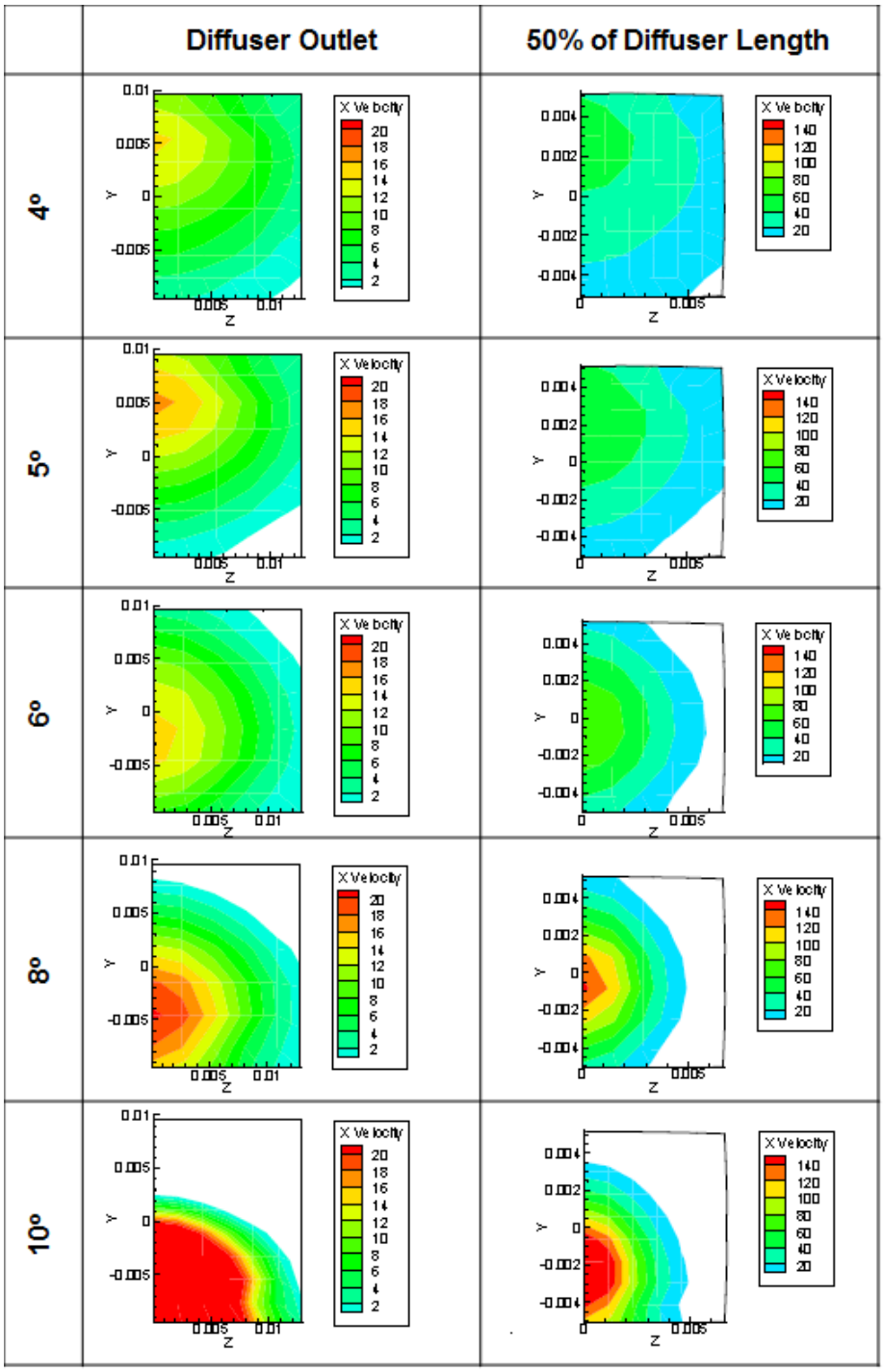

Figure 4.9: Contours of velocity magnitude at two cross sections for varying diffuser angles.

between a 5 degree and a 4 degree diffuser angle are minimal and only slight separation exists in the corner of the duct. The 4 degree diffuser angle produces a 25% increase in length over the 5 degree angle with only minimal gains; the 5 degree angle was chosen for the collector as the best compromise of size and performance.

4.5.2 Bend Radius

After diffusing the flow it must achieve the desired fully developed velocity profile at the collection area. Due to the dimension constraints, a bend was added to allow for additional length for the flow to develop. Therefore, the bend radius was studied to find the best compromise between size of the bend and the velocity distribution resulting from the bend. Once again the study was performed in FLUENT with the same models as used in the diffuser angle study. All boundary conditions, initial conditions, mesh resolution and the diffuser angle remained constant. However, the upper and lower length were varied dependent on the bend radius to meet the maximum size constraint of 0.254 m. This was done to achieve the greatest length possible to allow the flow to develop fully. In all of the studies conducted the velocity profile was measured on the centerline of the duct at the beginning of the collection area. The collection area location was held constant at 0.1 m from the outlet of the collector.

The first study was conducted by solely varying the bend radius and it was found that it had little effect on the simulated velocity profiles as shown in Figure 4.10. The position ranged from the top of the duct to the bottom on the center line. It was noticed that the length of the straight after the diffuser was not long enough to dissipate the effects of the jet flow in all cases. As a result of the Coanda effect through the diffuser, the flow was not symmetric at the exit of the diffuser. In all cases, higher velocities occurred on the top wall and ultimately along the outer radius of the bend, which caused the skewed velocity profiles

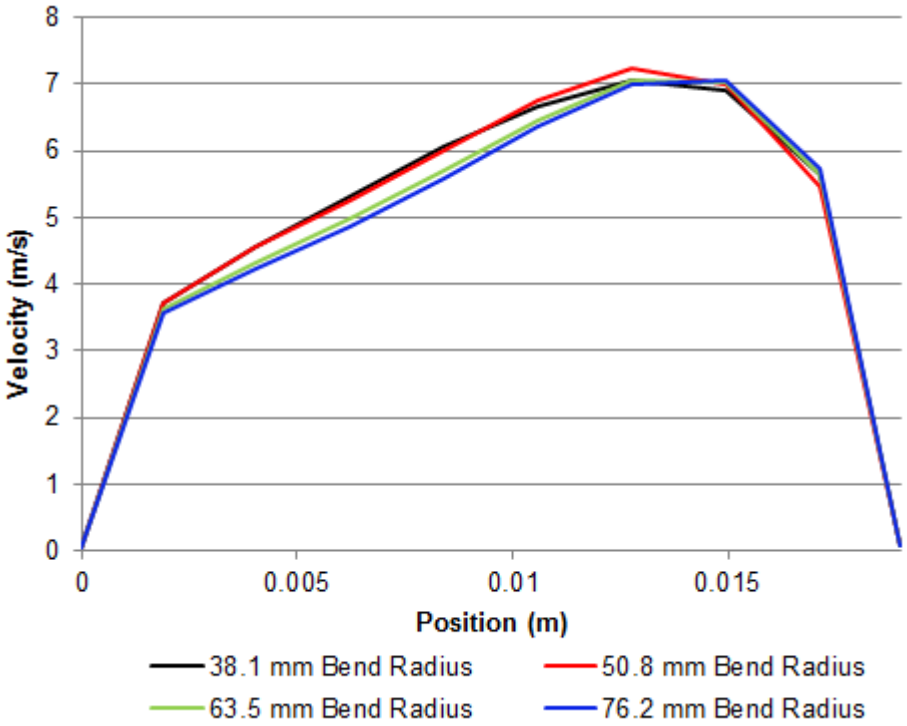

Figure 4.10: Velocity profiles simulated while varying the bend radius.

seen in Figure 4.10. The Coanda effect caused the jet flow to be attracted and attached to the upper wall of the collector just after the diffuser due to the bend in the rectangular duct. The residual effects of the velocity distribution at the exit of the diffuser was dominant over the effects of the bend radius.

Due to the findings of the first study a guide vane was added to the bend to aid in better distributing the flow. The guide vane was centered in the duct dividing it into two equal parts. The same bend radii were studied and an improvement in the velocity profiles were found, as seen in Figure 4.11. The residual effects of the diffuser are still apparent, but were reduced by the addition of the guide vane. The results appear to be contrary to common knowledge in that the larger bend radius produced a more skewed velocity profile. However, this is due to the decrease in straight length after the diffuser to compensate for the

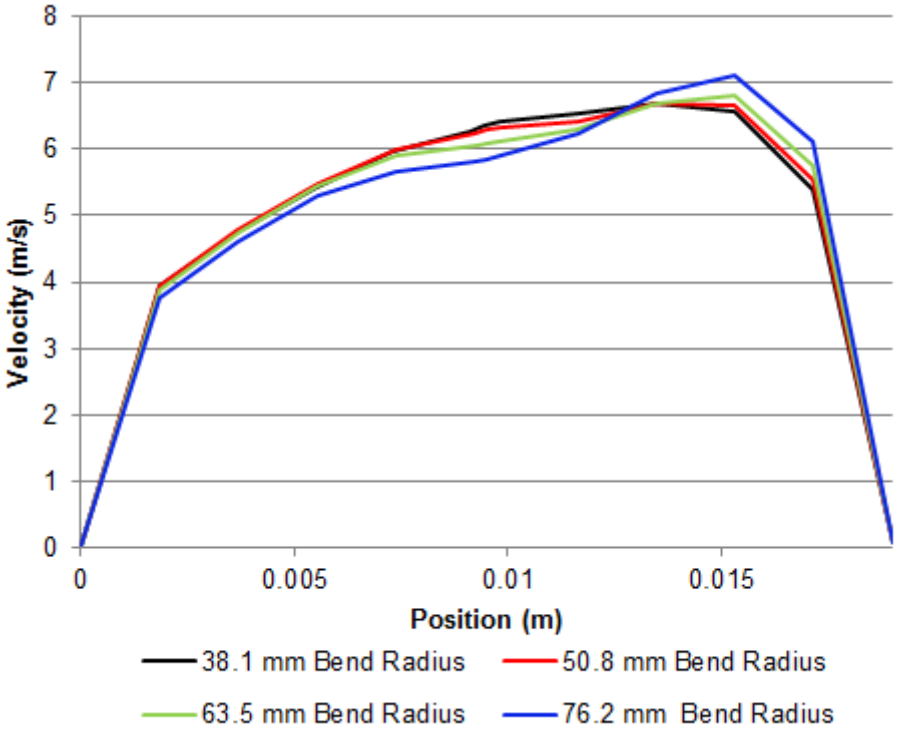

Figure 4.11: Simulated velocity profiles with the addition of a centered guide vane.

larger bend radius. The flow has less length to dissipate the jet flow effects and it protrudes further into the bend. This produces higher velocities on the outer wall of the bend and a skewed velocity profile. The addition of a guide vane did ultimately improve the results, but did not meet the requirement of a fully developed velocity profile.

The guide vane was offset from the center of the bend radius in an attempt to further improve the distribution of the velocities at the collection area. The simulations were all performed in a bend radius of 50.8 mm and the results are shown in Figure 4.12. Slight improvements were noted with the 0.508 mm and 1.27 mm offsets, but the velocity profiles were still skewed to the bottom side of the duct. When the offset was increased to 2.54 mm a significant improvement in the distribution of velocities was seen. It was noted that by introducing a larger area on the inner radius of the bend, the jet flow characteristics of the

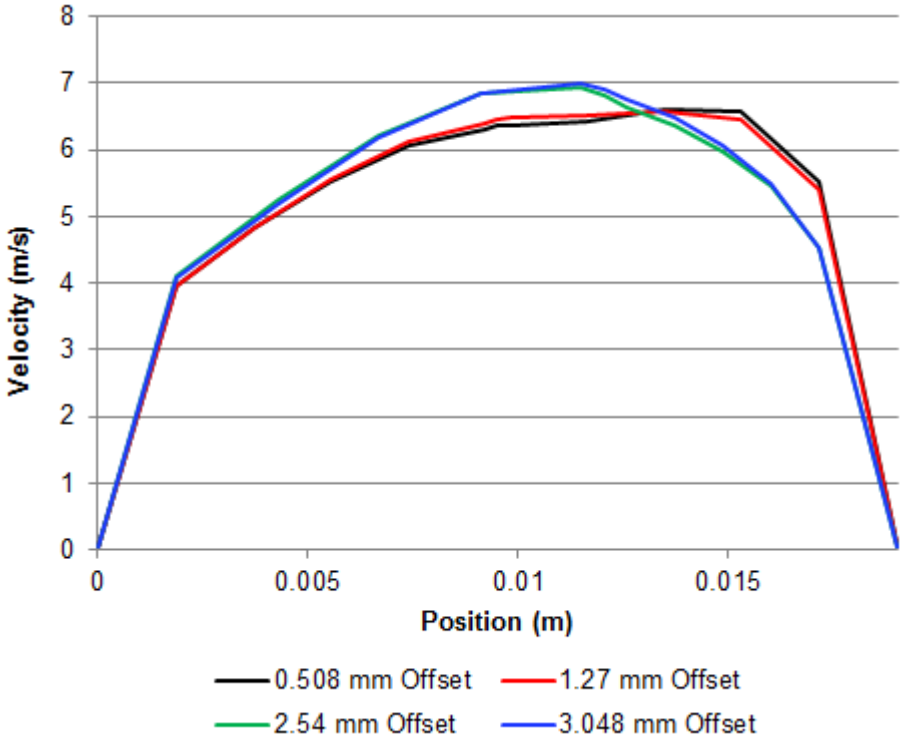

Figure 4.12: Simulated velocity profiles while varying the position of the guide vane in a 2" bend radius.

diffuser were coerced towards the bottom wall of the duct. This produced higher velocities on the inner radius purely due to the residual effects of the jet flow. The flow through the outer area of the bend radius was also higher due to the smaller cross sectional area. Ultimately, the 2.54 mm offset guide vane produced a more symmetric velocity distribution at the collection area. Further increasing the offset to 3.048 mm began showing negative effects on the velocity distribution.

Finally, the 2.54 mm offset guide vane was applied to varying bend radii. The goal was to find a combination of guide vane placement and bend radius that would most closely match a fully developed turbulent velocity profile. The results of the simulations performed with a 2.54 mm offset guide vane in varying bend radii is show in Figure 4.13. The fully developed velocity profile was simulated in a straight rectangular duct of the same dimensions as the

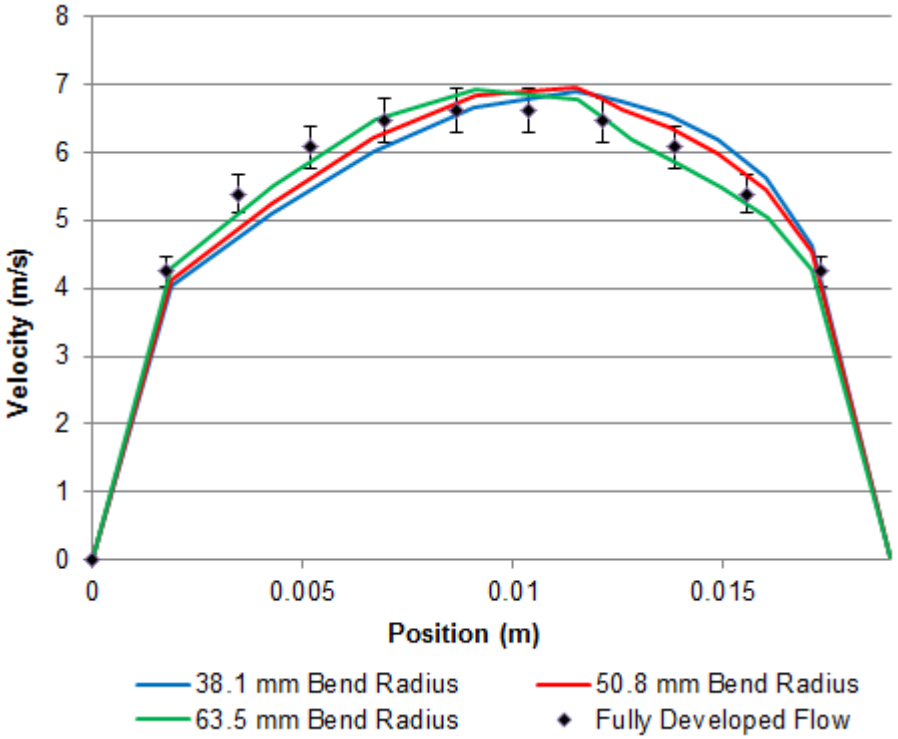

Figure 4.13: Simulated velocity profiles with a 2.54 mm offset guide vane in varying bend radii.

collector and the error bars represent +/- 5%. It was found that a bend radius of 63.5 mm with a 2.54 mm offset guide vane produced a velocity profile at the collection area that was within 5% of the simulated fully developed velocity profile.

The completion of the bend radius studies concluded the design of the collector. In summary, the carbon dioxide enters the collector through a 1.6 mm diameter orifice and expands through a 5 degree diffuser into a rectangular duct that is 19.1 mm in height and 25.4 mm in width. After the diffuser there is a 0.043 m straight section before entering a 180 degree bend with a radius of 63.5 mm. The bend contains a guide vane that runs the full length of the bend and is offset 2.54 mm from the centerline towards the outside of the bend. After the bend the carbon dioxide flows through a 0.1778 m straight section before exiting the system through a 100 μm filter. A dimensioned drawing of the final collector design is pictured in Appendix C. The combination of the diffuser and bend radius studies produced a collector design that resulted in a velocity profile at the collection area that was within 5% of a fully developed velocity profile while meeting the overall size constraints.

4.5.3 Final Design Multiphase Flow

The collector design simulations in the previous sections have utilized single phase compressible turbulence flow models. However, to simulate the particulate entrainment process a multiphase model was required which cannot be used in conjunction with a compressible flow model. To overcome this, a profile of the flow containing the velocity, pressure, and turbulence information was exported from the compressible case and imported as the inlet condition to a multiphase case. The profile was taken just after the bend radius, therefore the geometry for the multiphase flow only included the lower straight section as pictured in Figure 4.14. The multiphase flow parameters were set the same as those found through-

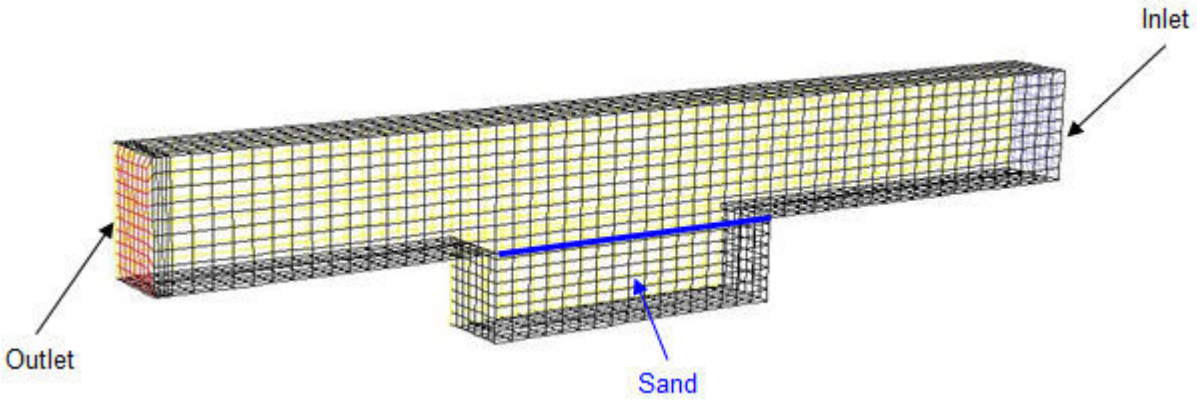

Figure 4.14: Mesh used for multiphase flow simulations of final collector design.

out the 2D study presented in Section 3.2.1. The simulations showed the top layer of the sand (blue) being entrained into the flow and carried into the storage area illustrated in Figure 4.15.The system operated purely on particulate entrainment and only the top layer of particles was collected. The results from the simulations were validated with experimental testing.

4.6 Experimental Testing and Results

The final design of the collector was manufactured utilizing the additive manufacturing process for testing. The first round of tests was performed with compressed air due to its availability to confirm the FLUENT simulation models and results. A pitot-static tube was fitted in place of the collection area and the velocity profile was measured over a range of inlet pressures. The system was then supplied with carbon dioxide and the velocities at the collection area were measured at two inlet pressures. Finally, the system was placed on a bed of sand to test for particulate entrainment.

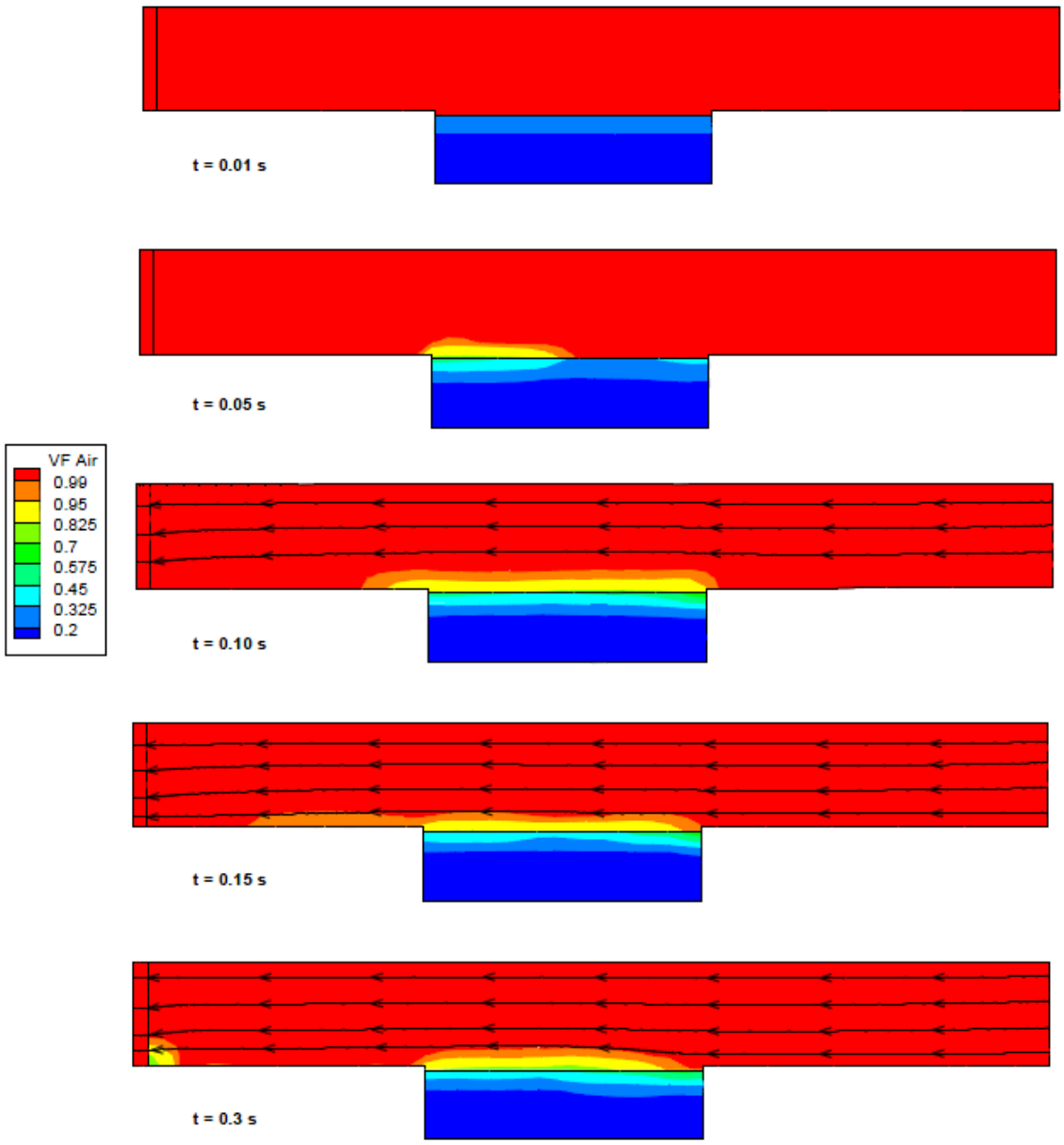

Figure 4.15: Multiphase simulation of final collector design. Velocity streamlines of the gas flow are shown in black.

4.6.1 Velocity Profile Measurement

In an effort to validate the results found through FLUENT simulations as well as the values from the fluids calculations in Section 4.4, the collection device was fitted with a pitot-static tube in place of the collection area. The complete experimental setup is pictured in Figure 4.16. A 70 gallon air compressor was used as the supply to the system which was connected to a pressure regulator. A pressure transducer was connected to the pressure regulator to measure the supply pressure during the experiment. A ball valve was employed after the pressure regulator to control the air supply through the system. The collection device was then fitted with an aluminum plate fitted with a pitot-static tube at the collection area as shown in Figure 4.17. An Omega differential pressure transmitter, part number PX275-01DI, was used in conjunction with the pitot-static tube. The voltage output of the pressure transmitter was input to a National Instruments myDAQ unit connected to a laptop running

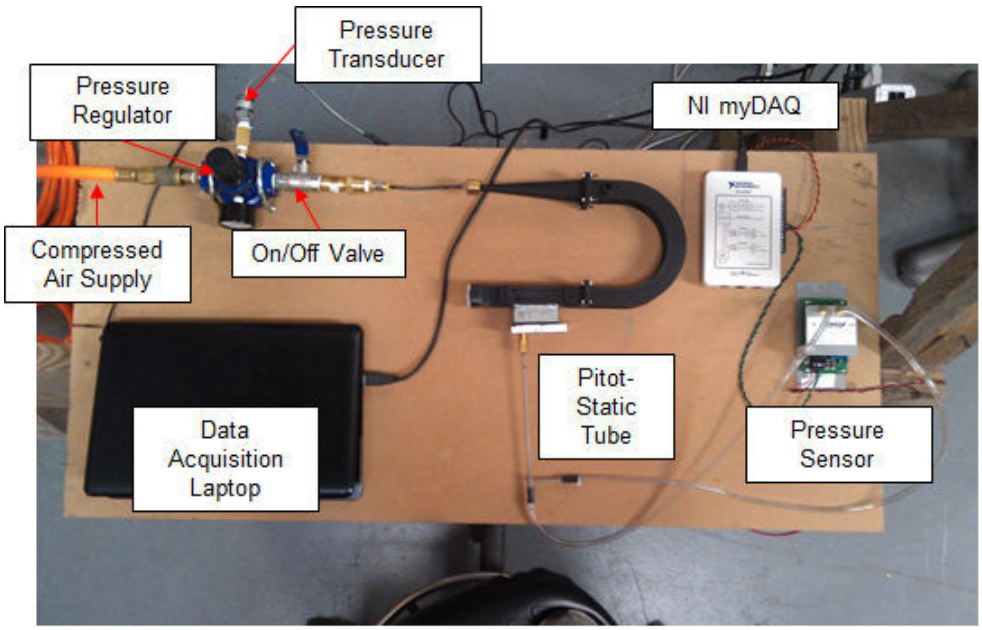

Figure 4.16: Experimental setup for measured the velocity profiles at the collection area.

Labview for data collection. The pressure transducer and pitot-static tube data was sampled at 100 Hz for 5 seconds and the average and standard deviation of the data was recorded.

The velocity profile was measured for five inlet pressures utilizing compressed air and two inlet pressures with carbon dioxide. At each inlet pressure the height of the pitot-static tube was varied from 0.0047 m to 0.014 m in two equal increments as measured from the bottom side of the duct as shown in Figure 4.17. Each case was also simulated with FLUENT for comparison with the measured data.

The first experiments were run with compressed air due to the availability. The simulations accurately predicted the measured velocity points as illustrated by the dashed lines in Figure 4.18. The centerline velocities matched within 2% in every case except for the 419 kPa inlet case in which only an 8% difference was observed. The other two measured points agreed well with the simulations at the three lower inlet pressures, but were higher for an inlet pressure above 480 kPa. However, the maximum percentage difference at any point was less than 20%. Also, the velocity profile appeared to be symmetric through the measurements as was predicted with simulations. The measured data was also compared to the average velocity as calculated by the fluids calculations as summarized in Table 4.2. The

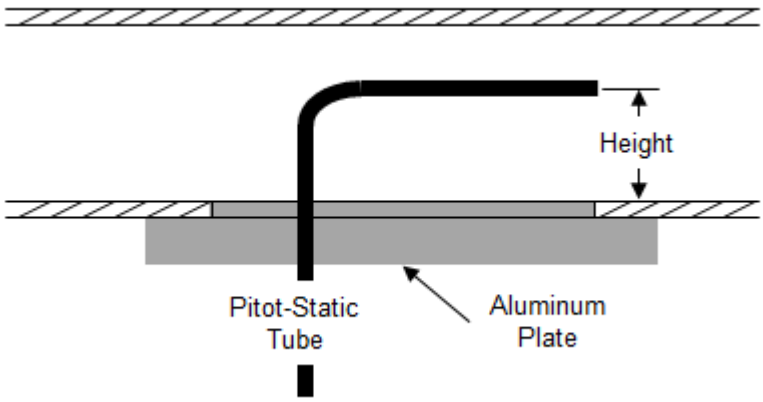

Figure 4.17: Pitot-Static tube installed in the collection area.

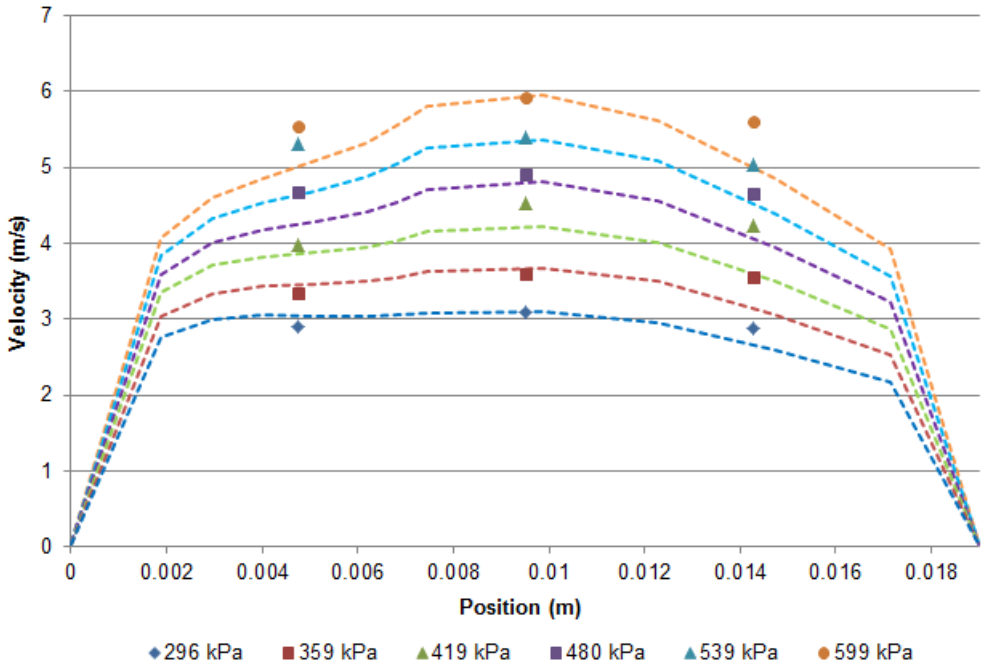

Figure 4.18: Measured velocity versus simulated velocity profiles, dashed lines, when using compressed air.

Table 4.2: Compressed Air Measured, Simulated, and Calculated Collection Velocities

Inlet Pressure (kPa)	Measured Velocity	Simulated Average Velocity	Calculated Average Velocity	% Difference: Measured and Simulated	% Difference: Measured and Calculated
296	2.2	2.57	2.38	14	8
359	2.6	2.98	2.74	14	5
419	3.2	3.38	3.08	6	4
480	3.55	3.78	3.43	6	3
539	3.93	4.2	3.78	6	4
599	4.27	4.57	4.11	6	4

combined results of the compressible and incompressible calculations performed in Section 4.4 correlated very well with the measured data. The average velocity at the collection area was predicted within 10% in each case when compared to the measured data.

The test was then repeated using carbon dioxide as the supply to the collection device. The experimental setup was very similar to the one pictured in Figure 4.16, but the supply was replaced with a carbon dioxide tank. The velocities were tested at two inlet pressures: 691 kPa and 827 kPa. The cases were also simulated in FLUENT and good correlation with the measured data was observed as illustrated in Figure 4.19. Similar to the results from the compressed air tests, the center line velocities were simulated within 3% of the measured and the other two points were within 12% of the measured velocities. The measured velocity points were also compared to the fluids calculations as shown in Table 4.3. The fluids calculations correlated extremely well with the measured data with a maximum of a 3% difference. As demonstrated by the compressed air and the carbon dioxide tests, the

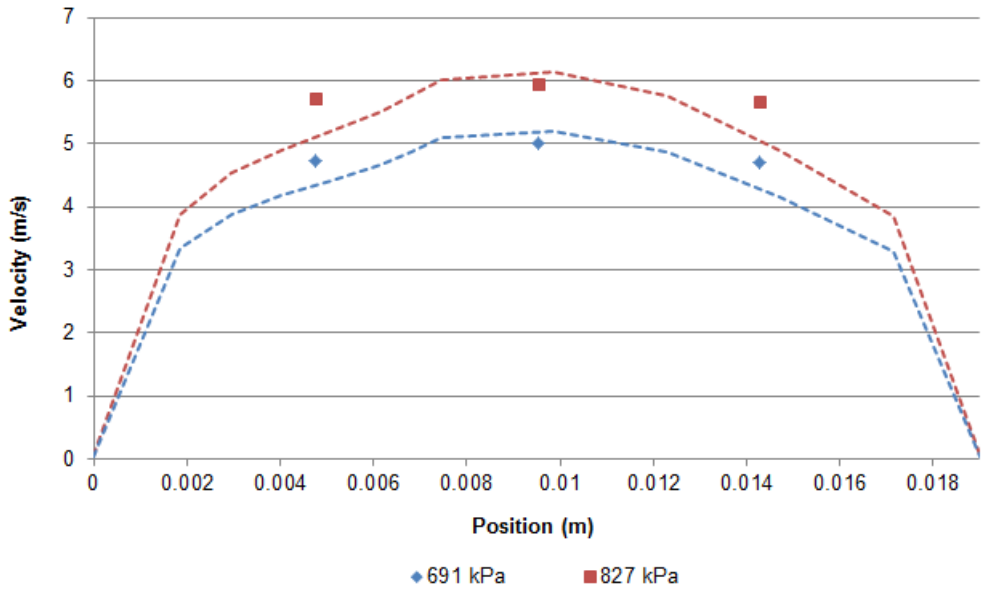

Figure 4.19: Measured velocity points versus simulated velocity profiles shown as the dashed lines when using carbon dioxide.

Table 4.3: Carbon Dioxide Measured, Simulated, and Calculated Collection Velocities

Inlet Pressure (kPa)	Average Measured Velocity	Simulated Average Velocity (m/s)	Calculated Average Velocity (m/s)	% Difference: Measured and Simulated	% Difference: Measured and Calculated
691	3.62	3.94	3.55	8	2
827	4.33	4.63	4.21	6.5	3

FLUENT simulations and the fluids calculations proved to be a valuable tool to predict the velocities and velocity distribution at the collection area.

4.6.2 Particle Entrainment Testing

After verifying the simulated and calculated velocity results, the collection device was tested on a bed of sand. The experiment was only performed with carbon dioxide as the supply due to the increased density, and as a result a lower required pick up velocity. The lower density of compressed air requires a higher pick up velocity as found by Equations 2.5 and 2.6. At the highest inlet pressure tested with compressed air, the required minimum pick up velocity was calculated as 6.25 m/s. This scenario was tested and as predicted, no particulate entrainment was observed.

The experimental setup with carbon dioxide as the supply is shown in Figure 4.20. A 50 lb carbon dioxide tank was used as the supply and was fitted with a pressure regulator. The output of the pressure regulator was connected to a ball valve to control the flow through the collector. Lastly, the collector was placed on a bed of sand that had been sieved to 500 μm. A viewing window of the collection area was implemented to visualize the entrainment process shown in Figure 4.21. To begin testing the ball valve was opened and the carbon dioxide flowed through the collector. The test was performed with the same two inlet pressures as measured in section 4.6.1.

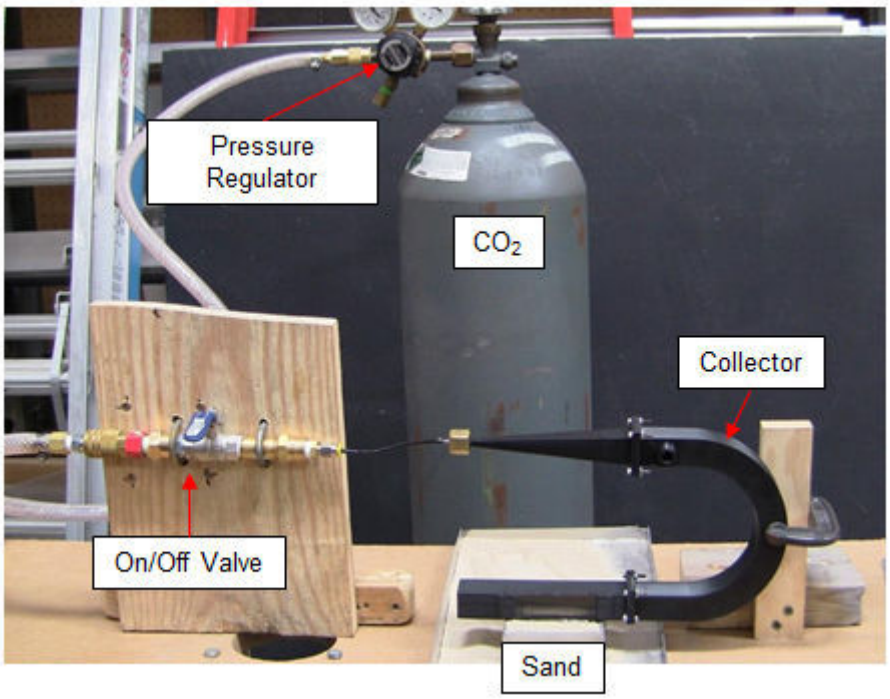

Figure 4.20: Experimental setup for particulate entrainment testing with carbon dioxide as the supply.

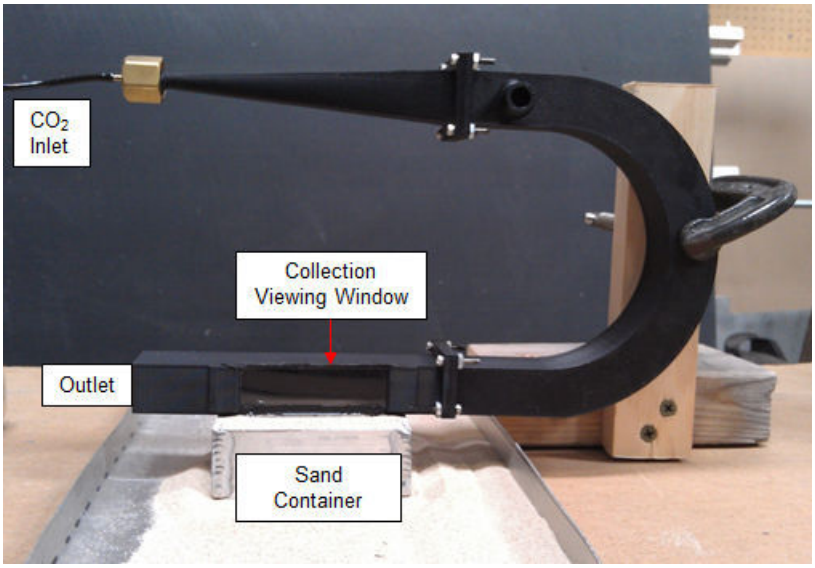

Figure 4.21: Collector device placed on a bed of sand with a viewing window to visualize the particulate entrainment process.

Table 4.4: Carbon dioxide measured collection velocity versus minim pickup velocity

Inlet Pressure (kPa)	Average Measured Velocity (m/s)	Minimum Pick up Velocity (m/s)
691	3.62	3.45
827	4.33	3.5

The minimum collection velocity was calculated for each inlet pressure and compared to the measured average velocity as shown in Table 4.4. At the lower pressure of 691 kPa, the measured average collection velocity is only 5% above the minimum pick up velocity. As explained in the literature review, this is truly a minimum velocity in which particulate entrainment or saltation will begin. The higher inlet pressure of 827 kPa produced an average measured velocity that was approximately 20% higher than the minimum pick up velocity and as a result considerably more particles should be entrained in the flow.

The test was first conducted at an inlet pressure of 691 kPa and as expected particulate entrainment was observed, however it was sparse. The entrainment process was recorded through the viewing window and three frame captures are shown in Figure 4.22. Unfortunately, due to the frame rate and the rate of movement of the particulate it was hard to capture the motion in still frames; the particle paths have been highlighted with red arrows in the frame captures. The first frame is just before the test was started and the particulate is at rest. In the second frame, particles on the top layer of the sand have begun the saltation process and are entrained into the flow. In frame three, the flow has developed and particles are being entrained at a constant rate, yet sparse, as previously mentioned. The observed motion was exactly as expected due to only supplying a velocity 5% above the calculated minimum pick up velocity.

The inlet pressure was then increased to 827 kPa which resulted in a collection velocity 20% higher than the minimum pick up velocity. This inlet pressure matched the boundary

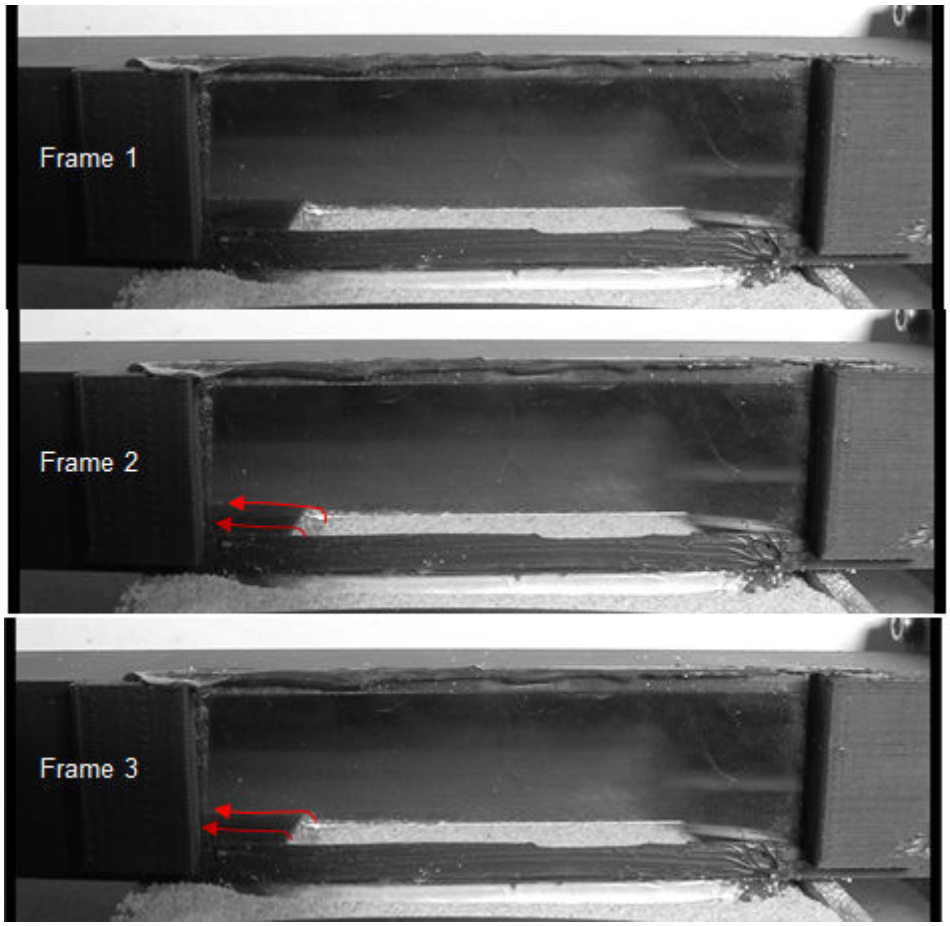

Figure 4.22: The particulate entrainment process at an inlet pressure of 691 kPa.

conditions of the simulated multiphase case presented in Section 4.5.3. The test was also recorded and three frame captures are shown in Figure 4.23. Frame one represents the particulate before the flow has begun. In the second frame, the red highlighted area shows particulate being entrained into the flow. The red highlighted area in frame three shows a much denser grouping of particulate as it flows into the storage area. Once again, the dynamics were difficult to capture on film, but a significant amount of particles were entrained at the higher inlet pressure. The entrainment process seen through the experimental testing matched very well with the final multiphase simulation. As predicted through simulation, only the top layer of the sand was entrained into the flow and carried to the storage area.

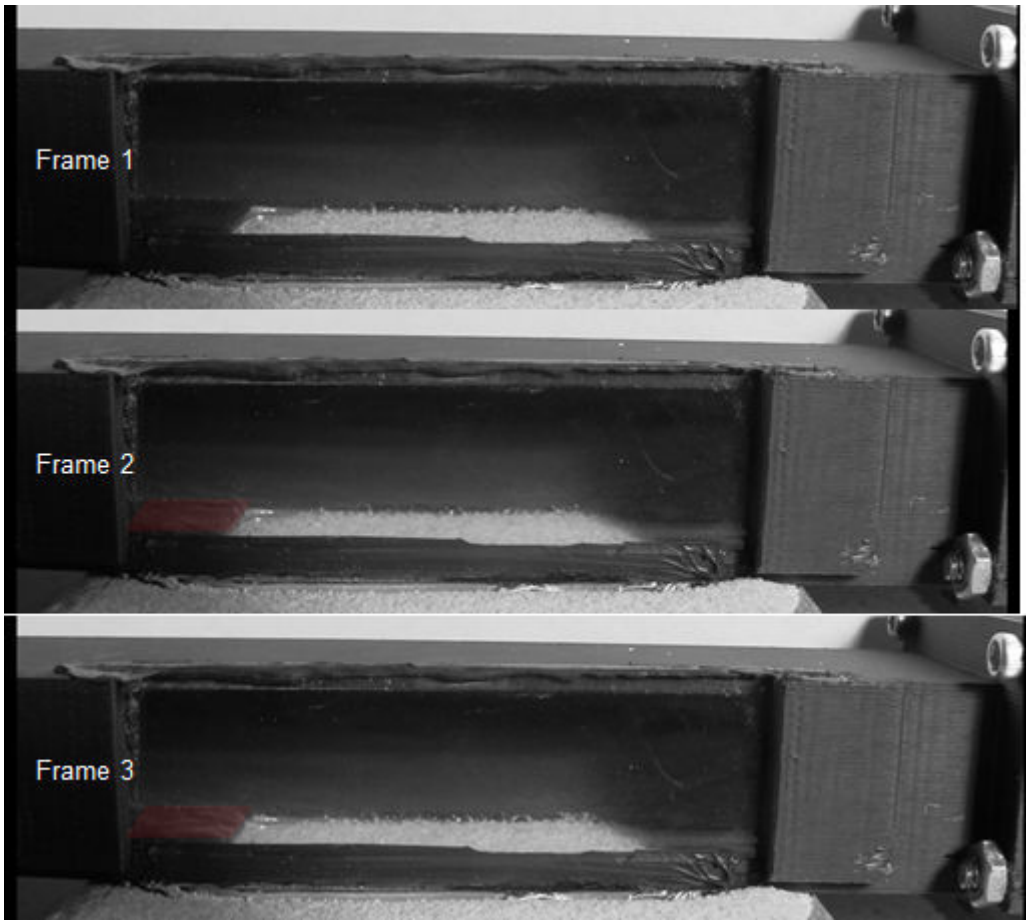

Figure 4.23: The particulate entrainment process at an inlet pressure of 827 kPa.

These experimental results validated the multiphase simulation.

The collection device designed through fluids calculations and FLUENT provided a system capable of of employing the mechanism of particulate entrainment as a method of transport. The aforementioned process collected only the top layer of particles as desired. Areas of recirculation and jet impingement on the particulate bed were completely eliminated in the design of a more efficient collection device.

Chapter 5.

Conclusions and Recommendations

5.1 Conclusions

The pneumatic particulate collection system was originally conceived by Mike Couch [8] from the USL to be implemented in place of a vacuum sampler system. The pneumatic PCS overcomes the issues of the shear size and power draw of a vacuum system while still maintaining the performance desired. The original design was developed based solely on experimental testing and results; therefore it was desired to further analyze the system through high speed video and computational fluid dynamics to improve the design. The high speed video in conjunction with the CFD analysis highlighted areas of recirculation in the collector resulting in wasted energy. It was also noted that the jet flow was impacting the particle bed, as opposed to operating on an entrainment principle as desired. An effort to improve the design deficiencies combined with the knowledge gained through the literature review served as the basis of the improved PCS.

The original PCS utilized a compressed air tank as the supply to the collection system which created an unsteady system. As the compressed air tank was depleted the density of the air changed and consequently the minimum pick up velocity of the particulate was

constantly changing. This produced a system that was very difficult to design and operate at peak performance throughout the entire collection process. As a result, the improved collection system utilized carbon dioxide as the transport gas. Carbon dioxide not only provided the benefit of being more dense, but can also be stored at much higher pressures as a saturated liquid. This storage technique creates a system that holds a constant pressure until all of the saturated liquid has been evaporated and the collector can operate at a semi-steady state.

The improved PCS featured a rectangular duct design meant to expand and develop the carbon dioxide gas flow prior to particulate collection. The system was analyzed through compressible and incompressible flow calculations to study the effects of geometry changes and operating conditions. It was found that a cross sectional size of 19.1 mm in height and 25.4 mm in width allowed for the desired collection velocity to be achieved without exceeding the allowable inlet pressure. The collector device was then thoroughly studied utilizing ANSYS FLUENT to determine the effects of the diffuser angle and the bend radius. The diffuser angle was varied from 4 deg up to 10 deg in an effort to reduce flow separation and recirculation while considering the overall size constraints on the system. A 5 degree diffuser angle was selected as the best compromise between flow performance and physical dimensions. The bend radius was then studied in a similar manner to optimize the velocity distribution at the collection area. A fully developed turbulent velocity profile was desired for collection to replicate the experimental studies researched in the literature review. Due to the short straight length after the diffuser, the residual jet flow effects through the diffuser dominated any effects introduced by the bend radius. Therefore, a guide vane was implemented through the center of the bend radius and eventually offset towards the outside of the bend to improve the flow distribution. It was found that a 63.5 mm bend radius with a guide vane offset 2.54 mm from the center line produced a velocity profile at the collection

area within 5% of a simulated fully developed velocity profile.

The final design of the collection device was manufactured with an additive manufacturing process to be bench tested. Initially, a pitot-static tube was installed in place of the collection area to validate the velocities and flow distribution predicted through calculation as well as CFD. It was found that both methods were able to accurately predict the flow characteristics through the collection device and served as a valuable tool in design. The collector was then placed on a bed of sand to test the particle entrainment capabilities. The first test was conducted at approximately the predicted minimum pick up velocity to verify the equations found through the literature review. Particle saltation and the beginnings of entrainment were observed at only 5% above the minimum pick up velocity as was expected. The inlet pressure was then increased to produce a velocity 20% above the minimum pick up velocity and a much greater amount of particulate was entrained. In both cases only the top layer of particles were affected, as was designed for.

Overall, the improved collection device eliminated any areas of recirculation and impingement on the particle bed while meeting the size constraints set forth. The system performed as designed and exhibited particle entrainment as the primary transport process. The compressible and incompressible flow calculations as well as the FLUENT simulations proved to be a valuable tool throughout the design process.

5.2 Recommendations for Future Work

The improved PCS performed as designed and as a result validated the use of FLUENT as a simulation and prediction tool. The flow through the system was accurately simulated and predicted, therefore could be used for further studies on the design. The cross sectional sizing was set through a basic study utilzing the fluids calculations spreadsheet in Appendix

A, however the effects of duct size changes on the flow were not studied. If the height of the rectangular duct could be further decreased without affecting the performance; the flow rate would increase and consequently would lead to a decrease in the inlet pressure required. Reducing the required inlet pressure would extend the amount of collection time available in the supply source. Also, the length of the collection area cut out was not studied through the simulations. It was set as a constant length and remained unchanged through all simulations. Varying this length could result in a larger area for collection and possibly an increase in particulate entrainment. Finally, the bend radius and guide vane could benefit from further simulation studies. It may be possible to decrease the bend radius and achieve the desired velocity profile with the use of multiple guide vanes or a flow straightening device after the diffuser. All of these changes could be studied with the models utilized in FLUENT.

The improved PCS was produced for testing utilizing the additive manufacturing process; although this process is relatively quick and easy, it does not produce a smooth surface finish. The major viscous losses through the collection system could be reduced by manufacturing the system in a different manner. A reduction in the major viscous losses would once again reduce the required inlet pressure.

The use of carbon dioxide created a system that operated at a lower collection velocity as opposed to compressed air. However, the pressure regulation and storage system was not designed in this thesis and is a critical subsystem of the overall collection process. Pressure regulation of a carbon dioxide source while maintaining the flow rate required by the collection device is a difficult task. The pressure regulator needs to be compact and lightweight to meet the needs of the proposed system. A device of this type is not readily available and would require extensive research and design. However, the benefits of utilizing carbon dioxide are prominent and worth the time to find a pressure regulation system.

As mentioned previously, a pressure regulation system is not readily available for a

carbon dioxide source. Carbon dioxide was initially chosen due to the wide availabiltiy of gas cartridges in a range of sizes. However, other gases do exist that have a higher density than compressed air and may be more easily regulated. Gas sources such as argon, propane, and butane all exhibit a relatively high density. All of the aformentioned gases would maintain the benefits of carbon dioxide and may be more easily regulated to the desired inlet pressure.

The design and analysis of the improved pneumatic particulate collection system not only eliminated areas of recirculation and operated purely on particle entrainment, but also provided valuable tools through calculations and CFD to further improve the design. The fluids calculations and CFD simulations were validated through the experimental testing and provide valuable tools that could be easily applied to variations of the collector design.

Bibliography

[1] Alhajraf, S. "Computational Fluid Dynamic Modeling of Drifting Particles at Porous Fences." Environmental Modeling & Software 19.2 (2004): 163-70. Print.

[2] ANSYS, Inc., 2010, ANSYS FLUENT 13.0 Theory Guide.

[3] Battaglia, F., England, J., Kanholy, S., and Deza, M., "On the Modeling of Gas-solid Fluidization: Which Physics are Most Important to Capture?", In Proceedings of the 2010 ASME International Mechanical Engineering Congress and Exposition. Paper IMECE2010-40213.

[4] Brunone, Bruno, Bryan W. Karney, Michele Mecarelli, and Marco Ferrante. "Velocity Profiles and Unsteady Pipe Friction in Transient Flow." Journal of Water Resources Planning and Management 126.4 (2000): 236. Print.

[5] Cimbala, John M. "Experimental Design." Lecture. Penn State University, 2009.

[6] C.K.K. Lun, S.B. Savage, D.J. Jeffrey, and N. Chepurniy. "Kinetic Theories for Granular Flow: Inelastic Particles in Couette Flow and Slightly Inelastic Particles in a General Flow Field". J. Fluid Mech. 140. 223-256. 1984.

[7] Cabrejos, Francisco J., and George E. Klinzing. "Pickup and Saltation Mechanisms of Solid Particles in Horizontal Pneumatic Transport." Powder Technology 79 (1994): 173-86. Print.

[8] Couch, Michael R. Pneumatic Particulate Collection System for an Unmanned Ground Sampling Robot. Thesis. Virginia Polytechnic Institute and State University, 2010.

[9] D. Gidaspow, R. Bezburuah, and J. Ding. "Hydrodynamics of Circulating Fluidized Beds, Kinetic Theory Approach". In Fluidization VII, Proceedings of the 7th Engineering Foundation Conference on Fluidization. 75-82. 1992.

[10] Den Toonder, J.M.J., and F.T.M. Nieuwstadt. "Reynolds Number Effects in a Turbulent Pipe Flow for Low to Moderate Re." American Institute of Physics 9.11 (1997): 3398-409. Print.

[11] Gel, Aytekin, Tingwen Li, Chris Guenther, and Sreekanth Pannala. "High Resolution Numerical Simulations of Coal Gasifiers Using High Performance Computing." Lecture. NETL Multiphase Flow Science Workshop. PA, Coraopolis. 4 May 2010. Web.

[12] K.S. Hayden, K. Park, J.S. Curtis, Effect of Particle Characteristics on Particle Pickup Velocity, Powder Technology 131 (2003) 7-14.

[13] Kalman, H., A. Satran, D. Meir, and E. Rabinovich. "Pickup (critical) Velocity of Particles." Powder Technology 160.2 (2005): 103-13. Print.

[14] Kim, Jae-Hyung, and Heuy-Dong Kim. "Effect of Diffuser Angle on the Discharge Coefficient of Miniature Critical Nozzles." Journal of Mechanical Science and Technology 24.9 (2010): 1793-798. Print.

[15] Li, Tingwen, and Chris Guenther. "A CFD Study of Gas-Solid Jet in a CFB Riser Flow." American Institute of Chemical Engineers (2012): 756-69. Print.

[16] Munson, Bruce Roy, Donald F. Young, and T. H. Okiishi. Fundamentals of Fluid Mechanics. Hoboken, NJ: J. Wiley & Sons, 2006. Print.

[17] Pattanapol, W., S. J. Wakes, and M. Hilton. "Using Computational Fluid Dynamics to Determine Suitable Foredune Morphologies in New Zealand." Journal of Coastal Research 64 (2011): 298-302.

[18] Phillips, Mike. "A Force Balance Model for Particle Entrainment into a Fluid Stream." Applied Physics 13 (1980): 221-33. Print.

[19] A. Ramadan, P. Skalle, S.T. Johansen, A Mechanistic Model to Determine the Critical Flow Velocity Required to Initiate the Movement of Spherical Bed Particles in Inclined Channels, Chemical Engineering Science 58 (2003) 2153-2163.

[20] Schlichting, Hermann. Boundary-layer Theory. New York: McGraw-Hill, 1979. Print.

[21] Zenz, F. A. "Conveyability of Materials of Mixed Particle Size." Industrial & Engineering Chemistry Fundamentals 3.1 (1964): 65-75. Print.

[22] Zhang, Leying. "3D Numerical Modeling of Hydrodynamic Flow, Sediment Deposition and Transport in Stormwater Ponds and Alluvial Channels." Diss. Old Dominion University, 2009. Web.

Appendix A.

Fluids Calculations Spreadsheet

The calculation of the flow parameters throughout the collector duct requires extensive amounts of iteration. As a result, an excel spreadsheet was compiled with all of the calculations that allows the values to be quickly iterated and confirm that all equations are satisfied. An overview of the excel spreadsheet is pictured in Figure A.1. In the upper left hand corner is the section containing all of the user inputs. This section allows the user to input the parameters of the rectangular duct sizing, the surface roughness, and the inlet pressure to the system. The two sections below the user inputs provide the outputs of the compressible and incompressible flow calculations. The user must run the built-in excel solver to iterate and find the Mach number at the inlet as explained in the "Directions" section. The next step is to iterate the temperature at point 4 and the pressure at point 3 utilizing the section labeled "Values to Iterate". The guess values, highlighted in gold, are changed manually by the user until they match the values that satisfy the equations, highlighted in green. The results are displayed on the diagram at key locations throughout the rectangular duct. The two sections below the diagram calculate the estimated flow time of the system and the desired pick up velocity. When the velocity calculated at the collection area, point 4, is greater than the minimum pick up velocity it is highlighted in green; if it is not greater than the minimum pick up velocity it is highlighted in red. The spreadsheet allowed the collection velocity to be quickly predicted dependent upon the collector dimensions and the inlet pressure.

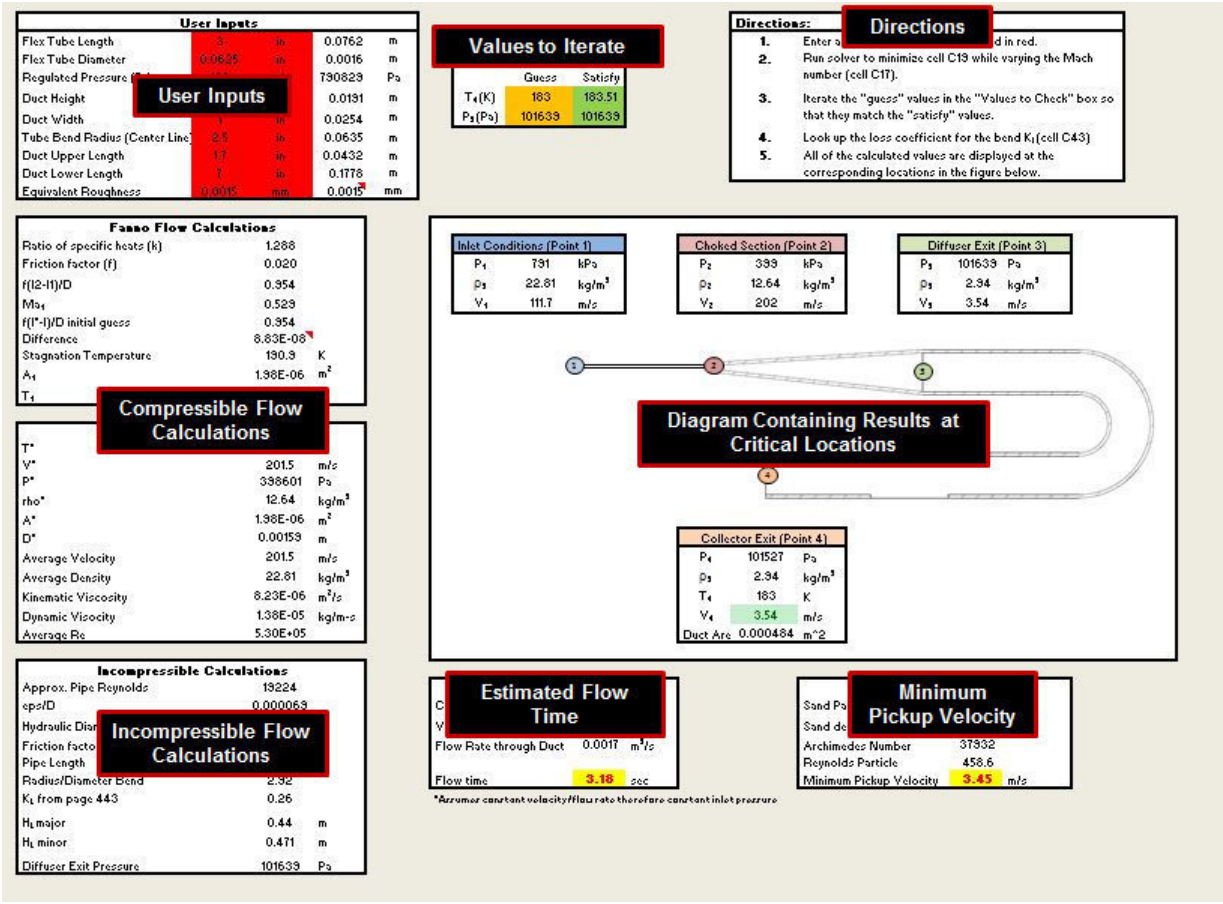

Figure A.1: User interface created in excel to iterate through fluids calculations.

Appendix B.

Collector Mesh Generation

The mesh is a critical part of the FLUENT simulations and is dependent on the geometry of the system. A Matlab script file was created to allow the user to input the following parameters: rectangular duct width and height, upper straight length, lower straight length, diffuser angle, and the bend radius. It also requires the user to input the boundary layer grid spacing dimension for the duct as well as the tubing prior to the inlet. The boundary layer dimensions are calculated based on a desired y^+ value as well as a reference length and Reynolds number. The standard wall-functions utilized within FLUENT require that the y^+ value be greater than 30 or else the functions will deteriorate affecting the overall solution. The local skin friction coefficient is,

$$C_f = \left[2 \cdot \log_{10}(Re) - 0.65\right]^{-2.3} \tag{B.1}$$

as approximated by Schlichting[20] for a turbulent boundary layer. The wall shear stress is then computed as,

$$\tau_w = C_f \cdot \frac{1}{2}\rho U_\infty^2 \tag{B.2}$$

where U_∞ is the free stream velocity. The wall grid spacing is then computed using Equation B.3.

$$\Delta s = \frac{y^+ \mu}{\rho \sqrt{\frac{\tau_w}{\rho}}} \tag{B.3}$$

The wall spacing is computed for the section of thin pipe illustrated as points 1 to 2 in Figure 4.6 as well as the rectangular duct depicted as points 3 to 4 in Figure 4.7. A file was created with all of the key points for the geometry to be input into ANSYS ICEM; an example of the points output is pictured in Figure B.1. It should be noted that the aspect ratio is not accurate in the plot shown in the figure. After importing the parts to ANSYS ICEM a script file was run to create all of the surfaces as well as to block the geometry for grid generation. This method kept all of the mesh's consistent as well as made the process more efficient for geometry changes. A completed mesh is pictured in Figure B.2.

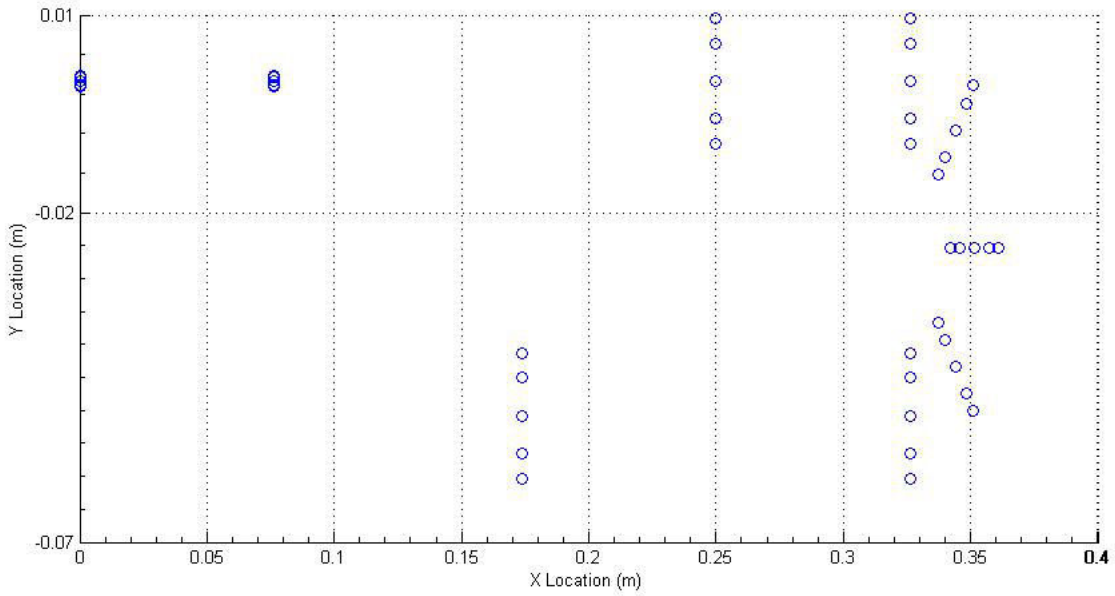

Figure B.1: Key points generated by Matlab script file for mesh generation.

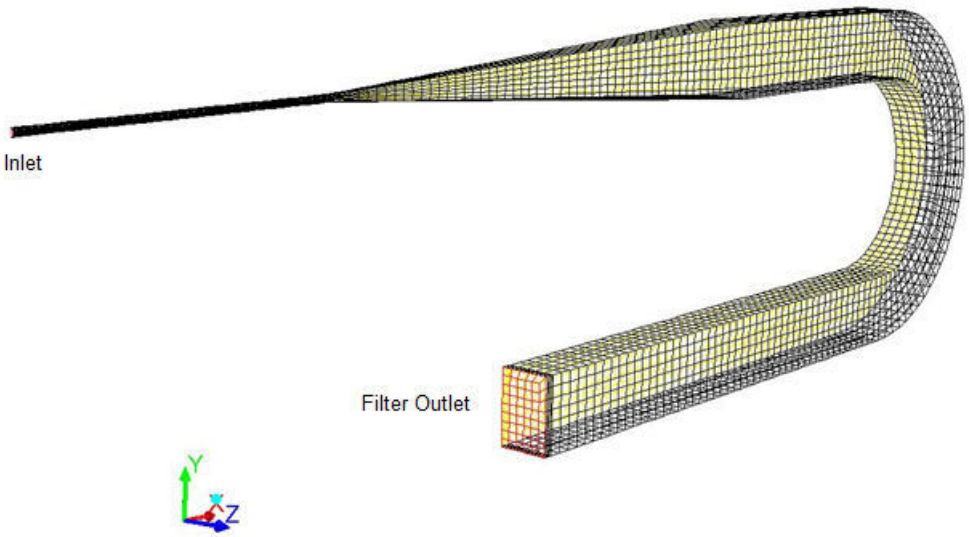

Figure B.2: Completed mesh for the CFD simulations utilizing automated generation process.

Appendix C.

Final Collector Design Drawing

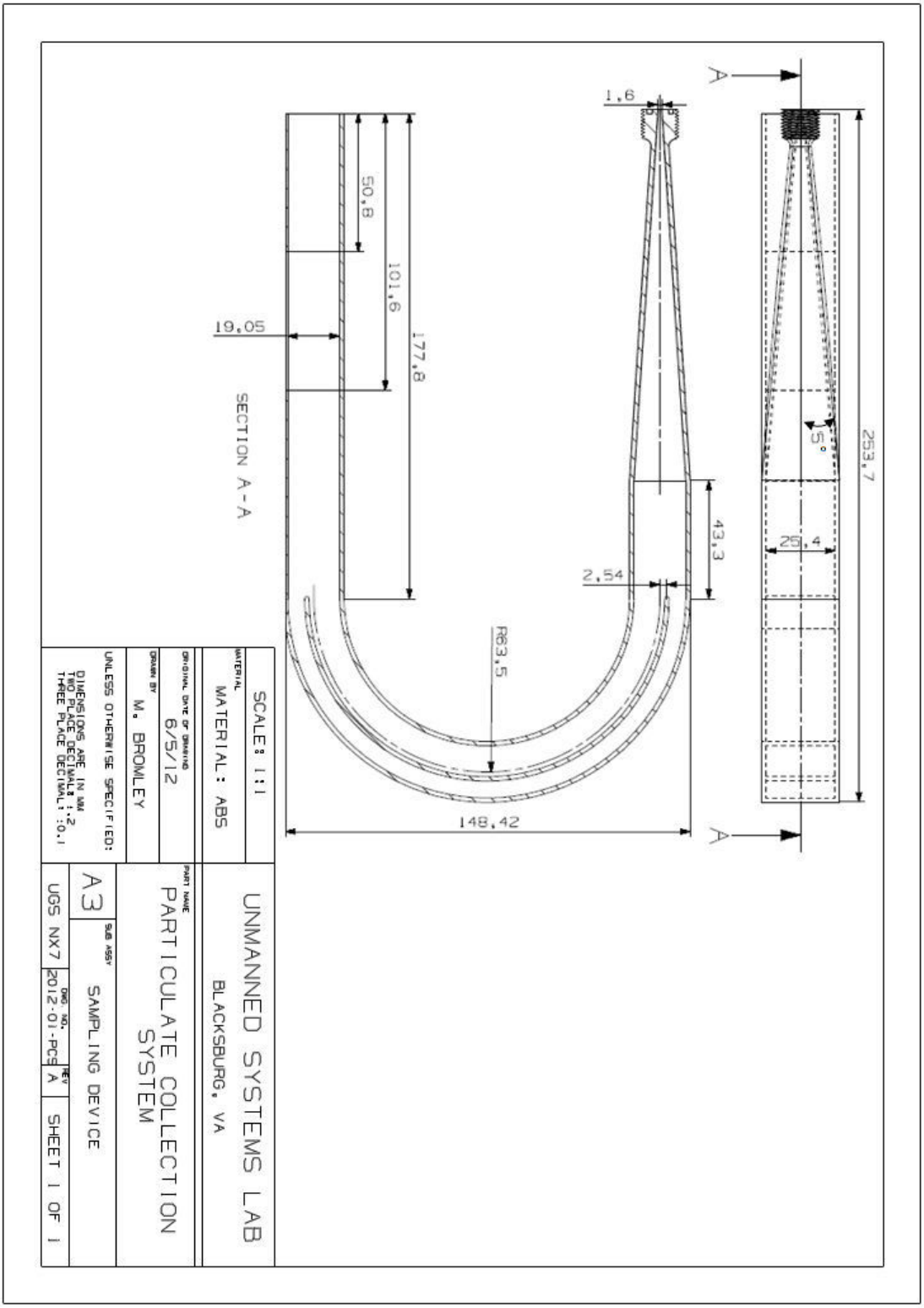

Figure C.1: Final collector design.

Appendix D.

FLUENT Model Parameters Summary

			1	2
			Original Case	**Original Case - Filter**
			2D_TestBench_Nozzle_Original	2DTestBench_Nozzle_Original_Filter Added
		DATE	9/6/2011	9/7/2011
General				
	Solver Type		Pressure-Based	Pressure-Based
	Velocity Formulation		Absolute	Absolute
	Time		Transient	Transient
	Gravity		Yes	Yes
	2D Space		Planar	Planar
Models				
	Multiphase		Yes	Yes
		Model	Eulerian	Eulerian
		Volume Fraction Scheme	Explicit	Explicit
		Courant Number	0.25	0.25
		Number of Phases	2	2
	Viscous			
		Model	k-epsilon (2 eqn)	k-epsilon (2 eqn)
		Reynolds-Stress Model	n/a	n/a
		k-epsilon Model	Standard	Standard
		Reynolds-Stress Optons	n/a	n/a
		RNG Options	none	none
		Near-Wall Treatment	Standard Wall Functions	Standard Wall Functions
		Turbulence Multiphase Model	Dispersed	Dispersed
Materials				
	Sand			
		Density (kg/m^3)	2000	2000
	Air			
		Density (kg/m^3)	1.225	1.225
		Viscosity (kg/m-s)	1.79E-05	1.79E-05
Phases				
	Primary Phase		Air	Air
	Secondary Phase			
		Phase Material	Sand	Sand
		Granular	Yes	Yes
		Packed Bed	No	No
		Granular Temperature Model	Phase Property	Phase Property
		Diameter (in)	0.015748	0.015748
		Granular Viscosity (kg/m-s)	gidaspow	gidaspow
		Granular Bulk Viscosity (kg/m-s)	lun-et-al	lun-et-al
		Frictional Viscosity (kg/m-s)	none	none
		Angle of Internal Friction (deg)	n/a	n/a
		Frictional Pressure (pascal)	n/a	n/a
		Frictional Modulus (pascal)	n/a	n/a
		Fricti ona Packing Limit	n/a	n/a
		Granular Tmperature (m2/s2)	algebraic	algebraic
		Solids Pressure (pascal)	lun-et-al	lun-et-al
		Radial Distribution	lun-et-al	lun-et-al
		Elasticity Modulus (pascal)	derived	derived
		Packing Limit	0.63	0.63
	Interaction			
		Drag Coefficient	gidaspow	gidaspow
		Lift	none	none
		Collisions	0.9	0.9
		Slip	n/a	n/a
		Heat	n/a	n/a
		Mass	n/a	n/a
		Reactions	n/a	n/a
		Surface Tension	none	none
Boundary Conditions				
	Inlet			
		Velocity Specification Method	Magnitude, Normal to Boundary	Magnitude, Normal to Boundary
		Reference Frame	Absolute	Absolute
		Velocity Magnitude (m/s)	345	345
		Turbulence Specification Method	Intensity and Hydraulic Diameter	K and Epsilon

			1	2
			Original Case	**Original Case - Filter**
		Turbulent Intensity (%)	20	n/a
		Turbulent Kinetic Energy	n/a	0
		Hydraulic Diameter (in)	0.035	n/a
		Turbulent Dissipation Rate	n/a	0
		Reynolds-Stress Specification Method	n/a	n/a
	Outlet			
		Type	Pressure Outlet	Pressure Outlet
		Gauge Pressure (pascal)	0	0
		Backflow Direction Specification Method	Normal to Boundary	Normal to Boundary
		Turbulence Specification Method	K and Epsilon	K and Epsilon
		Backflow Turbulent Kinetic Energy (m2/s2)	1	1
		Backflow Turbulent Dissipation Rate (m2/s3)	1	1
		Reynolds-Stress Specification Method	n/a	n/a
	Wall			
		Air	No Slip	No Slip
		Sand	No Slip	No Slip
Solution Methods				
	Pressure-Velocity Coupling Scheme		Phase Coupled SIMPLE	Phase Coupled SIMPLE
	Spatial Discretization			
		Gradient	Least Squares Cell Based	Least Squares Cell Based
		Momentum	First Order Upwind	First Order Upwind
		Volume Fraction	First Order Upwind	First Order Upwind
		Turbulent Kinetic Energy	First Order Upwind	First Order Upwind
		Turbulent Dissipation Rate	First Order Upwind	First Order Upwind
		Reynolds Stresses	n/a	n/a
	Transient Formulation		First Order Implicit	First Order Implicit
Solution Controls				
	Under-Relaxation Factors			
		Pressure	0.3	0.3
		Density	1	1
		Body Forces	1	1
		Momentum	0.7	0.7
		Granular Temperature	0.2	0.2
		Turbulent Kinetic Energy	0.8	0.8
		Turbulent Dissipation Rate	0.8	0.8
		Turbulent Viscosity	1	1
		Reynolds Stresses	n/a	n/a
Monitors				
	Residuals			
		Continuity	1.00E-05	1.00E-05
		U-air	0.001	0.001
		U-sand	0.001	0.001
		V-air	0.001	0.001
		V-sand	0.001	0.001
		W-air	0.001	0.001
		W-sand	0.001	0.001
		K-air	0.001	0.001
		K-sand	0.001	0.001
		Eps-air	0.001	0.001
		Eps-sand	0.001	0.001
		UU-air	n/a	n/a
		VV-air	n/a	n/a
		WW-air	n/a	n/a
		UV-air	n/a	n/a
		VW-air	n/a	n/a
		UW-air	n/a	n/a
		Convergence Criterion	Absolute	Absolute
Solution Initialization				
	Patch			
		Sand Volume Fraction	0.617	0.617
Run Calculation				
	Time Stepping Method		Fixed	Fixed
	Time Step Size (s)		1.00E-06	5.50E-06
	Max Iterations/Time Step		800	800

			3	4
			Original Case - Modified Mesh	**Frictional Viscosity - Modified Mesh**
			2D_ModifiedMesh_OriginalParameters	2D_ModifiedMesh_FrictionalViscosity
		DATE	9/14/2011	9/15/2011
General				
	Solver Type		Pressure-Based	Pressure-Based
	Velocity Formulation		Absolute	Absolute
	Time		Transient	Transient
	Gravity		Yes	Yes
	2D Space		Planar	Planar
Models				
	Multiphase		Yes	Yes
		Model	Eulerian	Eulerian
		Volume Fraction Scheme	Explicit	Explicit
		Courant Number	0.25	0.25
		Number of Phases	2	2
	Viscous			
		Model	k-epsilon (2 eqn)	k-epsilon (2 eqn)
		Reynolds-Stress Model	n/a	n/a
		k-epsilon Model	Standard	Standard
		Reynolds-Stress Optons	n/a	n/a
		RNG Options	none	none
		Near-Wall Treatment	Standard Wall Functions	Standard Wall Functions
		Turbulence Multiphase Model	Dispersed	Dispersed
Materials				
	Sand			
		Density (kg/m^3)	2000	2000
	Air			
		Density (kg/m^3)	1.225	1.225
		Viscosity (kg/m-s)	1.79E-05	1.79E-05
Phases				
	Primary Phase		Air	Air
	Secondary Phase			
		Phase Material	Sand	Sand
		Granular	Yes	Yes
		Packed Bed	No	No
		Granular Temperature Model	Phase Property	Phase Property
		Diameter (in)	0.015748	0.015748
		Granular Viscosity (kg/m-s)	gidaspow	gidaspow
		Granular Bulk Viscosity (kg/m-s)	lun-et-al	lun-et-al
		Frictional Viscosity (kg/m-s)	none	Schaeffer
		Angle of Internal Friction (deg)	n/a	30
		Frictional Pressure (pascal)	n/a	based-ktgf
		Frictional Modulus (pascal)	n/a	derived
		Frictiona Packing Limit	n/a	0.5
		Granular Tmperature (m2/s2)	algebraic	algebraic
		Solids Pressure (pascal)	lun-et-al	lun-et-al
		Radial Distribution	lun-et-al	lun-et-al
		Elasticity Modulus (pascal)	derived	derived
		Packing Limit	0.63	0.63
	Interaction			
		Drag Coefficient	gidaspow	gidaspow
		Lift	none	none
		Collisions	0.9	0.9
		Slip	n/a	n/a
		Heat	n/a	n/a
		Mass	n/a	n/a
		Reactions	n/a	n/a
		Surface Tension	none	none
Boundary Conditions				
	Inlet			
		Velocity Specification Method	Magnitude, Normal to Boundary	Magnitude, Normal to Boundary
		Reference Frame	Absolute	Absolute
		Velocity Magnitude (m/s)	345	345
		Turbulence Specification Method	Intensity and Hydraulic Diameter	Intensity and Hydraulic Diameter

			3	4
			Original Case - Modified Mesh	**Frictional Viscosity - Modified Mesh**
		Turbulent Intensity (%)	20	20
		Turbulent Kinetic Energy	n/a	n/a
		Hydraulic Diameter (in)	0.035	0.035
		Turbulent Dissipation Rate	n/a	n/a
		Reynolds-Stress Specification Method	n/a	n/a
	Outlet			
		Type	Pressure Outlet	Pressure Outlet
		Gauge Pressure (pascal)	0	0
		Backflow Direction Specification Method	Normal to Boundary	Normal to Boundary
		Turbulence Specification Method	K and Epsilon	K and Epsilon
		Backflow Turbulent Kinetic Energy (m2/s2)	1	1
		Backflow Turbulent Dissipation Rate (m2/s3)	1	1
		Reynolds-Stress Specification Method	n/a	n/a
	Wall			
		Air	No Slip	No Slip
		Sand	No Slip	No Slip
Solution Methods				
	Pressure-Velocity Coupling Scheme		Phase Coupled SIMPLE	Phase Coupled SIMPLE
	Spatial Discretization			
		Gradient	Least Squares Cell Based	Least Squares Cell Based
		Momentum	First Order Upwind	First Order Upwind
		Volume Fraction	First Order Upwind	First Order Upwind
		Turbulent Kinetic Energy	First Order Upwind	First Order Upwind
		Turbulent Dissipation Rate	First Order Upwind	First Order Upwind
		Reynolds Stresses	n/a	n/a
	Transient Formulation		First Order Implicit	First Order Implicit
Solution Controls				
	Under-Relaxation Factors			
		Pressure	0.3	0.3
		Density	1	1
		Body Forces	1	1
		Momentum	0.7	0.7
		Granular Temperature	0.2	0.2
		Turbulent Kinetic Energy	0.8	0.8
		Turbulent Dissipation Rate	0.8	0.8
		Turbulent Viscosity	1	1
		Reynolds Stresses	n/a	n/a
Monitors				
	Residuals			
		Continuity	1.00E-05	1.00E-05
		U-air	0.001	0.001
		U-sand	0.001	0.001
		V-air	0.001	0.001
		V-sand	0.001	0.001
		W-air	0.001	0.001
		W-sand	0.001	0.001
		K-air	0.001	0.001
		K-sand	0.001	0.001
		Eps-air	0.001	0.001
		Eps-sand	0.001	0.001
		UU-air	n/a	n/a
		VV-air	n/a	n/a
		WW-air	n/a	n/a
		UV-air	n/a	n/a
		VW-air	n/a	n/a
		UW-air	n/a	n/a
		Convergence Criterion	Absolute	Absolute
Solution Initialization				
	Patch			
		Sand Volume Fraction	0.617	0.617
Run Calculation				
	Time Stepping Method		Fixed	Fixed
	Time Step Size (s)		5.50E-06	5.50E-06
	Max Iterations/Time Step		800	800

			5	6
			Second Order - Modified Mesh	**Zero Wall Shear - Modified Mesh**
			2D_ModifiedMesh_SecondOrder	2D_ModifiedMesh_SecondOrder_ZeroShearWalls
		DATE	9/20/2011	9/20/2011
General				
	Solver Type		Pressure-Based	Pressure-Based
	Velocity Formulation		Absolute	Absolute
	Time		Transient	Transient
	Gravity		Yes	Yes
	2D Space		Planar	Planar
Models				
	Multiphase		Yes	Yes
		Model	Eulerian	Eulerian
		Volume Fraction Scheme	Explicit	Explicit
		Courant Number	0.25	0.25
		Number of Phases	2	2
	Viscous			
		Model	k-epsilon (2 eqn)	k-epsilon (2 eqn)
		Reynolds-Stress Model	n/a	n/a
		k-epsilon Model	Standard	Standard
		Reynolds-Stress Optons	n/a	n/a
		RNG Options	none	none
		Near-Wall Treatment	Standard Wall Functions	Standard Wall Functions
		Turbulence Multiphase Model	Dispersed	Dispersed
Materials				
	Sand			
		Density (kg/m^3)	2000	2000
	Air			
		Density (kg/m^3)	1.225	1.225
		Viscosity (kg/m-s)	1.79E-05	1.79E-05
Phases				
	Primary Phase		Air	Air
	Secondary Phase			
		Phase Material	Sand	Sand
		Granular	Yes	Yes
		Packed Bed	No	No
		Granular Temperature Model	Phase Property	Phase Property
		Diameter (in)	0.015748	0.015748
		Granular Viscosity (kg/m-s)	gidaspow	gidaspow
		Granular Bulk Viscosity (kg/m-s)	lun-et-al	lun-et-al
		Frictional Viscosity (kg/m-s)	Schaeffer	Schaeffer
		Angle of Internal Friction (deg)	30	30
		Frictional Pressure (pascal)	based-ktgf	based-ktgf
		Frictional Modulus (pascal)	derived	derived
		Fricitona Packing Limit	0.5	0.5
		Granular Tmperature (m2/s2)	algebraic	algebraic
		Solids Pressure (pascal)	lun-et-al	lun-et-al
		Radial Distribution	lun-et-al	lun-et-al
		Elasticity Modulus (pascal)	derived	derived
		Packing Limit	0.63	0.63
	Interaction			
		Drag Coefficient	gidaspow	gidaspow
		Lift	none	none
		Collisions	0.9	0.9
		Slip	n/a	n/a
		Heat	n/a	n/a
		Mass	n/a	n/a
		Reactions	n/a	n/a
		Surface Tension	none	none
Boundary Conditions				
	Inlet			
		Velocity Specification Method	Magnitude, Normal to Boundary	Magnitude, Normal to Boundary
		Reference Frame	Absolute	Absolute
		Velocity Magnitude (m/s)	345	345
		Turbulence Specification Method	Intensity and Hydraulic Diameter	Intensity and Hydraulic Diameter

			5	6
			Second Order - Modified Mesh	**Zero Wall Shear - Modified Mesh**
		Turbulent Intensity (%)	20	20
		Turbulent Kinetic Energy	n/a	n/a
		Hydraulic Diameter (in)	0.035	0.035
		Turbulent Dissipation Rate	n/a	n/a
		Reynolds-Stress Specification Method	n/a	n/a
	Outlet			
		Type	Pressure Outlet	Pressure Outlet
		Gauge Pressure (pascal)	0	0
		Backflow Direction Specification Method	Normal to Boundary	Normal to Boundary
		Turbulence Specification Method	K and Epsilon	K and Epsilon
		Backflow Turbulent Kinetic Energy (m2/s2)	1	1
		Backflow Turbulent Dissipation Rate (m2/s3)	1	1
		Reynolds-Stress Specification Method	n/a	n/a
	Wall			
		Air	No Slip	No Slip
		Sand	No Slip	0 Shear x and y components
Solution Methods				
	Pressure-Velocity Coupling Scheme		Phase Coupled SIMPLE	Phase Coupled SIMPLE
	Spatial Discretization			
		Gradient	Least Squares Cell Based	Least Squares Cell Based
		Momentum	Second Order Upwind	Second Order Upwind
		Volume Fraction	QUICK	QUICK
		Turbulent Kinetic Energy	First Order Upwind	First Order Upwind
		Turbulent Dissipation Rate	First Order Upwind	First Order Upwind
		Reynolds Stresses	n/a	n/a
	Transient Formulation		First Order Implicit	First Order Implicit
Solution Controls				
	Under-Relaxation Factors			
		Pressure	0.3	0.3
		Density	1	1
		Body Forces	1	1
		Momentum	0.7	0.7
		Granular Temperature	0.2	0.2
		Turbulent Kinetic Energy	0.8	0.8
		Turbulent Dissipation Rate	0.8	0.8
		Turbulent Viscosity	1	1
		Reynolds Stresses	n/a	n/a
Monitors				
	Residuals			
		Continuity	1.00E-05	1.00E-05
		U-air	0.001	0.001
		U-sand	0.001	0.001
		V-air	0.001	0.001
		V-sand	0.001	0.001
		W-air	0.001	0.001
		W-sand	0.001	0.001
		K-air	0.001	0.001
		K-sand	0.001	0.001
		Eps-air	0.001	0.001
		Eps-sand	0.001	0.001
		UU-air	n/a	n/a
		VV-air	n/a	n/a
		WW-air	n/a	n/a
		UV-air	n/a	n/a
		VW-air	n/a	n/a
		UW-air	n/a	n/a
		Convergence Criterion	Absolute	Absolute
Solution Initialization				
	Patch			
		Sand Volume Fraction	0.617	0.617
Run Calculation				
	Time Stepping Method		Fixed	Fixed
	Time Step Size (s)		1.00E-06	1.00E-06
	Max Iterations/Time Step		800	800

	7	8
	Symmetric Mesh - Final 2D Parameters	**Leakage Inlet**
	3DCase_2DFinalParameters_ModMesh_SandVol	3DCase_2DFinalParameters_ModMesh_LeakInlet
DATE	10/8/2011	11/9/2011
General		
Solver Type	Pressure-Based	Pressure-Based
Velocity Formulation	Absolute	Absolute
Time	Transient	Transient
Gravity	Yes	Yes
Models		
Multiphase	Yes	Yes
Model	Eulerian	Eulerian
Volume Fraction Scheme	Implicit	Implicit
Courant Number	0.1	n/a
Number of Phases	2	2
Viscous		
Model	k-epsilon (2 eqn)	k-epsilon (2 eqn)
Reynolds-Stress Model	n/a	n/a
k-epsilon Model	Standard	Standard
Reynolds-Stress Optons	n/a	n/a
RNG Options	none	none
Near-Wall Treatment	Standard Wall Functions	Standard Wall Functions
Turbulence Multiphase Model	Dispersed	Dispersed
Materials		
Sand		
Density (kg/m^3)	2000	2000
Air		
Density (kg/m^3)	1.225	1.225
Viscosity (kg/m-s)	1.79E-05	1.79E-05
Phases		
Primary Phase	Air	Air
Secondary Phase		
Phase Material	Sand	Sand
Granular	Yes	Yes
Packed Bed	No	No
Granular Temperature Model	Phase Property	Phase Property
Diameter (in)	0.015748	0.015748
Granular Viscosity (kg/m-s)	gidaspow	gidaspow
Granular Bulk Viscosity (kg/m-s)	lun-et-al	lun-et-al
Frictional Viscosity (kg/m-s)	Schaeffer	Schaeffer
Angle of Internal Friction (deg)	30	30
Frictional Pressure (pascal)	based-ktgf	based-ktgf
Frictional Modulus (pascal)	derived	derived
Frictiona Packing Limit	0.5	0.5
Granular Tmperature (m2/s2)	Algebraic	Algebraic
Solids Pressure (pascal)	lun-et-al	lun-et-al
Radial Distribution	lun-et-al	lun-et-al
Elasticity Modulus (pascal)	derived	derived
Packing Limit	0.6	0.6
Interaction		
Drag Coefficient	gidaspow	gidaspow
Lift	none	none
Collisions	0.9	0.9
Slip	n/a	n/a
Heat	n/a	n/a
Mass	n/a	n/a
Reactions	n/a	n/a
Surface Tension	none	none
Boundary Conditions		
Inlet		
Velocity Specification Method	Magnitude, Normal to Boundary	Magnitude, Normal to Boundary
Reference Frame	Absolute	Absolute
Velocity Magnitude (m/s)	600	600
Turbulence Specification Method	Intensity and Hydraulic Diameter	Intensity and Hydraulic Diameter
Turbulent Intensity (%)	50	20
Hydraulic Diameter (in)	0.035	0.035
Reynolds-Stress Specification Method	n/a	n/a
Leak Inlet		
Type		Velocity Magnitude, Normal to Boundary

	7	8
	Symmetric Mesh - Final 2D Parameters	**Leakage Inlet**
Reference Frame		Absolute
Velocity Magnitude (m/s)		6
Turbulence Specification Method		K and Epsilon
Turbulent Intensity (%)		1
Hydraulic Diameter (in)		1
Reynolds-Stress Specification Method		n/a
Outlet		
Type	Pressure Outlet	Pressure Outlet
Gauge Pressure (pascal)	0	0
Backflow Direction Specification Method	Normal to Boundary	Normal to Boundary
Turbulence Specification Method	K and Epsilon	K and Epsilon
Backflow Turbulent Kinetic Energy (m2/s2)	1	1
Backflow Turbulent Dissipation Rate (m2/s3)	1	1
Reynolds-Stress Specification Method	n/a	n/a
Wall		
Air	No Slip	No Slip
Sand	0 Shear x and y components	0 Shear x and y components
Solution Methods		
Pressure-Velocity Coupling Scheme	Phase Coupled SIMPLE	Phase Coupled SIMPLE
Spatial Discretization		
Gradient	Least Squares Cell Based	Least Squares Cell Based
Momentum	Second Order Upwind	Second Order Upwind
Volume Fraction	QUICK	QUICK
Turbulent Kinetic Energy	First Order Upwind	First Order Upwind
Turbulent Dissipation Rate	First Order Upwind	First Order Upwind
Reynolds Stresses	n/a	n/a
Transient Formulation	First Order Implicit	First Order Implicit
Solution Controls		
Under-Relaxation Factors		
Pressure	0.3	0.3
Density	1	1
Body Forces	1	1
Momentum	0.7	0.7
Granular Temperature	0.2	0.2
Turbulent Kinetic Energy	0.8	0.8
Turbulent Dissipation Rate	0.8	0.8
Turbulent Viscosity	1	1
Reynolds Stresses	n/a	n/a
Monitors		
Residuals		
Continuity	1.00E-05	1.00E-05
U-air	0.001	0.001
U-sand	0.001	0.001
V-air	0.001	0.001
V-sand	0.001	0.001
W-air	0.001	0.001
W-sand	0.001	0.001
K-air	0.001	0.001
K-sand	0.001	0.001
Eps-air	0.001	0.001
Eps-sand	0.001	0.001
UU-air	n/a	n/a
VV-air	n/a	n/a
WW-air	n/a	n/a
UV-air	n/a	n/a
VW-air	n/a	n/a
UW-air	n/a	n/a
Convergence Criterion	Absolute	Absolute
Solution Initialization		
Patch		
Sand Volume Fraction	0.6	0.6
Run Calculation		
Time Stepping Method	Fixed	Fixed
Time Step Size (s)	1.00E-08	1.00E-06
Max Iterations/Time Step	300	400

			9	10
			Leakage Inlet	**Leakage Inlet**
			3DCase_2DFinalParameters_ModMesh_PressureLeakInlet	3DCase_2DFinalParameters_PressureLeakInlet_ReducedVelocity
		DATE	11/15/2011	12/2/2011
General				
	Solver Type		Pressure-Based	Pressure-Based
	Velocity Formulation		Absolute	Absolute
	Time		Transient	Transient
	Gravity		Yes	Yes
Models				
	Multiphase		Yes	Yes
		Model	Eulerian	Eulerian
		Volume Fraction Scheme	Explicit	Explicit
		Courant Number	0.1	0.1
		Number of Phases	2	2
	Viscous			
		Model	k-epsilon (2 eqn)	k-epsilon (2 eqn)
		Reynolds-Stress Model	n/a	n/a
		k-epsilon Model	Standard	Standard
		Reynolds-Stress Optons	n/a	n/a
		RNG Options	none	none
		Near-Wall Treatment	Standard Wall Functions	Standard Wall Functions
		Turbulence Multiphase Model	Dispersed	Dispersed
Materials				
	Sand			
		Density (kg/m^3)	2000	2000
	Air			
		Density (kg/m^3)	1.225	1.225
		Viscosity (kg/m-s)	1.79E-05	1.79E-05
Phases				
	Primary Phase		Air	Air
	Secondary Phase			
		Phase Material	Sand	Sand
		Granular	Yes	Yes
		Packed Bed	No	No
		Granular Temperature Model	Phase Property	Phase Property
		Diameter (in)	0.015748	0.015748
		Granular Viscosity (kg/m-s)	gidaspow	gidaspow
		Granular Bulk Viscosity (kg/m-s)	lun-et-al	lun-et-al
		Frictional Viscosity (kg/m-s)	Schaeffer	Schaeffer
		Angle of Internal Friction (deg)	30	30
		Frictional Pressure (pascal)	based-ktgf	based-ktgf
		Frictional Modulus (pascal)	derived	derived
		Frictiona Packing Limit	0.5	0.5
		Granular Tmperature (m2/s2)	Algebraic	Algebraic
		Solids Pressure (pascal)	lun-et-al	lun-et-al
		Radial Distribution	lun-et-al	lun-et-al
		Elasticity Modulus (pascal)	derived	derived
		Packing Limit	0.6	0.6
	Interaction			
		Drag Coefficient	gidaspow	gidaspow
		Lift	none	none
		Collisions	0.9	0.9
		Slip	n/a	n/a
		Heat	n/a	n/a
		Mass	n/a	n/a
		Reactions	n/a	n/a
		Surface Tension	none	none
Boundary Conditions				
	Inlet			
		Velocity Specification Method	Magnitude, Normal to Boundary	Magnitude, Normal to Boundary
		Reference Frame	Absolute	Absolute
		Velocity Magnitude (m/s)	600	600
		Turbulence Specification Method	Intensity and Hydraulic Diameter	Intensity and Hydraulic Diameter
		Turbulent Intensity (%)	20	20
		Hydraulic Diameter (in)	0.035	0.035
		Reynolds-Stress Specification Method	n/a	n/a
	Leak Inlet			
		Type	Vent Inlet, normal to boundary	Vent Inlet, normal to boundary

			9	10
			Leakage Inlet	**Leakage Inlet**
		Reference Frame	n/a	n/a
		Velocity Magnitude (m/s)	n/a	n/a
		Turbulence Specification Method	K and Epsilon	K and Epsilon
		Turbulent Intensity (%)	1	1
		Hydraulic Diameter (in)	1	1
		Reynolds-Stress Specification Method	n/a	n/a
	Outlet			
		Type	Pressure Outlet	Pressure Outlet
		Gauge Pressure (pascal)	0	0
		Backflow Direction Specification Method	Normal to Boundary	Normal to Boundary
		Turbulence Specification Method	K and Epsilon	K and Epsilon
		Backflow Turbulent Kinetic Energy (m2/s2)	1	1
		Backflow Turbulent Dissipation Rate (m2/s3)	1	1
		Reynolds-Stress Specification Method	n/a	n/a
	Wall			
		Air	No Slip	No Slip
		Sand	0 Shear x and y components	0 Shear x and y components
Solution Methods				
	Pressure-Velocity Coupling Scheme		Phase Coupled SIMPLE	Phase Coupled SIMPLE
	Spatial Discretization			
		Gradient	Least Squares Cell Based	Least Squares Cell Based
		Momentum	Second Order Upwind	Second Order Upwind
		Volume Fraction	QUICK	QUICK
		Turbulent Kinetic Energy	First Order Upwind	First Order Upwind
		Turbulent Dissipation Rate	First Order Upwind	First Order Upwind
		Reynolds Stresses	n/a	n/a
	Transient Formulation		First Order Implicit	First Order Implicit
Solution Controls				
	Under-Relaxation Factors			
		Pressure	0.3	0.3
		Density	1	1
		Body Forces	1	1
		Momentum	0.7	0.7
		Granular Temperature	0.2	0.2
		Turbulent Kinetic Energy	0.8	0.8
		Turbulent Dissipation Rate	0.8	0.8
		Turbulent Viscosity	1	1
		Reynolds Stresses	n/a	n/a
Monitors				
	Residuals			
		Continuity	1.00E-04	1.00E-04
		U-air	0.001	0.001
		U-sand	0.001	0.001
		V-air	0.001	0.001
		V-sand	0.001	0.001
		W-air	0.001	0.001
		W-sand	0.001	0.001
		K-air	0.001	0.001
		K-sand	0.001	0.001
		Eps-air	0.001	0.001
		Eps-sand	0.001	0.001
		UU-air	n/a	n/a
		VV-air	n/a	n/a
		WW-air	n/a	n/a
		UV-air	n/a	n/a
		VW-air	n/a	n/a
		UW-air	n/a	n/a
		Convergence Criterion	Absolute	Absolute
Solution Initialization				
	Patch			
		Sand Volume Fraction	0.6	0.6
Run Calculation				
	Time Stepping Method		Fixed	Fixed
	Time Step Size (s)		1.00E-06	1.00E-08
	Max Iterations/Time Step		200	200